https://lib.uliege.be https://matheo.uliege.be

Master thesis and internship[BR]- Master's Thesis : Aeroelastic modelling of the Sonaca 200[BR]- Internship (linked to master's thesis)

Auteur : Rulliere, Hadrien
Promoteur(s) : Dimitriadis, Grigorios
Faculté : Faculté des Sciences appliquées
Diplôme : Master en ingénieur civil en aérospatiale, à finalité spécialisée en "aerospace engineering"
Année académique : 2019-2020
URI/URL : http://hdl.handle.net/2268.2/10272

Avertissement à l'attention des usagers :

Tous les documents placés en accès ouvert sur le site le site MatheO sont protégés par le droit d'auteur. Conformément aux principes énoncés par la "Budapest Open Access Initiative"(BOAI, 2002), l'utilisateur du site peut lire, télécharger, copier, transmettre, imprimer, chercher ou faire un lien vers le texte intégral de ces documents, les disséquer pour les indexer, s'en servir de données pour un logiciel, ou s'en servir à toute autre fin légale (ou prévue par la réglementation relative au droit d'auteur). Toute utilisation du document à des fins commerciales est strictement interdite.

Par ailleurs, l'utilisateur s'engage à respecter les droits moraux de l'auteur, principalement le droit à l'intégrité de l'oeuvre et le droit de paternité et ce dans toute utilisation que l'utilisateur entreprend. Ainsi, à titre d'exemple, lorsqu'il reproduira un document par extrait ou dans son intégralité, l'utilisateur citera de manière complète les sources telles que mentionnées ci-dessus. Toute utilisation non explicitement autorisée ci-avant (telle que par exemple, la modification du document ou son résumé) nécessite l'autorisation préalable et expresse des auteurs ou de leurs ayants droit.

UNIVERSITY OF LIEGE
FACULTY OF APPLIED SCIENCES

Aeroelastic modelling of the Sonaca 200

Graduation Studies conducted for obtaining the Master's degree in Aerospace Engineering by Hadrien Rulliere

Realized in collaboration of Sonaca Aircraft

Academic supervisor

DIMITRIADIS Grigorios

Industrial supervisor

MENGDHEL Carl

Academic year 2019-2020

Acknowledgements

I would first thank my academic supervisor Pr. Grigorios Dimitriadis who allowed me to take part to this project in collaboration of *Sonaca Aircraft*. His advice and constructive critique were of great help during this work. I would also express my gratitude to Pr. Ludovic Noels for his helpful answers and suggestions at several points of the project and who accepted to be part of my jury.

Thanks a lot to my industrial supervisors Carl Mengdhel and Carl Dewandhel from *Sonaca Aircraft* for their daily support during the first weeks and their availability in spite of the lockdown situation that we endured in 2020. The interest they put in following my progress and answering my questions was very beneficial and encouraging, especially in the hard times of the pandemic. I am also grateful to every person at *Sonaca Aircraft* and members of the design department for their friendly welcome during my short but pleasant period in the facility. Special thanks to Pauline Fraiche who accepted to adapt her work schedule in order to facilitate to me remote access to certain resources of the company.

Many thanks to people from the *Leichtwerk AG* company who provided very useful numerical data on my request.

Last but not least, I would like to express my sincere gratitude to my family and friends who supported me all along my studies and these last months.

Abstract

The present work concerns flutter analysis of the Sonaca 200, more precisely extension of the aeroelastic model to the full airplane. It fits in the continuation of two master theses that studied aeroelastic behavior of the main wing. The studied configuration corresponds to the prototype state of the airplane in 2018, without fuel nor luggage and with fixed control surfaces. An analytical approach relying on Megson aircraft structures theory [1] is here implemented to provide structural models for the rear fuselage and the empennage that are suited for flutter analysis. The different components are then assembled using elastic connections to create a full finite element model of the aircraft. Numerical modal analysis is performed on this latter and the resulting eigenmodes are compared with experimental data from ground vibration testing for validation. In parallel, an aeroelastic model of the Sonaca 200 utilizing the vortex lattice theory [2][3] is developed in *Matlab* based on the work of Dimitriadis. It manages aerodynamic efforts on the structure with use of vortex ring elements and relies on modal analysis data to solve the aeroelastic equation of motion. The algorithm is first tested with experimental modes and provides a satifactory degree of comparison with reference aeroelastic solutions computed by the *Leichtwerk* company. Outputs of the finite element model are subsequently injected in the program to observe the differences in terms of aeroelastic solutions. The results seem encouraging but highlight sensitivity of the Vortex Lattice Method to modal parameters of the system. It would thus be beneficial to investigate ways of improving accuracy of the finite element model for it to be appropriate in practice. Part of this improvement may come from determination of the real boundary conditions with the ground. Besides, implementing movable control surface in the finite element model would allow to test critical configurations of the airplane where actual flutter might appear.

Contents

List of Figures

List of Tables

1 Introduction

Figure 1.1: Illustration picture of the Sonaca 200 in flight.

The Sonaca 200 is a recent two-seater light airplane produced by the *Sonaca Aircraft* company in Namur. Built in a full aluminium frame and powered with a single Rotax 914F four-stroke piston engine, it is mainly intended for the market of flight schools as its performances allow for an easy maneuverability at low speeds [4]. It abides to the Certification Specifications for Very Light Aeroplanes (CS-VLA) enacted by the European Union Aviation Safety Agency (EASA). In particular, the CS-VLA 629 specifies certain requirements in terms of aeroelastic behavior: "It must be shown [...] that the aeroplane is free from flutter, control reversal, and divergence for any condition of operation within the limit V-n envelope, and at all speeds [...]" [5]. All three phenomenon listed here above are caused by energy exchanges between the flexible aircraft structure and the air stream around it. They all present a tremendous risk for flight safety:

- control reversal is the loss of maneuverability due to flexibility of the main aerostructures [6], and was one of the possible explainations for the crash of the USAir Flight 427 in 1991 [7] ;
- divergence, which always occurs past a certain airspeed, describes a static deflection of the lifting surfaces that can lead to tearing as it was demonstrated in experimental conditions;
- flutter is related to modification of the apparent damping of the structure in flight conditions. Above a critical speed, certain modal damping terms of the system can become negative, so that any exterior excitation can trigger a possibly destructive neutrally stable or unstable oscillation regime.

The present work is focused on theoretical flutter analysis of the Sonaca 200. This phenomenon was well experienced on airplanes of World War I and remains critical nowadays as it caused the crash of a F117 bomber during an airshow in 1997. This being known to manufacturers, the first flutter testing campaigns were initiated in 1935 on German aircrafts [8] by measuring the maximum response amplitude as a function of airspeed. As the risks involved were too important for both the machines and the pilots, the testing techniques evolved to become safer and safer throughout the twentieth century. Flight flutter testing remains a recommended method by flight authorities to prove airworthiness of a prototype under development. Nonetheless, reliable analytical approaches were demonstrated in the past decades in order to offer good forecasting without the cost and logistics of experimental setups. Rationale analysis is indeed one of the three possible methods requested by the EASA to justify absence of flutter in the flight envelope [5]. Theodorsen's aerodynamics played a big role in the progress of the different techniques, like the British Flutter Method [9] established in 1982, and grounds the theoretical framework of the aeroelastic solutions presented in this report.

Certification of the Sonaca 200 was supported by a flutter analysis conducted by the *Leichtwerk AG* company. Vibrational behavior of the structure was obtained with ground vibration testings and aerodynamic effects were tackled using a 2D strip theory approach on a finite number of sections of the lifting surfaces: 66 in total. Twenty different configurations of the airplane were considered, including presence or not of fuel and luggage, locking or not of the control surface angles, and different altitudes. Conclusions of the study highlighted two possible cases for flutter to occur with speeds up to $1.2V_{\mathrm{D}}$, where V_{D} is the airplane dive speed. The first one is related to an eventual disconnection of the trim tab that generates strong instabilities in antisymmetric modes. Failure of the trim system is although rather unlikely and its airworthiness can easily be checked before flight. The second flutter occurrence appears at high altitude in control free conditions, without payload nor fuel, for the vibration mode corresponding to fuselage torsion. However this was not confirmed by flight flutter tests. Still, in order to ensure that this mode of flutter does not arise during flight, a boundary in terms of altitude and equivalent airspeed conditions was suggested in conclusion of the report. It corresponds in fact to a more convenient way to limit the true airspeed for the pilot, since this value is not displayed inside the aircraft cockpit. This given, the middle-term objective for the company is now to dispose of a reliable tool allowing for flutter analysis without requiring intervention of a third-party firm. It would benefits further developments of the aircraft in cases where assessment of compliance to the regulation is needed. It might be especially relevant in the possible prospect of an aerobatic version of the Sonaca 200 to be released. As an outcome, a second study was carried out in the framework of a master thesis to propose a solution using a finite element model of the wing and an approach to the aeorelastic problem relying on the three-dimensional Vortex Lattice Method (VLM) developed by Dimitriadis [3]. The Sonaca 200 was then limited to its main wing and it came out that the obtained results were comparable *Leichtwerk* findings. The present work fits in the continuation of this endeavour since the goal is to obtain an aeroelastic model for the full aircraft. Therefore, creation of a complete finite element model that is suitable for aeroelastic analysis is investigated and the VLM code is extensively modified to be able to process multiple lifting surfaces in interaction. The structural part of this project is treated by exploiting the Computer Aided Design (CAD) resources of *Sonaca Aircraft* for geometrical data gathering and finite element models are created with *Samcef* using the *NX 12* user interface. According to the company's engineers, use of the industrial finite element environment is avoided in order to save a consequent amount of training time. As to the aeroelastic part of the project, it relies on *Matlab* scripts and the *Matlab* API to execute certain *C++* functions.

After detailing the hypotheses and methodology for the structural description of the Sonaca 200, this report focuses on the practical creation of the finite element model and results of the numerical modal analysis. The last section is dedicated to definition of the actual aeroelastic model in the context of the Vortex Lattice Method and how the computed solutions compare with the reference material provided by *Leichtwerk*.

2 Structural approximation

2.1 Preliminary considerations

2.1.1 Definition of the problem

The Sonaca 200 exhibits a conventional architecture with a bottom main wing in the front and a classical empennage at the rear. Most of its structural components are made out of aluminium Al-6061-T6 which possesses the following mechanical properties:

- Young modulus: $E = 68.69$ GPa;
- Density: $\rho = 2700$ kg/m^3;
- Poisson's ratio: $\nu = 0.33$.

Layout of the structure is illustrated in Figure 2.1, in combination with the system of axes used in all the following discussions. The global basis is noted $(\mathbf{e}_X, \mathbf{e}_Y, \mathbf{e}_Z)$ and the body-attached bases defined at the different steps of the structural analysis use the lower case notation $(\mathbf{e}_x, \mathbf{e}_y, \mathbf{e}_z)$. In this regard, it is decided that $\mathbf{e}_x$ is always the out-of-plane vector when cross-sections are considered. The aircraft is studied in the empty configuration of the FTA2 version (March 2018), as used for the ground vibration testing campaign. Its total empty weight amounts to 473.50 kg and a ballast of 75 kg at the left seat is also taken into account to simulate the crew's mass. Other geometrical parameters of interest for the present study are listed in Table 1. From this point, acronyms are introduced to refer more easily the different aircraft members: WNG for the wing, HTP for the Horizontal Tail Plane and VTP for the Vertical Tail Plane. When necessary,

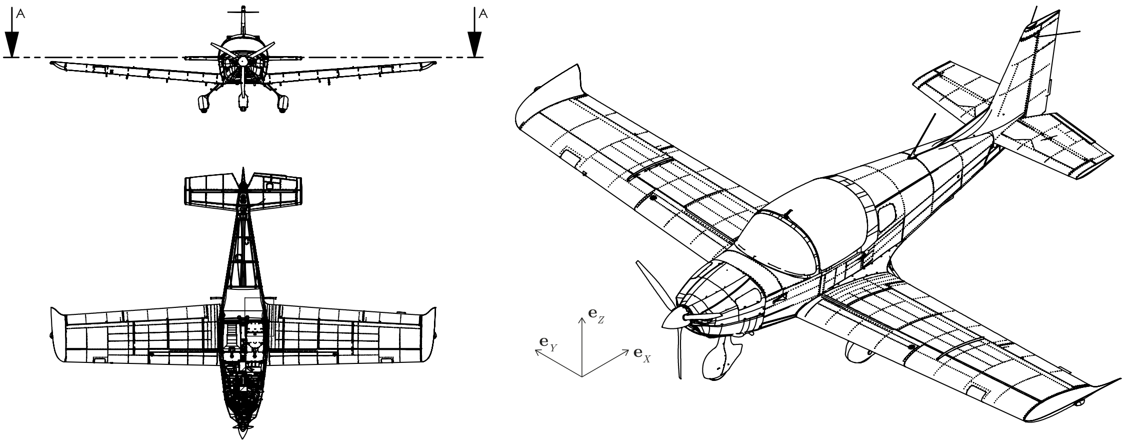

Figure 2.1: Projected views of the Sonaca 200, reproduced from [10]; in the top left corner: front view; in the bottom left corner: section A-A; on the right: isometric illustration.

it is also specified wether the fixed or the moving parts are under consideration. The control surfaces are thus referenced with ELV for the elevator and RD for the rudder. The purpose of the structural modelling is to obtain a set of vibration modes of the system using a finite element approach, including the corresponding eigenfrequencies and effective masses. These data must allow to study the fluid-structure interactions of the flying aircraft, as developed in Section 4. In order to dispose of a finite element model that is pertinent for aeroelastic analysis, its mode shapes must describe general deformations of the main structural members and not those of individual components like skin panels and small mechanical parts. From return of experience by engineers of *Sonaca Aircraft*, the full finite element model used for stress analysis is thus not the most suited for the present study. A better solution is to have a simplified description of the aircraft where the fuselage, wing, tail and vertical fin are treated as flexible beams in interaction.

	Symbol			Value		
	WNG	HTP	VTP	WNG	HTP	VTP
Span [mm]	s^{w}	s^{HTP}	s^{VTP}	20.341	7.963	20.341
Root chord [mm]	$c^{\mathrm{w}}_{\mathrm{root}}$	$c^{\mathrm{HTP}}_{\mathrm{root}}$	$c^{\mathrm{VTP}}_{\mathrm{root}}$	20.341	7.963	20.341
Tip chord [mm]	$c^{\mathrm{w}}_{\mathrm{tip}}$	$c^{\mathrm{HTP}}_{\mathrm{tip}}$	$c^{\mathrm{VTP}}_{\mathrm{tip}}$	20.341	7.963	20.341
Sweep angle [°]	$\Lambda^{\mathrm{w}}_{1/4}$	$\Lambda^{\mathrm{HTP}}_{1/4}$	$\Lambda^{\mathrm{VTP}}_{1/4}$	0	3.3	29.8
Root AOA [°]	α^{w}_{0}	$\alpha^{\mathrm{HTP}}_{0}$	$\alpha^{\mathrm{VTP}}_{0}$	1.5	-2	0
Twist angle [°]	$\varepsilon^{\mathrm{w}}_{\mathrm{g}}$	$\varepsilon^{\mathrm{HTP}}_{\mathrm{g}}$	$\varepsilon^{\mathrm{VTP}}_{\mathrm{g}}$	2	0	0

Table 1: Main geometrical parameters of the lifting surfaces, as measured on the CAD model of the Sonaca 200.

2.1.2 Principle of the structural approximation

The full set of considered flexible members is represented in Figure 2.2 including positioning and numbering of different sections. The same naming conventions as those graphically defined are conserved in the subsequent discussions. Regions of the structure that are not represented in Figure 2.2 are basically treated as rigid bodies and boundary conditions between the different elements, which are of great importance, are discussed in Section 3. In order process the considered system with the *Samcef* finite element solver, cross-sections are considered to be constant over the segments represented in Figure 2.2. For this reason, positions of the subdivisions are chosen consistent with discontinuities in

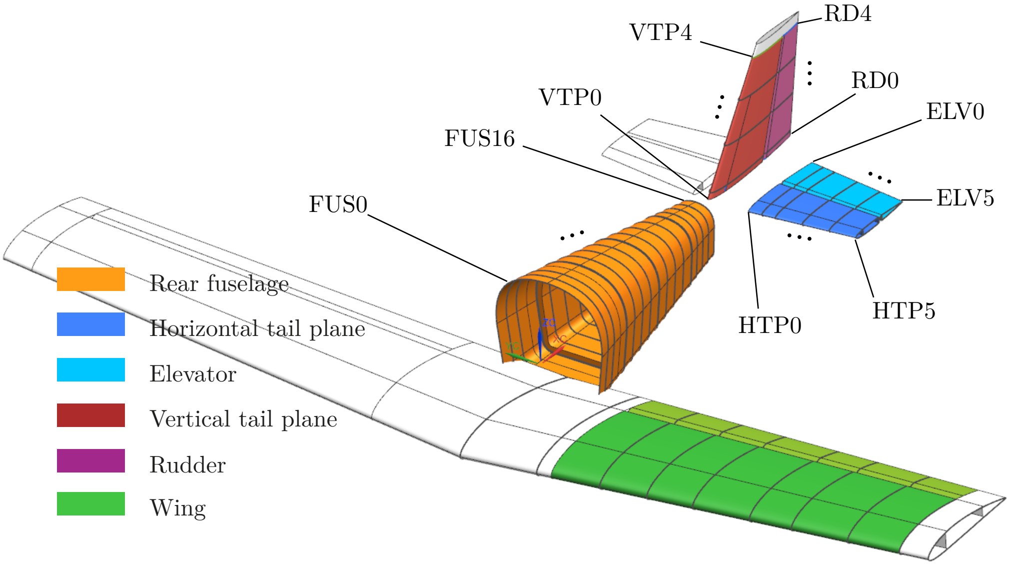

Figure 2.2: Simplified 3D representation of the main flexible members of the Sonaca 200 displaying the sections of interest; these geometries are recreated from accurate measurements on the CAD model the aircraft and are used to extract coordinates of the sections.

the internal structure, in addition to allow for a fair enough description of the proportion and size variations of external shape. The section properties at the different stations can be used to define a piecewise beam approximation of the structure. They can be obtained either by running numerous load cases on the full finite element model, or by proxy of an analytical approach. The first method was implemented to produce a finite element model of the previous iteration of this work [11]. As stated in the introduction, it was validated with experimental modal data and serves here as a foundation to add the missing parts. To save training time on the finite element analysis environment of *Sonaca Aircraft*, an analytical approach is this time chosen to tackle the rear fuselage and empennage. It is thus necessary to select the right theoretical framework, which informs on the useful parameters to extract from the geometry and material properties.

2.1.3 Choice of the theoretical beam model

Timoshenko beam elements, which take into account orientation of the cross-section with respect to the neutral axis, are good candidates since they give more physically accurate results than the classical Euler-Bernouilli model. This latter, where shear strains are neglected, would be easier to implement but a simple example can highlight obvious differences in terms of modal analysis, as shown in Table 2. The values presented here result from modal analysis of a 1 m -long, 100 mm × 100 mm C-beam with a 10 mm-thick wall in clamped-free conditions. Timoshenko and Euler-Bernouilli models are tested using *Nastran* for 10 elements over the total length in both cases. It appears that a higher

Frequencies [Hz]	f_1	f_2	f_3	f_4	f_5	f_9
E-B	88.4811	108.853	519.835	573.359	1259.67	2346.04
Timoshenko	46.7593	88.4811	136.85	213.863	241.65	519.835

Table 2: Comparison of E-B and Timoshenko beams in terms of eigenfrequencies for a C-beam in clamped-free conditions.

number of modes is obtained with the Timoshenko model in the low frequency range, hence the obvious frequency mismatch at a given mode order between the two methods. The additional eigenvalues mostly describe torsion modes that are not visible with the Bernouilli model at low frequencies. As to correlated vibration modes, which apparently share the same frequency while having here different mode orders, literature [12] [13] indicates that more or less significant frequency differences can be observed depending on the simulation settings. It can at least be noted that the 108.853 Hz frequency is here not predicted by Timoschenko. Observing the mode shapes reveals that the 136.85 Hz frequency provided by this model corresponds to a similar bending mode around the $\mathbf{e}_z$ axis as the one associated to f_2 with Euler-Bernouilli. The main difference is presence of a coupling with torsion around $\mathbf{e}_z$ in the case of Timoschenko. For all these reasons, Euler-Bernouilli model is discarded. Timoshenko beam elements are supported by the *Samcef* commercial finite element solver which allows to define custom cross-sections by encoding the proper list of parameters. As described in the software documentation [14], the properties of interest are the A cross-section area, the I_y and I_z moments of inertia in the principal transverse directions, the I_T torsional moment of area and the k_y and k_z shear factors, also expressed as reduced areas. These parameters are related to the mass and stiffness matrices of the equation of motion defined in the framework of Timoshenko theory [15], also discussed in Section 3.

2.2 Beam properties computation

Theoretical foundations detailed by Megson [1] are particularly useful to contemplate shear and torsion loading of a thin walled cross-section beam. The purpose of the following discussion is to explicitly retrieve the corresponding shear factors and torsional moment of area by pursuing the approach of the reference book. In the meantime, the cross-section area directly comes from measurements on the CAD model of the aircraft, and the principal moments of inertia are given by the classical formulas

$$I_y = \int_A z^2 dA, \tag{2.1}$$

and

$$I_z = \int_A y^2 dA. \tag{2.2}$$

2.2.1 Expression of the shear factors as a function of the shear flow

Shear factors are related to stress distribution in the beam under a shear load. Without losing generality, applying a shear load along direction $\mathbf{e}_z$ to a beam of cross-section area A actually generates some shear deflection and warping in the elastic domain, as illustrated in Figure 2.3. This deformation can be parametrized with the shear strain angle γ, which is equal to zero on the top and bottom surfaces and varies inside the profile. In this case, the avergae shear strain $\bar{\gamma}$ can be defined as the the angle of the deformed neutral axis with its original direction. Dimensional analysis then suggests a convenient relation between this average value and the norm of the shear load,

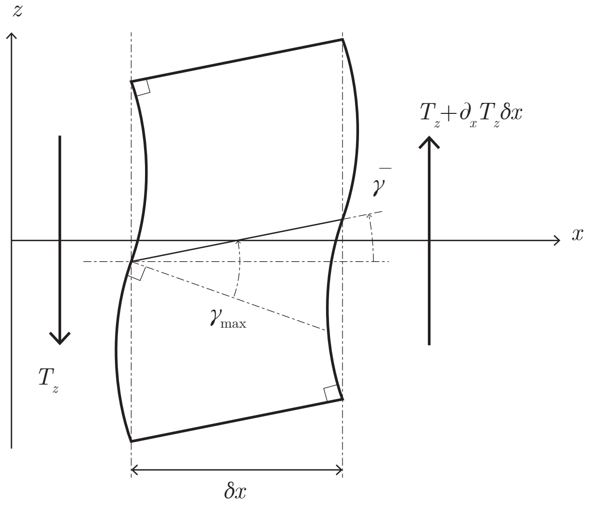

Figure 2.3: Shearing of a small symmetrical beam segment

$$\bar{\gamma} = \frac{T_z}{A'_z \mu}, \tag{2.3}$$

where $\mu = \frac{E}{2(1+\nu)}$ is the shear modulus of the material, E its Young modulus, ν its Poisson's ratio, and $A'_z = k_z A$ the reduced sectional area to take into account non-uniformity of the shear stress. It thus defines k_z the vertical shear factor. The horizontal shear factor is expressed in the exact same way in the case of an horizontal loading T_y. It can be noted that a uniform shear stress distribution would imply $\bar{\gamma} = \frac{T_z}{A\mu}$. Assuming that the deformed cross-section does remain planar with a constant shear strain $\bar{\gamma}$, the infinitesimal work of external forces on a small beam segment of length δx can be expressed as

$$\delta^2 W_{\text{ext}} = T_z \delta \frac{T_z}{A' \mu} \delta x = \delta \frac{T_z^2}{2A' \mu} \delta x. \tag{2.4}$$

Considering a conservative system, writing the balance between the work of external forces and the variation of internal energy is a way to obtain an explicit formulation for

A'_z, hence k_z (and k_y by analogy). The general expression for the infinitesimal energy variation of the beam slice is

$$\delta^2 E_{\text{int}} = \int_A \boldsymbol{\sigma} : \delta\boldsymbol{\varepsilon} dA \delta x, \tag{2.5}$$

where the double dot denotes the double contracted product between the 3×3 $\boldsymbol{\sigma}$ stress tensor, and the 3×3 $\delta\boldsymbol{\varepsilon}$ strain tensor. Regarding pure shear state in the $(\mathbf{e}_x, \mathbf{e}_z)$ plane, expression for the shear tensor in the local basis of cartesian coordinates writes

$$\delta\varepsilon = \begin{bmatrix} 0 & 0 & \delta\varepsilon_{xz} \\ 0 & 0 & 0 \\ \delta\varepsilon_{xz} & 0 & 0 \end{bmatrix}_{(x,y,z)} . \tag{2.6}$$

Besides, in the framework of thin walled cross-section beams which is used to describe aircraft components, elements of the tensor can be expressed in the basis attached to the section contour, as displayed in Figure 2.4. Tensor $\delta\varepsilon$ can be thus written in the $(\mathbf{e}_x, \mathbf{e}_s, \mathbf{e}_t)$ local basis using the base change

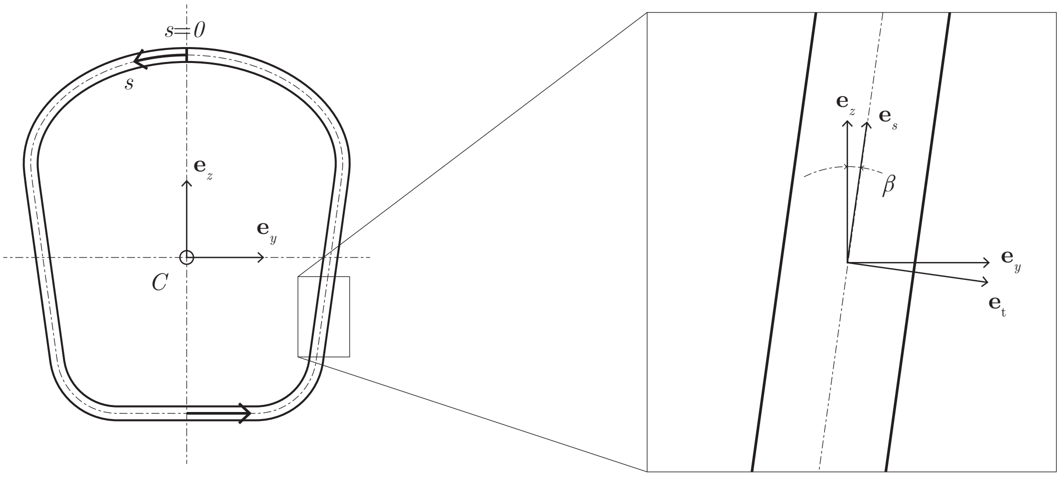

Figure 2.4: Contour parametrization and base change in a thin walled cross-section beam.

$$\delta\varepsilon_{(x,t,s)} = \mathbf{R}^{\mathrm{T}} \delta\varepsilon_{(x,y,z)} \mathbf{R}, \text{ with } \mathbf{R} = \begin{bmatrix} 1 & 0 & 0 \\ 0 & \cos(\beta) & \sin(\beta) \\ 0 & -\sin(\beta) & \cos(\beta) \end{bmatrix} . \tag{2.7}$$

It leads to

$$\delta\varepsilon = \begin{bmatrix} 0 & -\sin(\beta)\delta\varepsilon_{xz} & \cos(\beta)\delta\varepsilon_{xz} \\ -\sin(\beta)\delta\varepsilon_{xz} & 0 & 0 \\ \cos(\beta)\delta\varepsilon_{xz} & 0 & 0 \end{bmatrix}_{(x,t,s)} = \begin{bmatrix} 0 & \delta\varepsilon_{xt} & \delta\varepsilon_{xs} \\ \delta\varepsilon_{xt} & 0 & 0 \\ \delta\varepsilon_{xs} & 0 & 0 \end{bmatrix}_{(x,t,s)}, \tag{2.8}$$

where β is the angle between the section contour direction and the vertical axis. Moreover, under the hypothesis that the skin thickness is small enough to locally ensure plane stress state in the $(\mathbf{e}_x, \mathbf{e}_s)$ plane, the stress tensor can be given by

$$\sigma = \begin{bmatrix} \sigma_{xx} & 0 & \sigma_{xs} \\ 0 & 0 & 0 \\ \sigma_{xs} & 0 & \sigma_{ss} \end{bmatrix}_{(x,s,t)}. \tag{2.9}$$

Injecting Equation 2.9 and Equation 2.8 into Equation 2.5 allows to explicitly compute the tensorial product and transform the integral term into

$$\begin{aligned} \delta^2 E_{\text{int}} &= \int_A 2\sigma_{xs}\delta\varepsilon_{xs} dA\delta x \\ &= \int_A 2\sigma_{xs}\frac{\delta\sigma_{xs}}{2\mu} dA\delta x \\ &= \int_A \frac{1}{2\mu}\delta\sigma_{xs}^2 dA\delta x. \end{aligned} \tag{2.10}$$

Transition from the first to the second equality in Equation 2.10 relies on Hooke's law which prescribes that $2\delta\varepsilon_{xs} = \sigma_{xs}/\mu$. Defining now the shear flow as

$$q(s) = t\tau(s), \tag{2.11}$$

where $\tau(s) = \sigma_{xs}$, the energy variation can be formulated as an integral on the section contour,

$$\delta^2 E_{\text{int}} = \int_s \frac{1}{2\mu}\delta\left(\frac{q}{t}\right)^2 t ds\delta x = \int_s \frac{1}{2\mu t}\delta q^2 ds\delta x. \tag{2.12}$$

Writing the equality $\delta^2 E_{\text{int}} = \delta^2 W_{\text{ext}}$ then provides

$$\frac{T_z^2}{2A'_z\mu} = \int_s \frac{1}{2\mu t} q^2 ds. \tag{2.13}$$

Imposing a unit shear load while recalling that $k_z = \frac{A'_z}{A}$ also yields

$$k_z = \frac{1}{A\int_s \frac{1}{t} q^2 ds}. \tag{2.14}$$

In the same way,

$$k_y = \frac{1}{A \int_s \frac{1}{t} q^2 ds}, \tag{2.15}$$

provided that q is generated by a unit shear load in the y direction. In both cases, q remains an unknown function of s that needs to be evaluated for each particular cross-section in the different components of the Sonaca 200. In practice, the considered structures have the shape of thin walled beams reinforced with stringers described as booms. Therefore, the reduced area of the full section must include contribution of the stiffening members. As shown in Annex A, it can be analytically justified that contribution of the shear stress in the booms is noticeably negligible in front of that in the skin. A correction factor must still be used to have the proper value of the shear factor: k_z thus becomes

$$k_z^* = \frac{A}{A + A_{\text{st}}} k_z, \tag{2.16}$$

where A_{st} is the total area of the booms, which can be rather important relatively to the total area $A + A_{\text{st}}$. And similarly,

$$k_y^* = \frac{A}{A + A_{\text{st}}} k_z. \tag{2.17}$$

For the sake of simplicity, k_y^* and k_z^* are noted k_y and k_z in the following.

2.2.2 Computation of the shear flow in the fuselage sections

The rear part of the fuselage can be considered as a thin walled tapered beam with stringers modelled as cylindrical booms distributed over the skin. Geometry of the cross sections is extracted at different locations along the X direction of the structural basis as illustrated in Figure 2.5. The four main fuselage segments delimited by the RIBS03, RIBS04 and RIBS05 structural frames are divided in four equal parts and the corresponding sections indexed in the diagram are measured from the CAD file. Gathered geometrical dimensions are then exploited to recreate a simplified but accurate representation of the fuselage in 3D using sheet bodies, as represented in Figure 2.2. From this step, coordinates of the sections are extracted and processed in *Matlab*. It can be noticed that three different patterns of stringers are found along the structure to offer the proper rigidity. Any of the closed section mid-line are parametrized with a curvilinear abscissa s equal to zero at the uppermost point, similarly to the illustration of Figure 2.4. In this context, the shear flow distribution generated by an external load is expressed as the sum of two terms:

$$q(s) = q_{\text{o}}(s) + q_0, \tag{2.18}$$

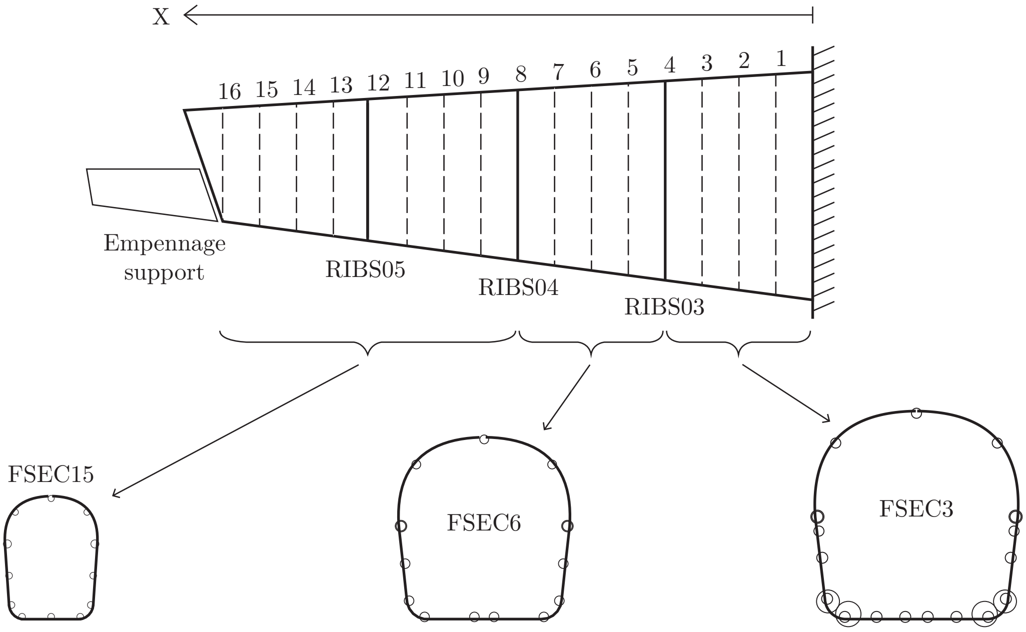

Figure 2.5: Discretization of the rear fuselage of the Sonaca 200, displaying the different sectional layouts along the X direction of the structural basis; radii of the represented boom sections are proportional to their actual area.

where $q_\mathrm{o}(s)$ is the open shear flow computed with a virtual cut in the contour at $s = 0$ and q_0 is the constant part corresponding to $q(s = 0)$. Under the assumption that the deformed sections remain planar, it can be established [1] that the open shear flow writes

$$q_\mathrm{o}(s) = q_\mathrm{o}^{T_y}(s) = -\frac{1}{I_z}\left[\int_0^s ytds + \sum_{i:s_i \leq s} y_i A_i\right] \tag{2.19}$$

in the case of a T_y load in the y direction, and

$$q_\mathrm{o}(s) = q_\mathrm{o}^{T_z}(s) = -\frac{1}{I_y}\left[\int_0^s ztds + \sum_{i:s_i \leq s} z_i A_i\right] \tag{2.20}$$

in the case of a T_z load in the z direction. The A_i coefficients here refer to the boom areas and the T_y and T_z input shear loads are taken as unit forces. The constant parts are then evaluated by enforcing a no-twist condition of the section, which holds when shear loads pass through its shear center. If it were not the case, the section would actually twist, a moment equilibrium should be verified and effects of taper should be taken into account. Developing the expression for the displacement field of a twisted closed section and using the principles of linear elasticity provides the relation

$$\oint_s \frac{q}{\mu t} ds = 2A_h \frac{\partial \theta}{\partial x}, \tag{2.21}$$

where $\frac{\partial \theta}{\partial x}$ is the twist rate of the section, $A_h = \frac{1}{2} \oint_s p ds$ is the area swept by the vector pointing from the centroid of the section to its mid-line, and p is the local distance from the centroid to the local tangent to the mid-line. Therefore, using $\frac{\partial \theta}{\partial x} = 0$ and the decomposition of Equation 2.18 in Equation 2.21 leads to

$$q_0 = -\frac{\oint_s q_{\text{o}}(s) ds}{\oint ds}. \tag{2.22}$$

Another concept related to twist is torsion inertia of the section. It is defined to describe the amount of deformation that a M_x axial moment can generate:

$$I_{\text{T}} = \frac{M_x}{\theta_{,x} \mu}. \tag{2.23}$$

Under pure torsion, shear stress in the contour is constant. With $q = q_0$, it can be deduced from Equation 2.21 that

$$\theta_{,x} = \frac{q_0}{2A_h \mu} \oint_s \frac{1}{t} ds. \tag{2.24}$$

Furthermore

$$M_x = \oint pq ds = q_0 \oint p ds = 2A_h q_0. \tag{2.25}$$

Consequently:

$$I_{\text{T}} = \frac{4A_h^2}{\oint \frac{1}{t} ds}. \tag{2.26}$$

Coming back to shear flow distribution, results of Equations 2.19, 2.20 and 2.22 can be implemented in *Matlab* to evaluate $q(s)$ over any of the measured fuselage sections. The dedicated function is called `secanalysis.m` (and `secanalysis_multiCell.m` for the lifting surfaces). Figure 2.6 displays the computed shear flow along the contour of FUS3 and indicates the placement of shear center S with respect to centroid C. Symmetry of the distribution is clearly visible, which should be expected from the horizontal symmetry of the fuselage section. As mentioned above, S corresponds to the point verifying that shear loads passing through it do not generate twist in the section. Its coordinates can be found by writing the balance equations for the two load cases:

$$y_S = \oint_s q^{T_z} p ds, \tag{2.27}$$

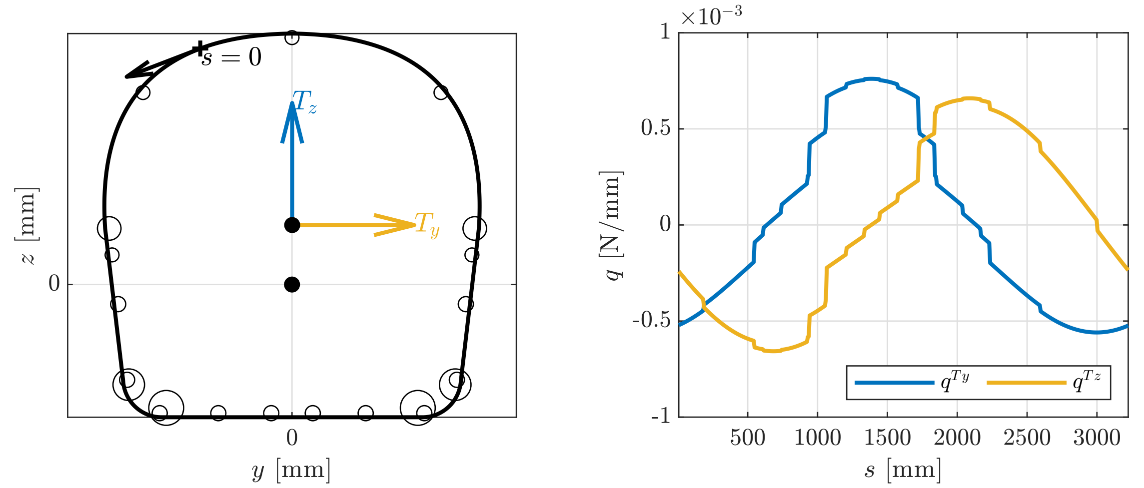

(a) Geometry of FUS3 with the applied shear loads, centroid and shear center

(b) Computed shear flow around the contour of FUS3.

Figure 2.6: Results of the 2D analytical approach for section FUS3; the geometrical representation of FUS3 is true-to-scale with the actual positions of the centroid and shear center respectively represented at the C and S points.

and

$$z_S = \oint_s q^{T_y} p ds, \tag{2.28}$$

where q^{T_z} is the shear flow induced by T_z and q^{T_y} is the shear flow induced by T_y. Position of the shear center provides a first degree of validation for the structural analysis since it must lie on the eventual symmetry axes of the section. It can here be verified that y_S is very close to zero in comparison to the section width, which is consistent with the fact that $(C, \mathbf{e}_z)$ is a symmetry axis. This observation can be done for all the processed sections as presented in Figure 2.15b showing that the position errors remains lower than 0.5% along the fuselage. It should also be checked that shear loads are well recovered from the shear stress distribution, which can be performed by calculating

$$\tilde{T}_y = \int_s q(s)\mathbf{ds} \cdot \mathbf{e}_y, \tag{2.29}$$

and

$$\tilde{T}_z = \int_s q(s)\mathbf{ds} \cdot \mathbf{e}_z, \tag{2.30}$$

where $\mathbf{ds} = ds\mathbf{e}_s$ is the contour orientation vector. As T_y and T_z are assumed to be unit shear loads, all values of $\tilde{T}_y$ and $\tilde{T}_z$ should be very close to 1. Small errors may occur due to the approximation of integral terms by discrete sums in the computation code. Apart from this, it appears, as shown in Figure 2.7, that the implemented structural analysis

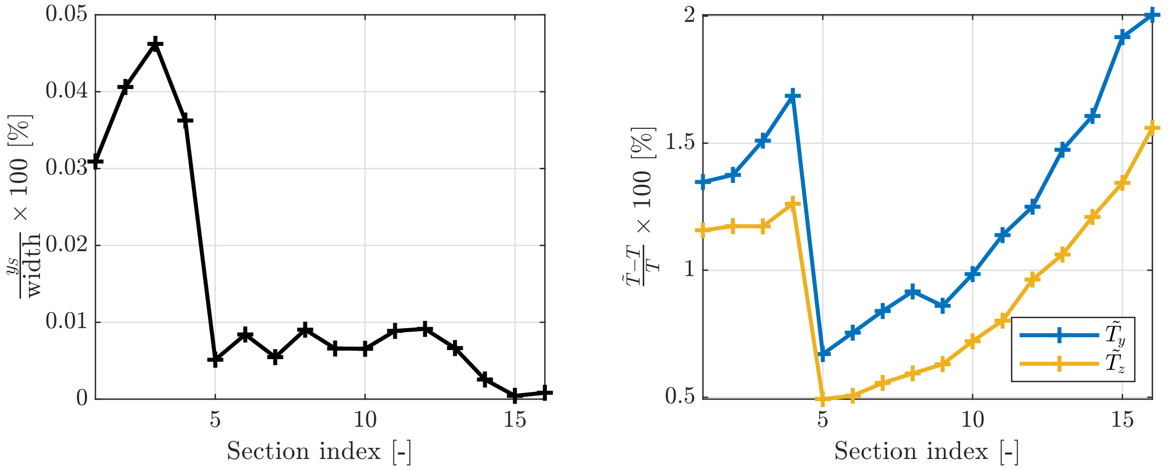

(a) Shear center position error *vs* Section index

(b) Recovered shear load error *vs* Section index

Figure 2.7: Verification of the computed shear flow distribution in terms of recovered shear loads and position of the shear center.

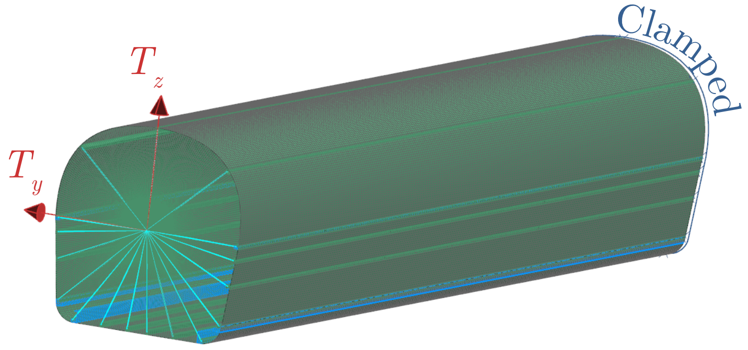

Figure 2.8: Finite element model of the extruded version of FSEC3 with the applied boundary conditions and shear loads.

method provides expected results. Deviations in terms of shear loads actually remain below 2% over the full set of considered sections.

Error curves presented here above support reliability of the implemented 2D approach but it is especially interesting to see how relevant this method is to describe the 3D structure. To have some reference data in terms of shear flow distribution, a finite element model of an extruded version of FUS3 is created using first order shell elements for the skin and rod elements for the booms. As shown in Figure 2.8, one side of the structure is clamped in the inertial frame and the other is considered as a rigid body connected to a single node at the shear center where forces are applied. Both load cases are simulated with nominal values of $T_y = T_z = 1000N$. The shear stresses distribution around the cross section contour are subsequently extracted at a location not too close to the extremities to avoid

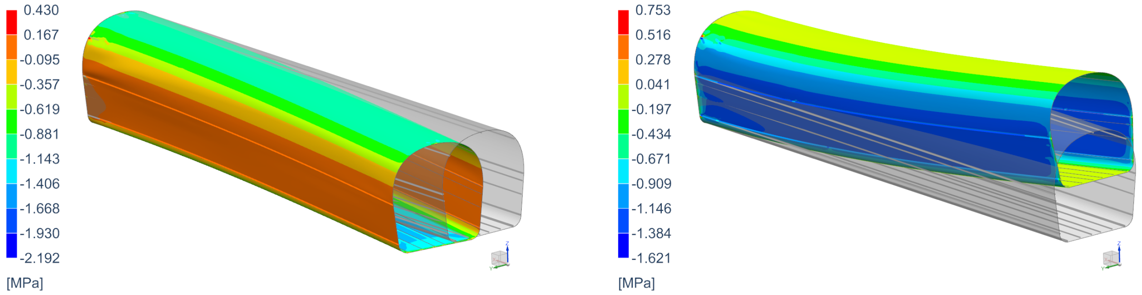

(a) σ_{xy} in the skin under horizontal loading. (b) σ_{xz} in the skin under vertical loading.

Figure 2.9: Stress distribution over the finite element model based on FUS3.

singularities. It was verified that the exact axial coordinate of the considered station in the finite element model has almost no influence over the gathered values. This can be visually confirmed with the provided stress fields, as shown in Figure 2.9. The stress tensors provided in cartesian coordinates by the software are beforehand expressed in the local $(\mathbf{e}_x, \mathbf{e}_t, \mathbf{e}_s)$ basis in order to retrieve the σ_{xs} shear stress in the skin mid-surface. The base change is similar to Equation 2.7 at the difference that the angle of rotation is of opposite sign. It gives here

$$\sigma_{(x,t,s)} = \begin{bmatrix} \sigma_{xx} & 0 & c\sigma_{xz} - s\sigma_{xy} \\ 0 & 0 & 0 \\ c\sigma_{xz} - s\sigma_{xy} & 0 & c^2\sigma_{zz} + s^2\sigma_{yy} - 2cs\sigma_{yz} \end{bmatrix}_{(x,t,s)}, \tag{2.31}$$

where $c = \cos(\beta)$, $s = \sin(\beta)$, and the zero elements come from the plane stress state in the skin. The shear stress σ_{xs} can be identified as $\sigma_{xs} = \cos(\beta)\sigma_{xz} - \sin(\beta)\sigma_{xy}$ and the corresponding shear flow is simply obtained with $q = t\sigma_{xs}$. The simulated stress distribution is then plotted on top of the analytical one and it can be observed in Figure 2.10 that the two sets of data are quite close to each other. It thus seems to ground the relevance of the 2D approach. Applying the result of Equations 2.14 and 2.15 also yields a quantitative comparison between the 2D analytical approach and the 3D numerical results. As presented in Table 3, the resulting shear factors are fairly similar, with a maximum relative error of 7%, which tends to further confirm the implemented analytical method. It can be mentioned that the same process as the one described for FSEC3 was repeated for FSEC5 to check reliability of the presented solutions. Finally, it must be ensured that the assembly of the beam elements containing the section properties gives a satisfying description of the actual fuselage. The 1D finite element model of the rear fuselage is obtained by gathering the parameters found with the analytical approach and summarized in Figure 2.11. It can be noticed that the transitions between the three

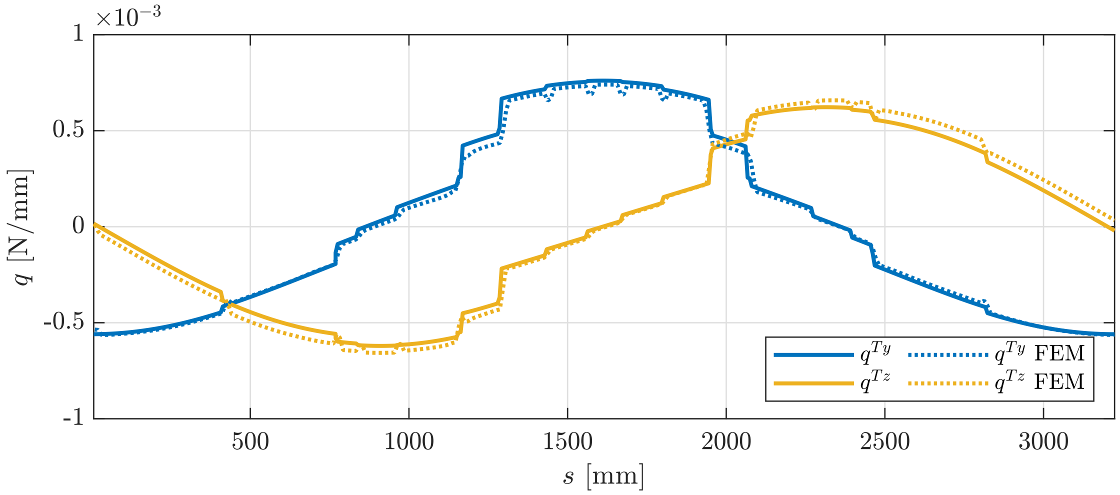

(a) Analytically computed shear flow and finite element results around the contour of FUS3.

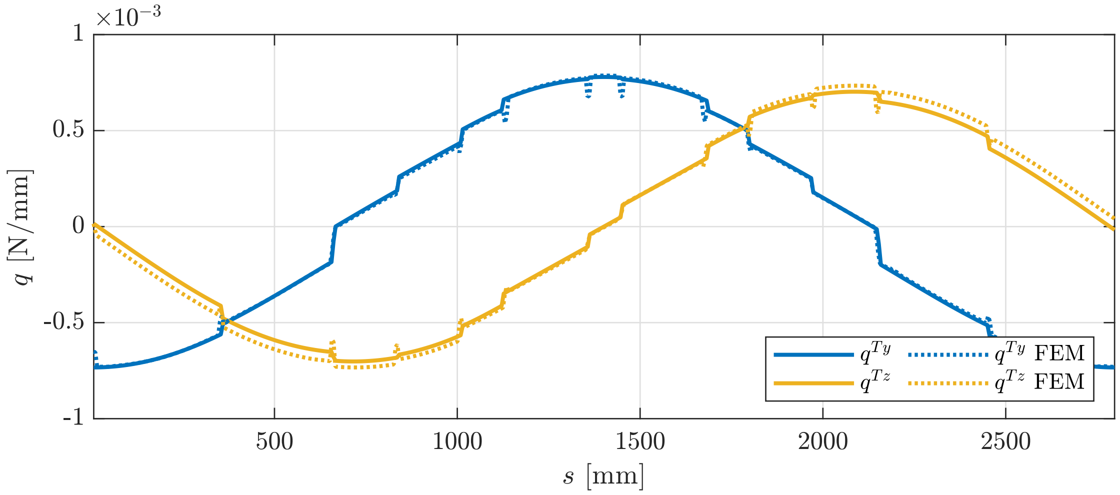

(b) Analytically computed shear flow and finite element results around the contour of FUS5.

Figure 2.10: Comparison between the analytical and finite element approach at two different stations of the rear fuselage.

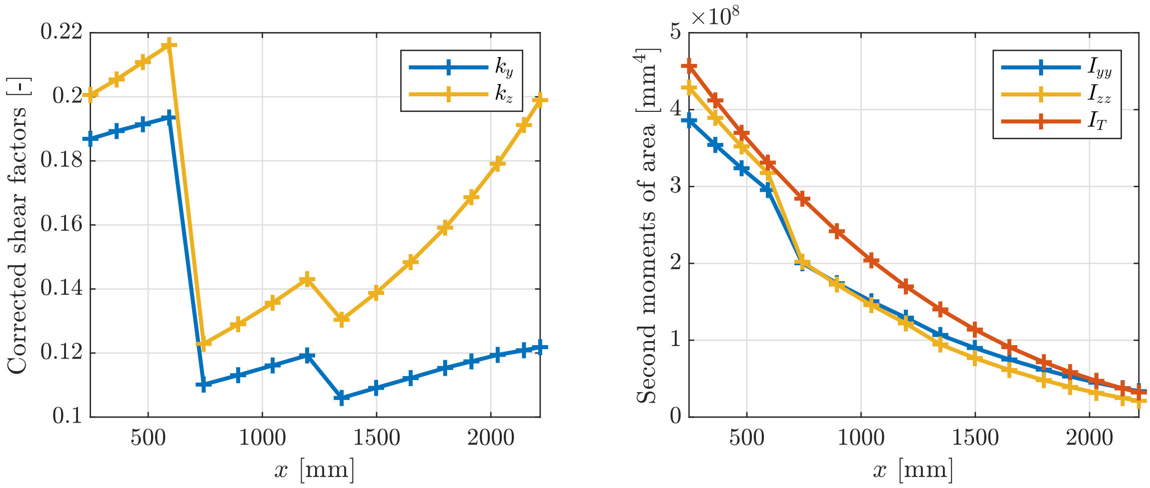

(a) Shear factors along the rear fuselage. (b) Inertia along the rear fuselage.

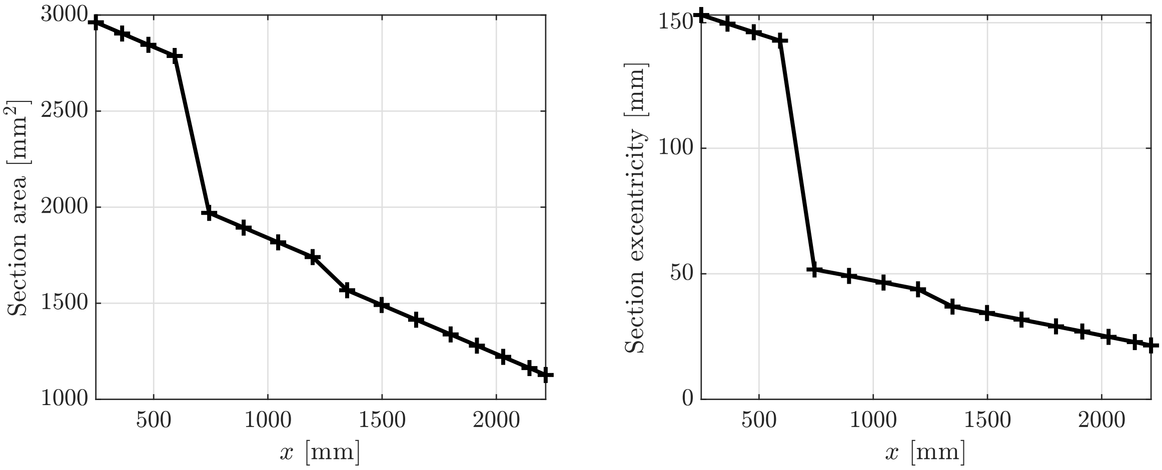

(c) Areas along the rear fuselage. (d) Excentricity along the rear fuselage..

Figure 2.11: Distribution of the different useful sectional parameters along the rear fuselage of the Sonaca 200, as used for Timoshenko beam elements creation in *Samcef*.

Section	FEM results		Analytical results	
	k_y [-]	k_z [-]	k_y [-]	k_z [-]
FSEC3	0.6989	0.7104	0.6837	0.7527
(Err [%])	-	-	(2.2)	(6.0)
FSEC5	0.5867	0.6322	0.5823	0.6762
(Err [%])	-	-	(0.8)	(7.0)

Table 3: Comparison between the analytically computed shear factors and the finite element analysis results.

different regions of the rear fuselage clearly translate as discontinuities in the mechanical properties. The first four sections actually have a much higher area and subsequently higher bending moments of area. It also illustrates in terms of shear factors with significant jumps at each transition. The shear factor in the z direction remains higher than the one in the y direction and this difference increases as the the fuselage section becomes more and more narrow towards the tip. It can be explained with Equation 2.3 which shows that the shear deformation decreases when the reduced area increases. So, it can be expected that the reduction factor increases in the direction where the structure becomes stiffer, and thus less prone to shear deformation. Furthermore, a simplified 3D finite element model of this part of the airplane is also completed. It takes into account taper of the structure and accurate positioning of the sections with respect to each other. It uses the same kind of elements as the mesh presented in figure 2.8 and similar boundary conditions are imposed at the two extremities. The same configuration is reproduced with the beam model and in both cases, shear loads $T_y = 1000$ N, $T_z = 1000$ N and a torsion moment $M_x = 1000$ dN × m are applied at the tip of the structure. Values of the maximum measured displacement are reported in Table 4. It can be observed that the two models display similar values, which was the point of all the steps described here above. It can thus be conceded that the simplified model provides a relatively accurate image of the complete structure while being more adapted for flutter analysis due to the reasons mentioned in the Section 2.1.

	u_y [mm]	u_z [mm]	θ_x [°]
3D model	0.302	0.299	0.416
1D model	0.316	0.290	0.447
(Err [%])	(4.6)	(3.0)	(7.6)

Table 4: Comparison of the fuselage deflection between the 3D and 1D finite element models.

2.2.3 Computation of the shear flow in the empennage sections: Horizontal tail plane

Computation of the shear factors in the lifting surfaces follows the same principles as for the fuselage. The only difference is that the cross-sections are composed of multiple cells delimited by the wing spars. A convenient approach is to follow the methodology described by Megson [1] in the case of a wing profile with multiple spars. The first step remains computing the open shear flow in the skin contour by using virtual cuts on the upper walls as illustrated in figure 2.12. Free branches are processed in the first place using the same exact formulas as in Equations 2.19 and 2.20. Shear flow on branches located between two intersections is then computed using a conservation relationship at the nodes. Keeping the notations introduced in Figure 2.13, it is actually verified that

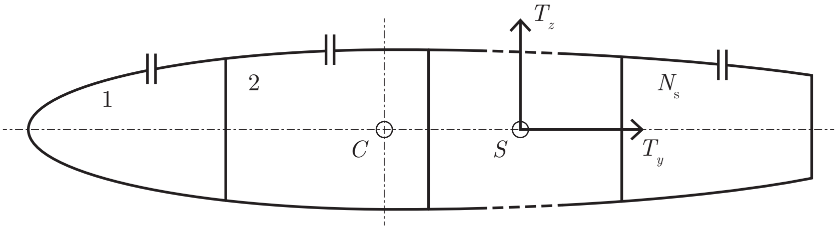

Figure 2.12: N_c-cell wing section subjected to shear loads passing through its shear center.

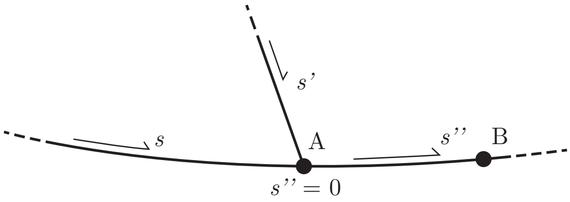

Figure 2.13: Parametrization of the section contour around a node.

$$q_o(s''_B) = q_o(s_A) + q_o(s'_A) + \int_0^{s''_B} \partial_{s''} q_o(s'') ds'', \tag{2.32}$$

where $q_o(s''_B)$ is the shear flow at the abscissa of point B in the third branch, $q_o(s_A)$ is the shear flow at the abscissa of point A in the first branch and $q_o(s'_A)$ is the shear flow at the abscissa of point A in the second branch. The integral term is here expressed in its most general form and can be computed with Equations 2.19 or 2.20 depending on the load case. Once the open shear flows are computed, the constant terms corresponding to the values a the cuts are found with the no-twist condition. It must here be applied to each cell of the section by taking into account contributions of the neighbour cells. For the i^{th} cell, $i \in \{1, ..., N_{\text{c}}\}$, this relation writes

$$\theta_{,x} = \frac{1}{2A_h^i \mu_{\text{ref}}} \left[-q^{i-1}(0)\bar{l}^i_{i-1} + q^i(0)\bar{l}^i + \oint_{\text{cell}i} \frac{q_{\text{o}}}{t\frac{\mu}{\mu_{\text{ref}}}} + q^{i+1}(0)\bar{l}^{i+1}_i \right] = 0, \tag{2.33}$$

where notation $\bar{l} = l/t$ indicates the reduced length of a given branch arc of length l and thickness t, $\bar{l}^i$ is the reduced perimeter of cell i, and $\bar{l}^i_{i-1}$ (resp. $\bar{l}^{i+1}_i$) is the reduced length of the dividing wall between cell i and cell $i-1$ (resp. i and $i+1$). Assuming that all the cells are horizontally aligned, the full system of equations can be put in the form

$$\begin{bmatrix} \bar{l}^1 & -\bar{l}^2_1 & & & & (0) \\ -\bar{l}^2_1 & \bar{l}^2 & \ddots & & & \\ & \ddots & \ddots & -\bar{l}^i_{i-1} & & \\ & & -\bar{l}^i_{i-1} & \bar{l}^i & \ddots & \\ & & & \ddots & \ddots & -\bar{l}^{N_{\text{c}}}_{N_{\text{c}}-1} \\ (0) & & & & -\bar{l}^{N_{\text{c}}}_{N_{\text{c}}-1} & \bar{l}^{N_{\text{c}}} \end{bmatrix} \left\{ \begin{matrix} q(0)^1 \\ q(0)^2 \\ \vdots \\ q(0)^i \\ \vdots \\ q(0)^{N_{\text{c}}} \end{matrix} \right\} = - \left\{ \begin{matrix} \oint_{\text{cell1}}(...) \\ \oint_{\text{cell2}}(...) \\ \vdots \\ \oint_{\text{cell}i}(...) \\ \vdots \\ \oint_{\text{cell}N_{\text{c}}}(...) \end{matrix} \right\}, \tag{2.34}$$

and can easily be solved by inverting the tri-diagonal matrix. This method provides the closed shear flow in all the walls of the section and the shear factors can be retrieved using Equations 2.19 and 2.20. Function `secanalysis_multiCell.m` is programmed in *Matlab* to perform this task. The horizontal tail plane being separated between the static structure and the elevator, the two regions of the section are separately studied. Figure 2.14 displays the results obtained for HTP3. Obvious discontinuities in the individual shear flow distributions of each cell are due to summations at the intersection nodes. This is why symmetry of the distribution is not as visible as for the fuselage sections in this display. Nonetheless, it appears that the shear center lies as expected on the horizontal symmetry axis in both parts of the horizontal tail plane. Its position is computed as described for the fuselage with the difference that orientation of the contour with respect to the centroid must be carefully taken into account. Error in terms of z_{S} remains very small for all the considered sections in this component of the aircraft, as it can be seen in Figure 2.15. Besides, shear flow in the section can also be integrated to verify that shear loads are correctly recovered. It appears in the graph of Figure 2.15 that the inaccuracy barely reaches 1% of the applied shear load which is considered satisfactory. The portion of the lifting surface characterized with the approach presented in this paragraph is then modelled as a system of two parallel beams possessing the properties displayed in Figures 2.16 and 2.17.

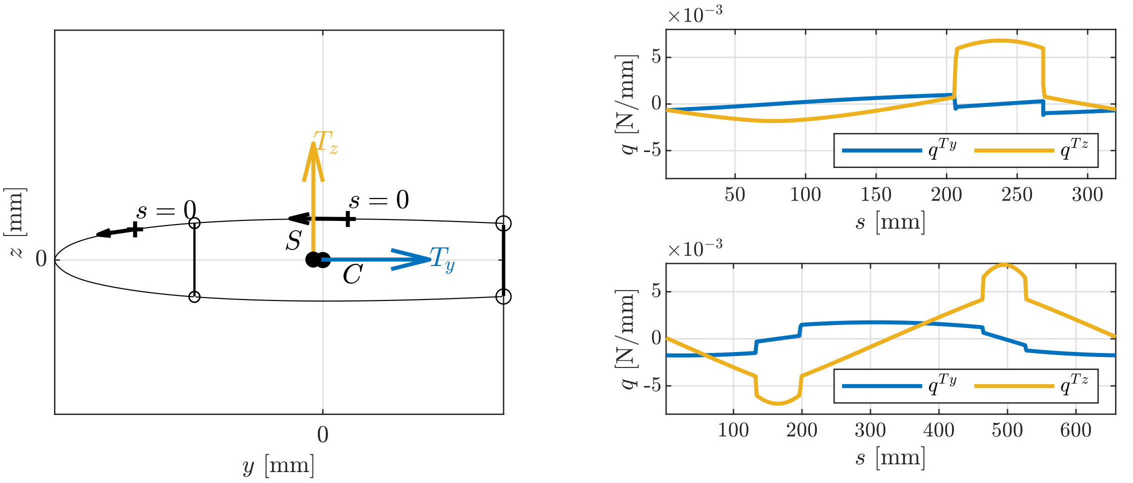

(a) Geometry of HTP3 with the applied shear loads, centroid and shear center.

(b) Computed shear flow around the contour of HTP3.

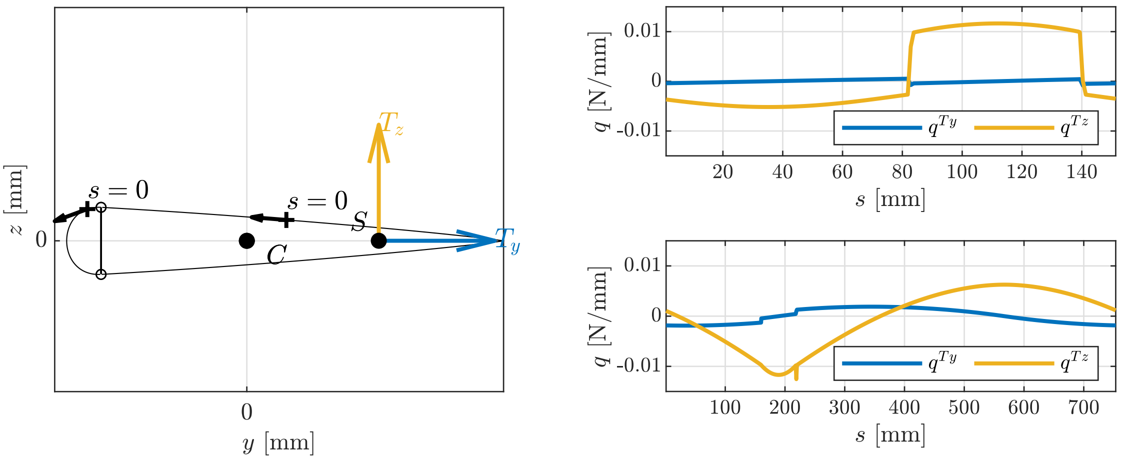

(c) Geometry of ELV3 with the applied shear loads, centroid and shear center.

(d) Computed shear flow around the contour of ELV3.

Figure 2.14: Results of the 2D analytical approach for sections HTP3 and ELV3; the geometrical representations are true-to-scale with the actual positions of the centroid and shear center respectively represented at the C and S points.

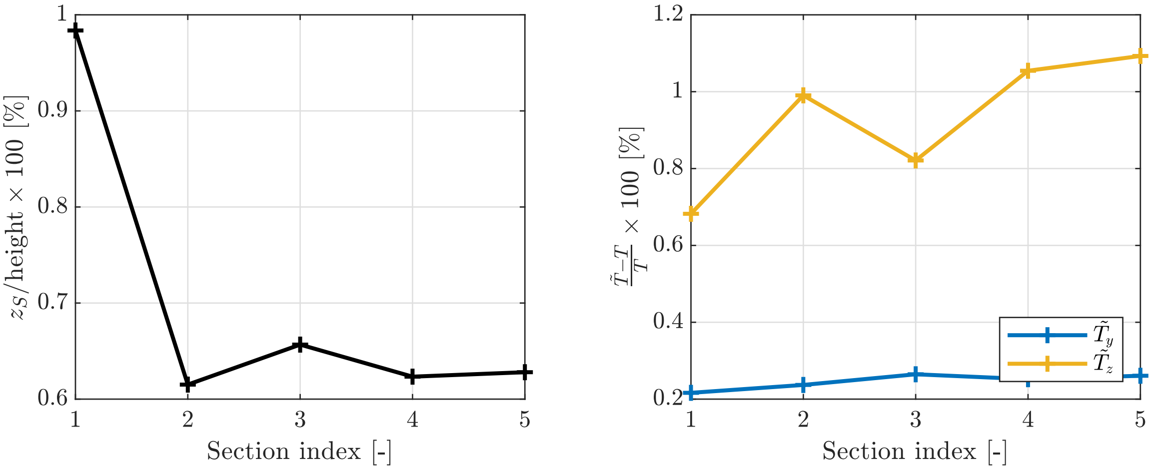

(a) Shear center position error *vs* Section index

(b) Recovered shear load error *vs* Section index

Figure 2.15: Verification of the computed shear flow distribution in terms of recovered shear loads and position of the shear center.

2.2.4 Computation of the shear flow in the empennage sections: vertical tail plane

Computation of the shear flow in the vertical tail plane follows the same rules as for the horizontal tail plane. The only difference is the variation of the section pattern close to the tip of the structure. Computation results are presented in Figures **??** and 2.19. As mentioned earlier for HTP, presence of large stiffening elements at the root of the vertical tail plane induces a larger bending inertia. Elongated shape of the profiles also explains why k_y appears much higher than k_z. Moreover, errors in terms of shear center position and recovered shear loads are still very small.

2.3 Conclusions

The method described in this section might be an alternative to the use of a complete finite element model to evaluate mechanical properties of the structures. It however requires a fair amount of programming to apply the analytical relations to the full set of data in a proper way, especially for multi-cell cross-sections. Final results appear to be consistent with the 3D structure in terms of static behavior, which is satisfactory. It remains that modal parameters of the system are the desired properties. The following section is thus dedicated to defining the actual finite element model of the Sonaca 200 and to comparing the numerical solutions to available reference material.

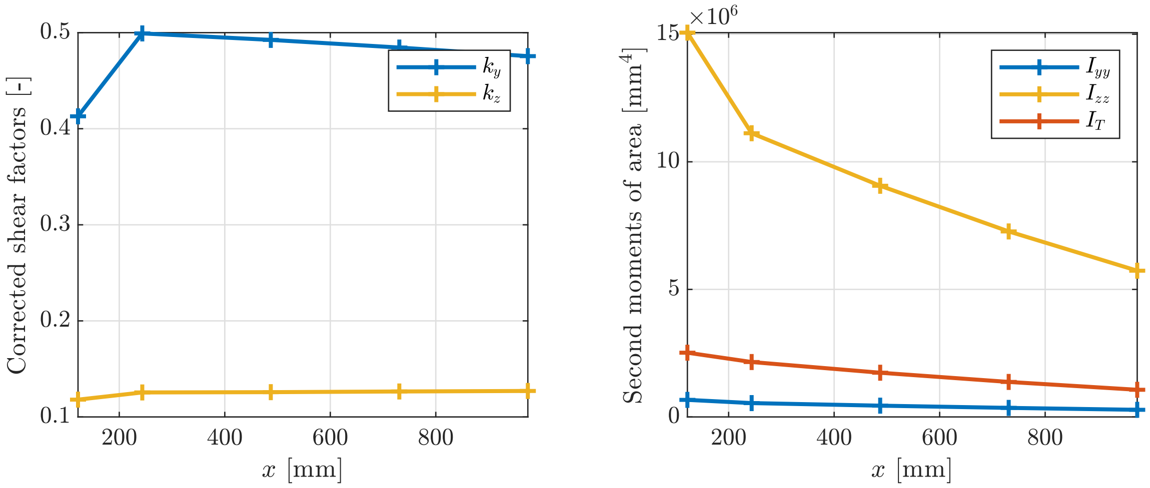

(a) Values of the shear factors along the half span of the horizontal tail plane.

(b) Inertia of the sections along the half span of the horizontal tail plane.

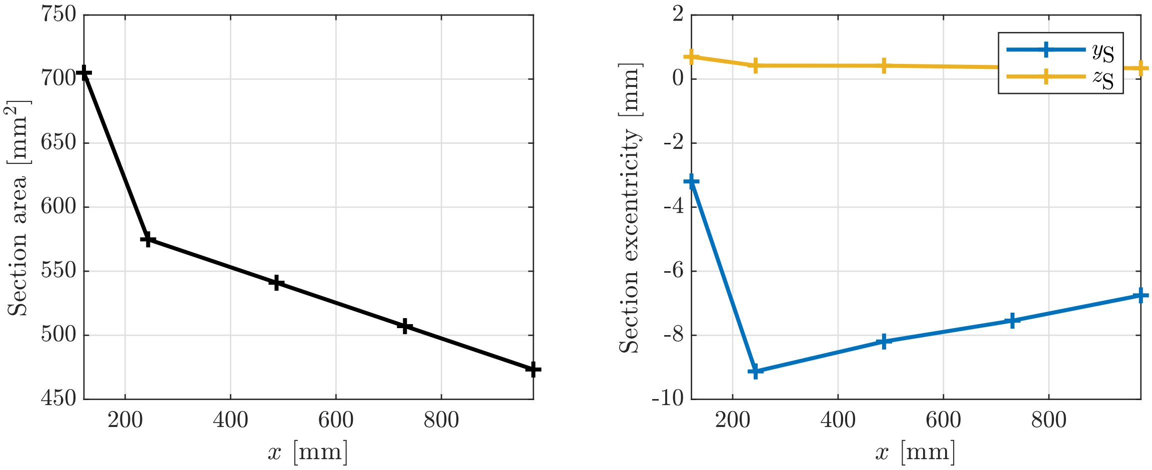

(c) Areas of the sections along the half span of the horizontal tail plane.

(d) Excentricity of the sections along the half span of the horizontal tail plane.

Figure 2.16: Horizontal tail plane (HTP): distribution of the different useful sectional parameters, as used for Timoshenko beam elements creation in *Samcef*.

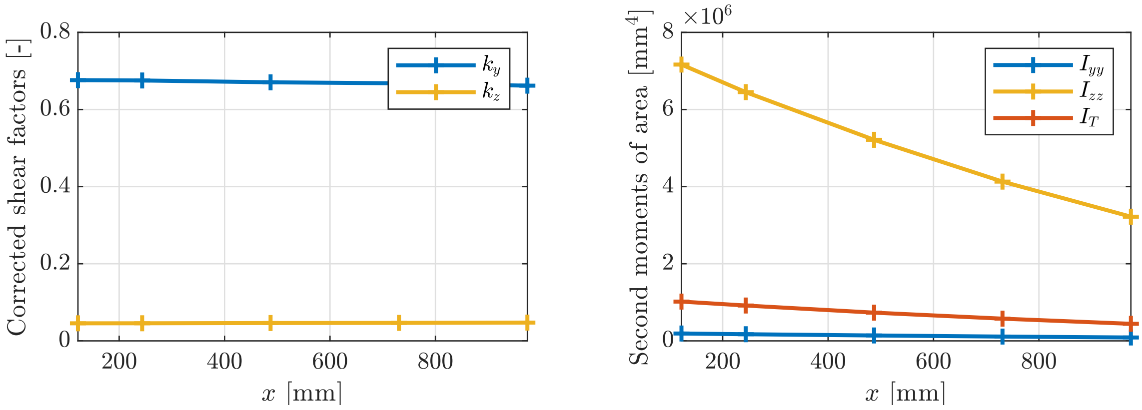

(a) Shear factors along ELV. (b) Inertia along ELV.

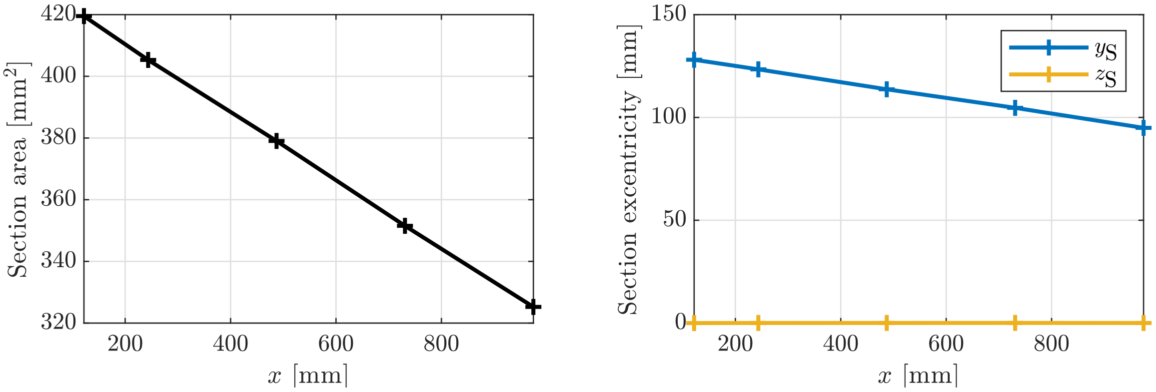

(c) Cross-sectional area along ELV. (d) Excentricity along ELV.

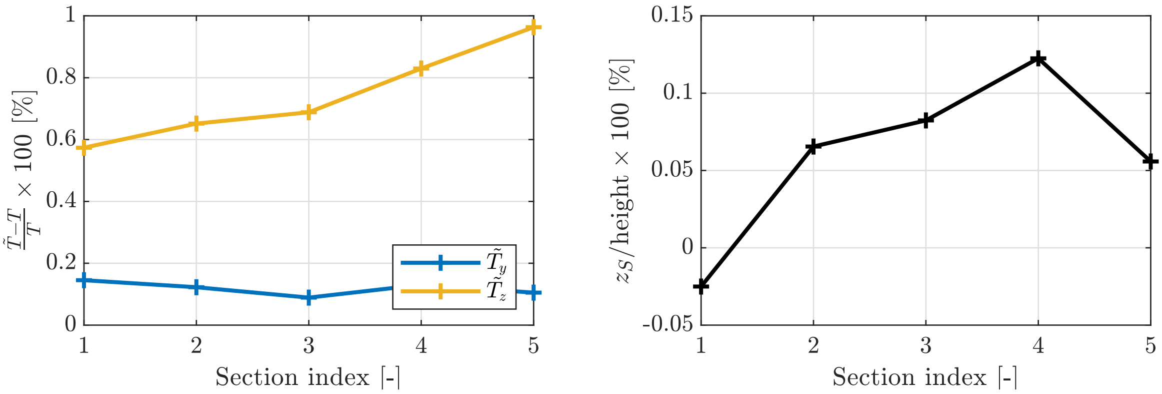

(e) Recovered shear load error along ELV. (f) Shear center position error along ELV.

Figure 2.17: Elevator (ELV): distribution of the different useful sectional parameters, as used for Timoshenko beam elements creation in *Samcef*.

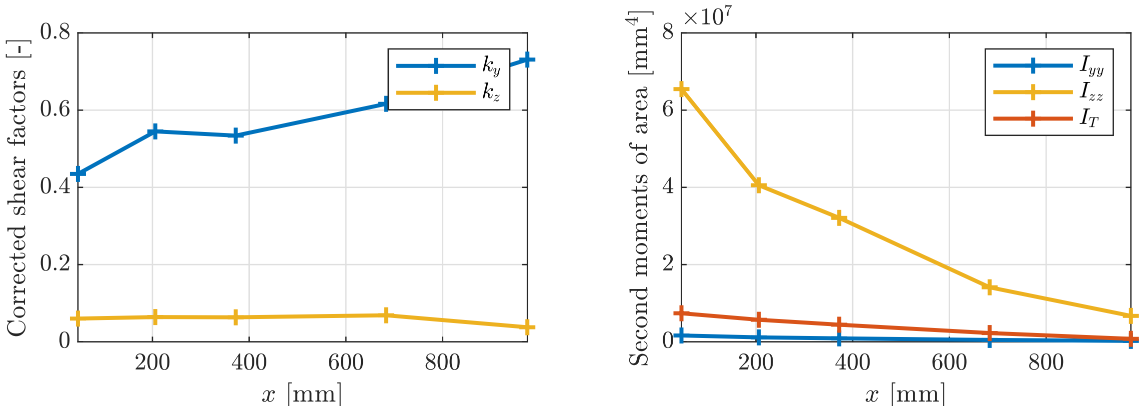

(a) Shear factors along VTP.

(b) Inertia along VTP.

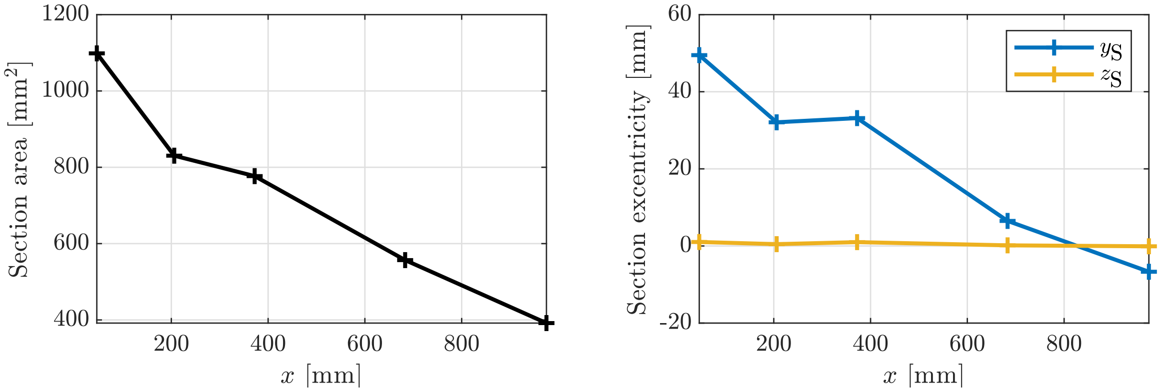

(c) Cross-sectional area along RD.

(d) Excentricity along VTP.

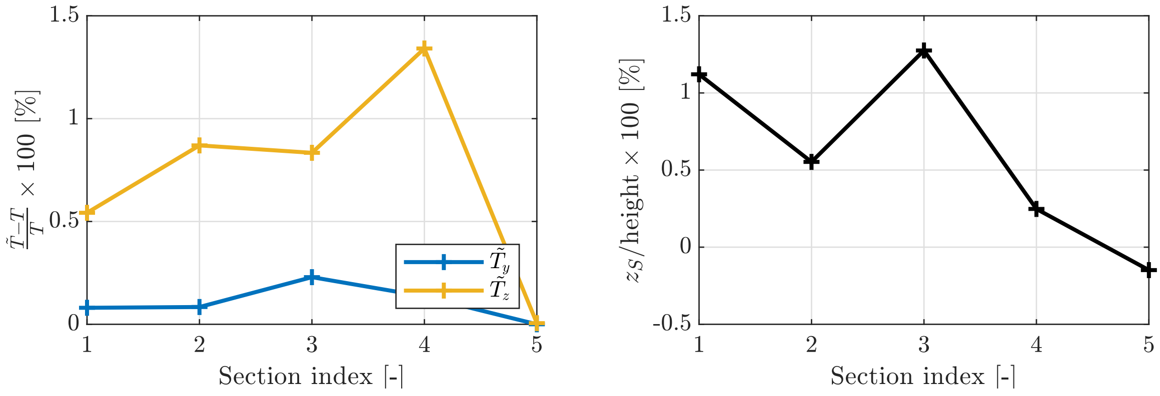

(e) Recovered shear load error along VTP.

(f) Shear center position error along VTP.

Figure 2.18: Vertical Tail Plane (VTP): distribution of the different useful sectional parameters, as used for Timoshenko beam elements creation in *Samcef*.

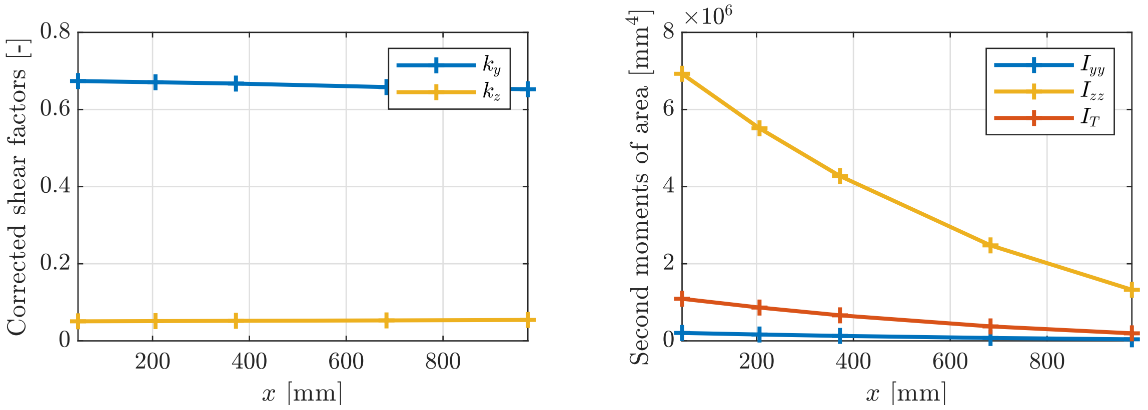

(a) Shear factors along RD. (b) Inertia along RD.

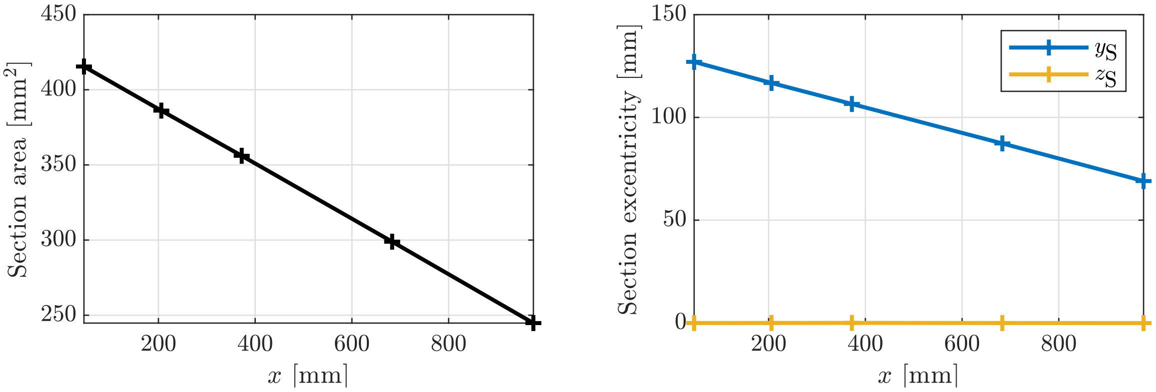

(c) Cross-sectional area along RD. (d) Excentricity along RD.

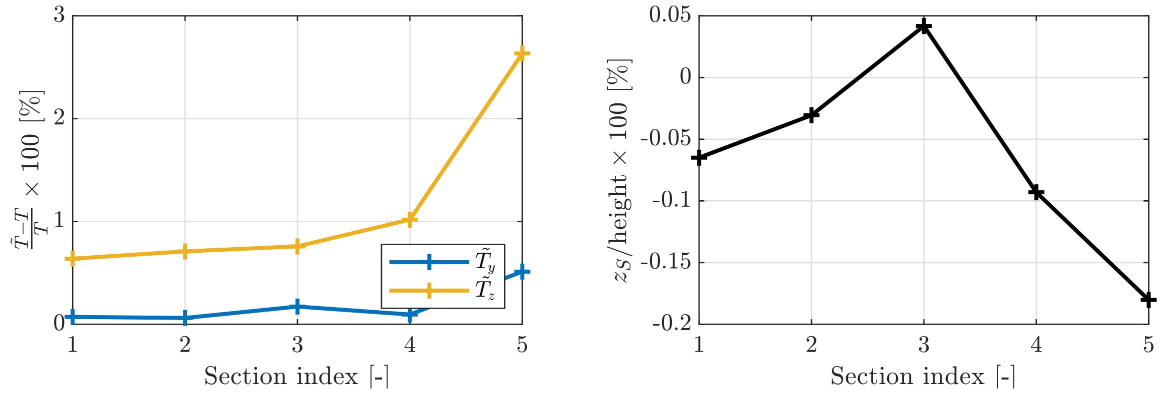

(e) Recovered shear load error along RD. (f) Shear center position error along RD.

Figure 2.19: Rudder (RD): distribution of the different useful sectional parameters, as used for Timoshenko beam elements creation in *Samcef*.

3 Numerical modal analysis of the airplane

Partial ground vibration testing results have been provided by the *LeichtwerkAG* company in addition to their report, which offers some material to compare with the simulations. As it is explained in detail in Section 4, only the out-of-plane displacement components of the eigenvectors are useful for flutter analysis. It remains that the full eigenvectors with six degrees of freedom per node are here computed to ensure that the model behaves as realistically as possible.

3.1 Theoretical principles of numerical modal analysis

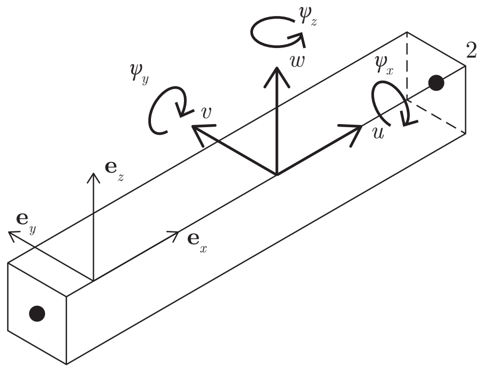

Figure 3.1: Nomenclature used for beam elements cinematic description.

All beam elements of the structural model are described by a pair of nodes, each of them having six degrees of freedom: three rotations and three translations in the orthonormal local basis $(\mathbf{e}_x, \mathbf{e}_y, \mathbf{e}_z)$ as shown in Figure 3.1. Shear angles are here designated with variables ψ_y and ψ_z. To take into account elemental physical properties, mass and stiffness matrices have to be generated. The bending energies in planes $(\mathbf{e}_x, \mathbf{e}_y)$ and $(\mathbf{e}_x, \mathbf{e}_z)$, as well as the extension and torsional deformation energies of the Timoshenko beams derive from the following integrals[16]:

$$\mathcal{V}_{\text{bend}xy} = \frac{1}{2}\int_0^l EI_z\Big(\frac{\partial \psi_z}{\partial x}\Big)^2 + \mu A'_z\left(-\psi_z + \frac{\partial w}{\partial x}\right)^2 dx, \tag{3.1}$$

$$\mathcal{V}_{\text{bend}xz} = \frac{1}{2}\int_0^l EI_y\Big(\frac{\partial \psi_y}{\partial x}\Big)^2 + \mu A'_y\left(-\psi_y + \frac{\partial v}{\partial x}\right)^2 dx, \tag{3.2}$$

$$\mathcal{V}_{\text{ext}} = \frac{1}{2}\int_0^l EA\Big(\frac{\partial u}{\partial x}\Big)^2 dx, \tag{3.3}$$

$$\mathcal{V}_{\text{torsion}} = \frac{1}{2}\int_0^l \mu I_{\text{T}}\Big(\frac{\partial \Psi_x}{\partial x}\Big)^2 dx. \tag{3.4}$$

It can be noted that the bending energies take into account both bending of the neutral fiber and shearing of the cross-section. Sum of the energy terms gives the internal potential energy $\mathcal{V}_{\text{int}}$ of the deformed beam element. As the elemental displacement fields are described by proxy of linear shape functions, development of the integral terms can provide a matrix form of the potential:

$$\mathcal{V}_{int,e} = \frac{1}{2}\mathbf{q}_{eL}^T \mathcal{K}_{eL}\mathbf{q}_{eL}, \tag{3.5}$$

where $\mathbf{q}_{eL}$ is a column vector containing the twelve degrees of freedom of the beam element:

$$\mathbf{q}_{eL} = (u_1, v_1, w_1, \psi_{x1}, \psi_{y_1}, \psi_{z1}, u_2, v_2, w_2, \psi_{x2}, \psi_{y_2}, \psi_{z2})^T. \tag{3.6}$$

Kinetic energy of the beam element, which is defined by

$$\mathcal{T}_e = \frac{1}{2}\int_0^l m(\dot{u}^2 + \dot{v}^2 + \dot{w}^2 +)dx + \frac{1}{2}\int_0^l m r_t^2 \dot{\Psi}_x{}^2 dx, \tag{3.7}$$

can similarly be written using an elementary mass matrix M_{eL} :

$$\mathcal{T}_e = \frac{1}{2}\dot{\mathbf{q}}_{el}{}^T \mathcal{M}_{el}\dot{\mathbf{q}}_{el}. \tag{3.8}$$

The matrices can then be expressed in the structural basis and assembled to form the structural $\mathcal{M}$ and $\mathcal{K}$ mass and stiffness matrices. The assembly process is not detailed here but more information can be found in that regard in the reference book by Gerardin [16]. At this point, Hamilton's principle can theoretically be applied for the whole structure in absence of external forces:

$$\delta \int_{t_1}^{t_2} \Big(\frac{1}{2}\dot{\mathbf{q}}^T \mathcal{M}\dot{\mathbf{q}} - \frac{1}{2}\mathbf{q}^T \mathcal{K}\mathbf{q}\Big) dt = 0, \tag{3.9}$$

which leads to the structural equation of motion

$$\mathcal{M}\ddot{\mathbf{q}} + \mathcal{K}\mathbf{q} = \mathbf{0}. \tag{3.10}$$

By Looking for oscillating solutions of the form $\mathbf{q}(t) = \mathbf{x}e^{i\omega t}$, the equation of motion can be reduced to the following eigenvalues problem:

$$\mathcal{K}\mathbf{x} = \omega^2 \mathcal{M}\mathbf{x}. \tag{3.11}$$

Finding the eigenvalues then provides the natural frequencies of the structure in absence of damping and the eigenvectors describe the different mode shapes. In the present case, only the modes up to 50 Hz are considered since it was the limit during the ground vibration testing campaign.

3.2 Full finite element model of the Sonaca 200

3.2.1 Mass distribution

Mass of the flexible components Using the computed sectional parameters to generate beam elements in the finite element software is equivalent to extruding the different profiles, which generates an under-evaluated mass distribution. To take into account additional mass in the real aircraft components, it is assumed that they have a trapezoidal m' mass distribution along their x coordinate. The slope and intercept of the related functions are assessed with use of the value for the total mass and the position of the center of gravity. This information is provided in the CAD files and the weight sheet of the aircraft. For a trapezoidal distribution, abscissa x_{CG} of the centroid is actually given by

$$x_{\mathrm{CG}} = \frac{b-a}{3}\frac{m'(a)+2m'(b)}{m'(a)+m'(b)}, \tag{3.12}$$

where $x = a$ and $x = b$, $a < b$, are the boundaries of the component in the axial direction. In the same time, the analytical expression for the area of a trapeze ensures that

$$m'(a) = \frac{2m}{b-a} - m'(b), \tag{3.13}$$

where m is the total mass of the considered part. It then comes that

$$m'(a) = \frac{2m}{b-a}\left[2 - \frac{3x_{\mathrm{CG}}}{b-a}\right], \tag{3.14}$$

and

$$m'(b) = \frac{2m}{b-a}\left[\frac{3x_{\mathrm{CG}}}{b-a} - 1\right]. \tag{3.15}$$

The mass functions can thus be integrated between the different sections to provide lumped masses that are added in the finite element model.

Rigid masses Components of the airplane that are not modelled with beam elements are added as concentrated masses connected to the structure with rigid link elements. They are separated in seven groups:

- seats: 15.00 kg;
- instrument panels: 15,00 kg;
- firewall forward, cabin and electrical (FF): 222,65 kg;
- main landing gear: 52,09 kg;
- front landing gear: 8.33 kg;

- remaining mass: 10,87 kg;
- lest in the left seat: 75,00 kg.

The remaining mass corresponds to the difference between the estimated mass of the Sonaca 200, including all the parts, fasteners and paint, and the actually weighted empty mass of 473.5 kg. The corresponding 0D elements are mostly located with help of the weight sheet that indicates some of the locations for the centers of gravity. Position of FF, which is not explicitly stated, is tweaked to respect position of the global center of mass in absence of lest. This latter is deduced from the masses measured at each of the two landing gears. Knowing that the front gear sustains a mass of 367.09 kg and the nose gear a mass of 106.50 kg, a simple momentum balance provides that the abscissa of the global center of gravity is situated 1,138 m behind the nose gear. This given, the finite element model of the airplane is expected to possess mass and inertia properties that are fairly similar to those of the real structure.

3.2.2 Assembly of the components and boundary conditions

Given complexity of the structure at the connection points, it may be abusive to use pure beam elements to link the different members of the aircraft together. Bushings with very high translation stiffness terms are here preferred to model the connections. In particular, it is easy enough to tweak their properties in order to perform some amount of reverse engineering. This approach is chosen to adapt the boundary conditions between the fuselage and the elements of the empennage to match the experimental data. It would otherwise be delicate to predict the combined influence of the different parts of the assembly whereas the stiffness values have a critical impact on the mode shapes. In each case, a first guess is made by selecting a reference cross section that is close enough to the connection point between two components. The bushing properties are then estimated by relying on the assumption of pure bending of beams. This latter actually leads to a simple expression for the angular stiffness terms K_{R_y} and K_{R_z} using the principal moments of area. Hooke's law for a cantilever beam under a bending moment M_y actually writes

$$M_y = \kappa E I_y, \tag{3.16}$$

where κ is here the beam curvature which is equal to the second derivative of the displacement field. It verifies

$$u_z(l) = \frac{\kappa}{2} l^2 \tag{3.17}$$

with the notations of Figure 3.2. In the same time, the maximum deflection can be parametrized with angle ϕ, which can be seen as the deflection angle of the bushing element:

$$u_z(l) = l \sin(\phi), \tag{3.18}$$

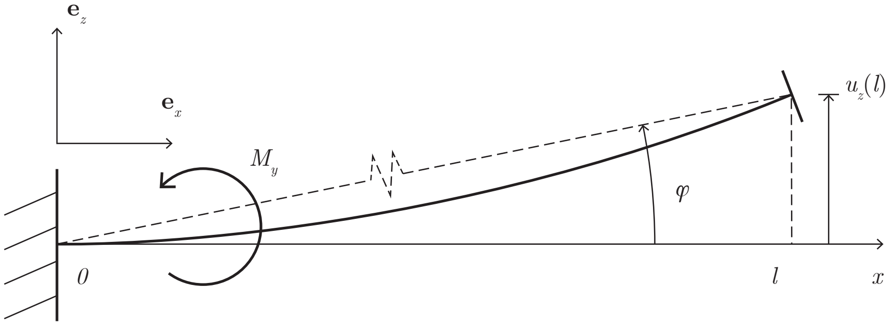

Figure 3.2: Pure bending of a cantilever beam

which means that

$$\sin(\phi) = \frac{\kappa l}{2}. \tag{3.19}$$

Using Equation 3.16 in the previous expression and linearizing $\sin(\phi)$ for a small angle then yields

$$K_{\mathrm{R}_y} = \frac{M_y}{\phi} = \frac{2EI_y}{l}. \tag{3.20}$$

In the exact same way

$$K_{\mathrm{R}_z} = \frac{2EI_z}{l}. \tag{3.21}$$

According to the ground vibration testing results [17], bending is largely predominant in the frequency range of interest for the empennage. Considering that the involved components are here the vertical and the horizontal tail plane, the torsion stiffness K_T of the bushings thus does not play a big role in modal analysis. For the sake of simplicity, it is set to

$$K_\mathrm{T} = \frac{1}{4(1+\nu)} \left(K_{\mathrm{R}_y} + K_{\mathrm{R}_z} \right), \tag{3.22}$$

which corresponds to the case where the torsion inertia I_T is approached by the sum of the two principal inertia terms under the assumption that $K_\mathrm{T} = \mu I_\mathrm{T}/l$. To match the testing conditions as much as possible, the whole structure is linked to the inertial frame using a 0D bush element with low stiffness terms. It can be noted that the value for the vertical translation stiffness K_z is fixed to respect the 1.7 Hz frequency of the suspension mentioned in the ground vibration testing report [17]. Knowing that the total weight of the system is 548.5 kg it comes that the required stiffness amounts to 62580 N/m. It is observed that values of the other terms must not be too high in order to avoid unexpected behaviour of the mode shapes. The final assembly is represented in Figure 3.3. Using the parameters discussed in this paragraph, it is possible to obtain eigenmodes that are comparable with outputs of the experimental modal analysis.

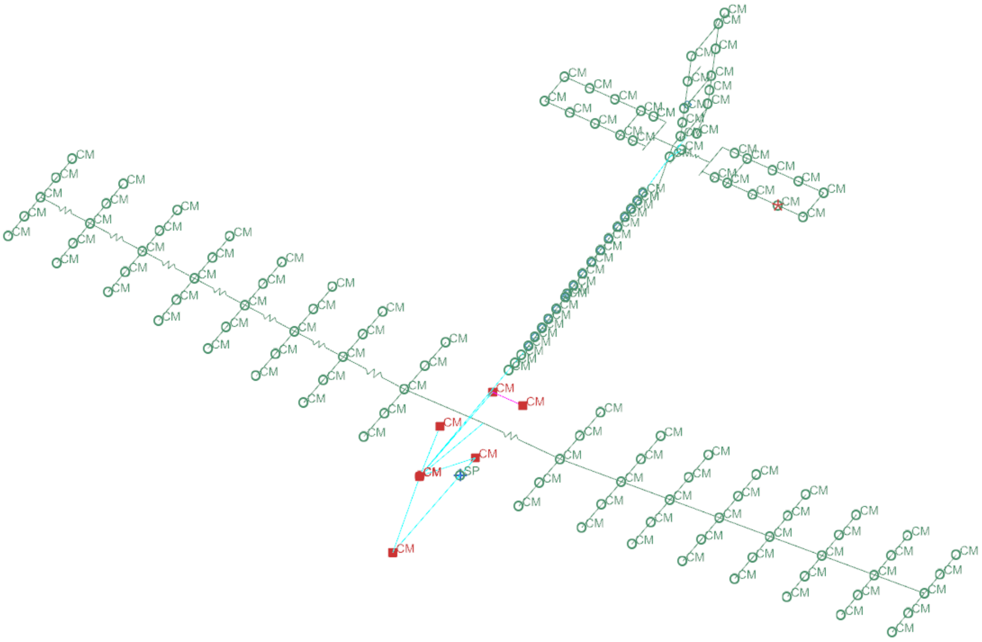

Figure 3.3: Finite element model of the full airplane; added rigid masses are represented with red squares.

3.3 Comparison of the finite element analysis results with experimental data

Eigenmodes provided by numerical modal analysis are compared to the ground vibration testing results in terms of out-of-plane displacement for the different lifting surfaces. It would be even more relevant to consider the fuselage deformation, however the corresponding experimental data were not available. This is actually the only degree of freedom that is useful in the aeroelastic analysis method implemented in this work. Numerical data for six of the fourteen identified experimental modes of the structure were provided by the *Leichtwerk* company. As an outcome, the comparison presented in this section is mainly focused on these modes, for which it is possible to compute the modal assurance criterion, commonly referenced as MAC [18]. This indicator gives a quantitative estimation of the degree of correlation between two sets of eigenvectors. It is given by

$$\mathrm{MAC} = \frac{|\mathbf{v}_{\mathrm{exp}}^{\mathrm{T}} \mathbf{v}_{\mathrm{FEM}}|^2}{\left(\mathbf{v}_{\mathrm{exp}}^{\mathrm{T}} \mathbf{v}_{\mathrm{ext}}\right) \left(\mathbf{v}_{\mathrm{FEM}}^{\mathrm{T}} \mathbf{v}_{\mathrm{FEM}}\right)}, \tag{3.23}$$

where $\mathbf{v}_{\mathrm{exp}}$ is the vector of nodal out-of-pane displacements for the experimental data and $\mathbf{v}_{\mathrm{FEM}}$ is the vector of nodal displacements for the finite element model outputs. A required precaution to use the formula of Equation 3.23, is that nodal values must be extracted at

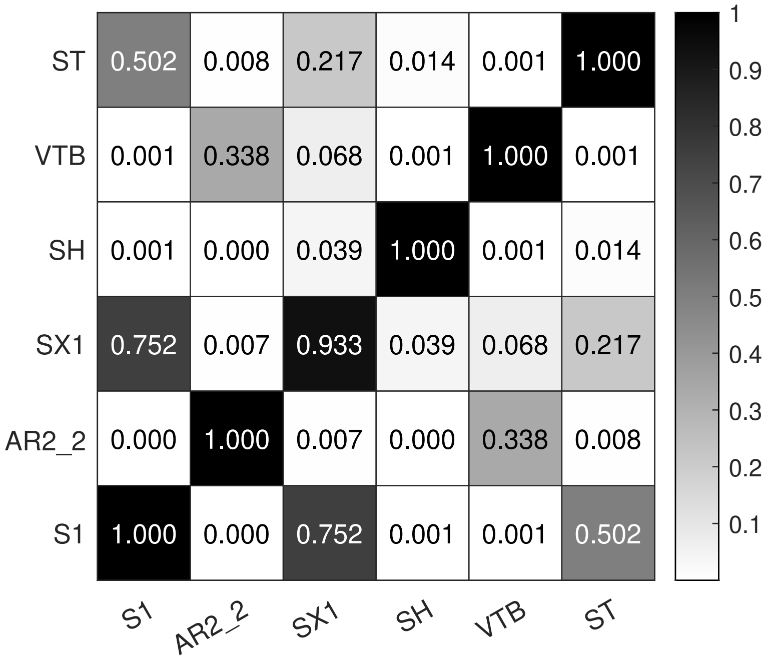

	S1	AR2_2	SX1	SH	VTB	ST
ST	0.502	0.008	0.217	0.014	0.001	1.000
VTB	0.001	0.338	0.068	0.001	1.000	0.001
SH	0.001	0.000	0.039	1.000	0.001	0.014
SX1	0.752	0.007	0.933	0.039	0.068	0.217
AR2_2	0.000	1.000	0.007	0.000	0.338	0.008
S1	1.000	0.000	0.752	0.001	0.001	0.502

Figure 3.4: Graphical representation of the auto-correlation matrix computed for the experimental modes.

the exact same locations. To do so, the finite element modes are interpolated at the nodes of the experimental mode shapes using spline functions. The method discussed here can although return spurious results if the number of degrees of freedom being compared is too low. In that case, a mode from the first family can appear to correlate equally with several modes of the second family. Therefore, it is useful to check that the number of considered degrees of freedom is high enough. One way is to compute the MAC of the experimental results with themselves, which is called the Auto-MAC. Coefficients must be very close to one for a same mode and very low for two different modes. As illustrated in Figure 3.4, the graphical representation of the auto-correlation matrix is diagonal, with diagonal coefficients being close to 1. It proves that the number of degrees of freedom is high enough. As stated above, the results presented hereafter are the consequence of an iterative process for adjusting the stiffness terms at the internal and external boundaries of the model. The selected configuration is the one that exhibits the best overall frequency and mode shapes matching between the numerical and experimental modes. This is not to negate the fact that better correlations may be found by spending more time on fine-tuning the different parameters. It can also be noted that testing conditions are not explicitly known which make it difficult to have truly realistic boundary conditions between the ground and the structure.

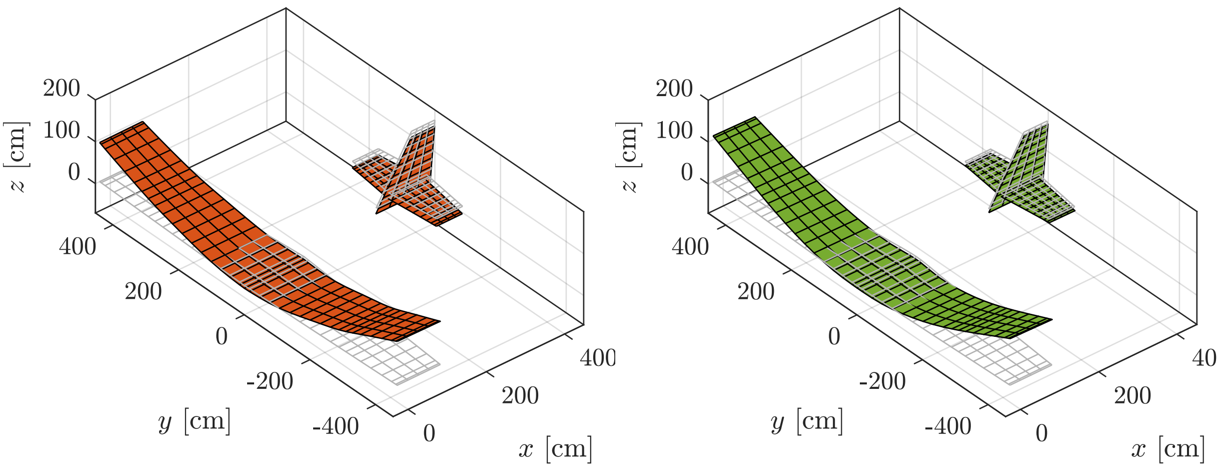

(a) Experimental mode (10.431 Hz).

(b) FE mode (7.963 Hz).

Figure 3.5: Graphical representation of mode S1 in terms out-of-plane displacements

3.3.1 First bending mode of the wing (S1)

First computed vibration mode of the system corresponds to bending of the wing at 7.963 Hz. In comparison, ground vibration testing suggests a first frequency at 10,431 Hz. Participation of other components of the airplane is negligible in the mode shape. Therefore, this mainly illustrates behavior of the base finite element model created for the wing by itself. It remains that deformation of the wing is very similar to the experimental mode shape. This can be confirmed with the actual correlation between the real and the simulated mode which amounts to 0.9883. As expected, the computed generalized mass of 20.341 kg$\times$cm^2 is also rather similar to the 22.690 kg$\times$cm^2 given by experimental data. The 23.7 % error in terms of eigenfrequency may come from approximations regarding the mass distribution or non-linearities in the real system. Connection stiffness terms at the root should not a priori be adapted in this case since they were explicitly evaluated with the full finite element model of the Sonaca 200.

3.3.2 Fuselage two-nodes bending (AR2_2)

The mode corresponding to a 2-nodes bending of the fuselage cannot clearly be identified among the outputs of the numerical modal analysis. It is characterized in the experimental data by a rotation of the empennage as a rigid body around the X-axis, and by a relatively low frequency compared to the other modes under consideration. The numerical mode presented in Figure 3.6 may share these attributes but it is obviously combined with anti-symmetrical bending of the wing which is absent from the reference material. It was observed that amplitude of the wing bending largely depends on the boundary conditions, both internal and external, and was very delicate to control. The compromise chosen in the present case does not allow to generate a mode shape for AR2_2 that is satisfactorily

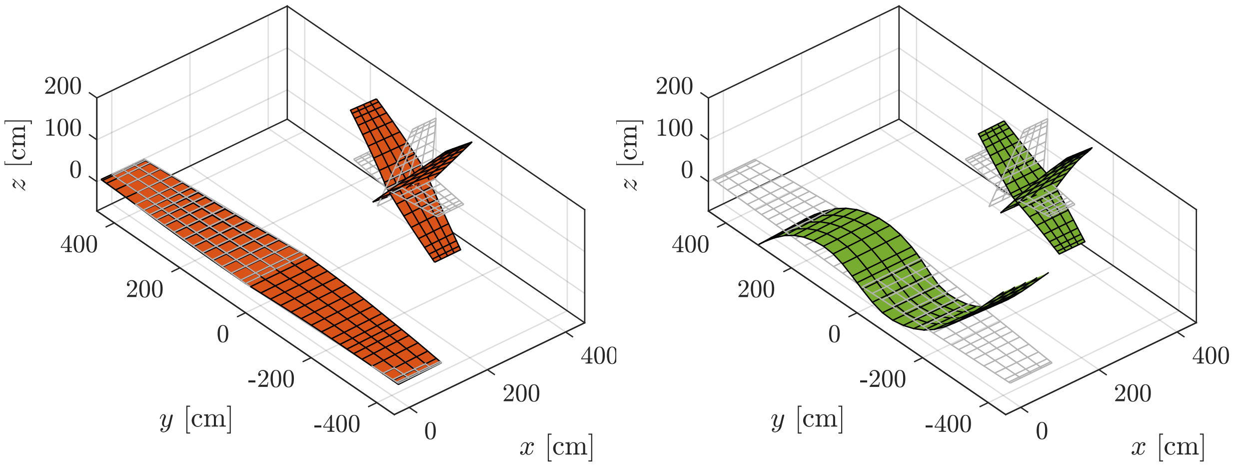

(a) Experimental mode (21.123 Hz) (b) FE mode (12.222 Hz)

Figure 3.6: Graphical representation of mode AR2_2 in terms of out-of-plane displacments

close to the experimental results. Focusing on quality of the other modes was actually preferred.

3.3.3 Wing in-plane bending (SX1)

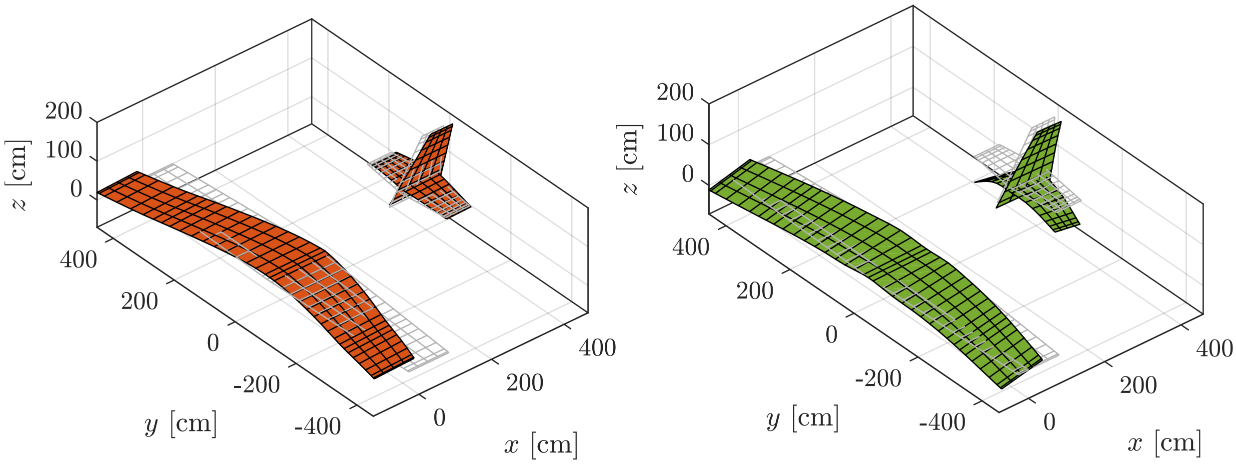

(a) Experimental mode (31.704 Hz) (b) FE mode (31.465 Hz)

Figure 3.7: Graphical representation of mode SX1 with in-plane and out-of-plane displacements.

The third mode that can be compared with experimental data describes in-plane bending of the wing at 31.465 Hz, which is very close to the 31.704 Hz of the testing results. As illustrated in Figure 3.8, in-plane bending is also coupled with slight bending of the horizontal tail plane, almost negligible for the the experimental mode shape but rather visible in the numerical results. Only normal displacements are exploited to study aeroelastic behavior of the structure. Nonetheless, deformation along the X axis is represented in Figure 3.8 since it offers a better comparison between the two cases. In this regard, the two modes have a very strong correlation of 0.933 if only in-plane displacements are taken into account. Differences in terms of generalized mass, with 12.437 kg×cm^2 against 26.020 kg×cm^2 can be explained with the phase difference regarding plunging of the wing between the two modes: the wing and horizontal tail plane vibrations are actually phase shifted in the testing data whereas it is not the case with the finite element model. It may still result from approximated mass properties of the wing in the finite element model, non-linearities in the real structure or even inaccuracies in the horizontal tail plane parameters.

3.3.4 Horizontal tail plane bending (SH)

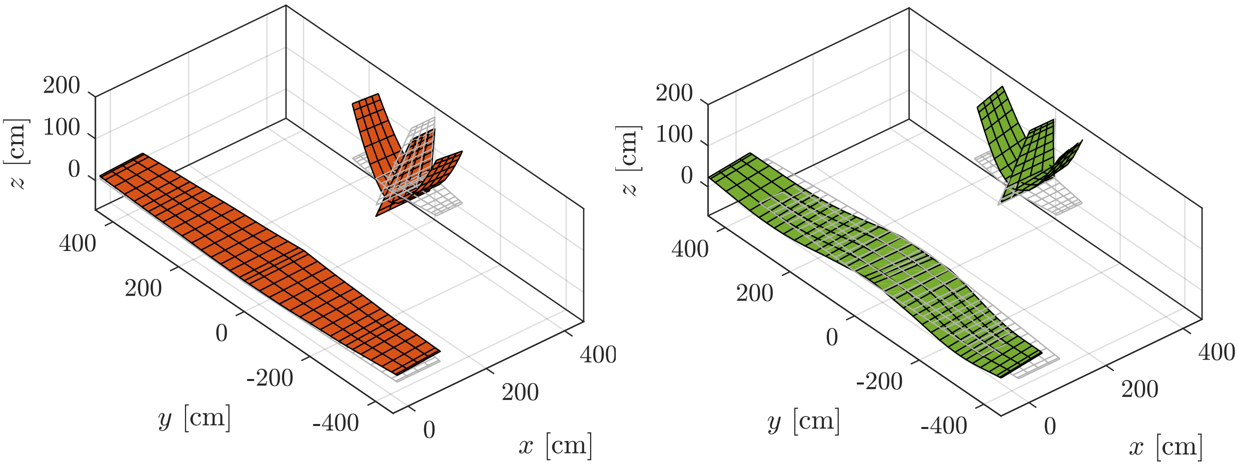

(a) Experimental mode (35.373 Hz).

(b) FE mode (36.201 Hz).

Figure 3.8: Graphical representation of mode SH in terms of out-of-plane displacements.

Bending of the horizontal tail plane is the fourth mode that can be compared with the experimental results. Vibration frequency of the simulated mode is quite similar to the actual frequency, with respectively 36.201 Hz and 35.373 Hz, which accounts for a 2.3% error. It also appears that SH is one of the modes that actually displays a good correlation between the two sets of data. This latter amounts to 0.8504, which can be confirmed by the graphical representations of Figure 3.8. In both cases, deformation of the horizontal tail plane is clearly predominant with very few contribution of the main wing. Like for the first mode, this resemblance translates in terms of generalized mass with respectively 5.621 kg×cm^2 and 4.895 kg×cm^2 for the simulated and experimental mode.

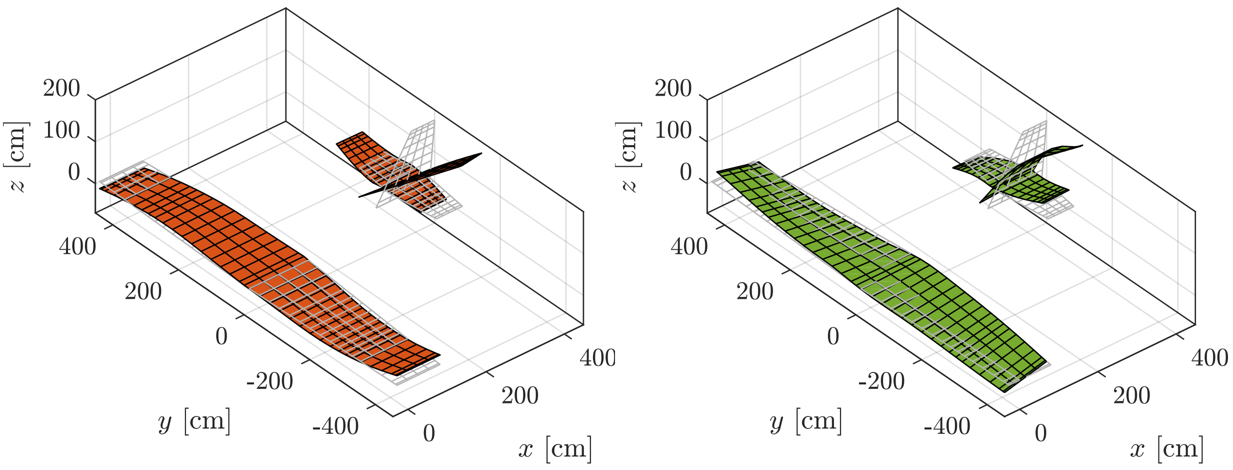

(a) Experimental mode (37.148 Hz) (b) FE mode (39.926 Hz).

Figure 3.9: Graphical representation of mode VTB in terms of out-of-plane bending.

3.3.5 Vertical tail plane bending (VTB)

With the created finite element model, the mode corresponding to bending of the vertical tail plane appears at 39.926 Hz which only represents a difference of 7.5 % with the experimental results that suggest an eigenfrequency of 37.148 Hz. According to Figure 3.9 it can be observed that deformation is predominant on VTP in both cases in spite that the mode shapes apparently differ from each other. The fact that the surface remains almost planar in the experimental mode shape can be put in parallel with the measurement setup for this part of the structure. Indeed, it appears in the ground vibration testing report [17] that the normal deflection on VTP is only extracted at four points roughly situated at the four corners of the surface. It thus limits the amount of details that can be represented, hence the simplified appearance of the mode shape. Nonetheless, the small contribution of the horizontal tail plane and wing, that have similar amplitudes in both cases, are phase shifted in the numerical analysis outputs. It is however delicate to correct this issue easily. The present choice of parameters for connection stiffness terms remains a good compromise between similarity of the mode shapes concerning VTB and frequency matching for all the other modes.

3.3.6 Second wing bending (S2)

The mode corresponding to second wing bending clearly appears in the finite element analysis at 40.672 Hz. It is very close to the experimental frequency of 40.160 Hz. Moreover the two mode shapes are quite similar, as it can be seen in Figure 3.11. In both cases deformation of the tail does appear in synchronization with the wing. Unfortunately, only a graphical representation of the deformation is available for the experimental eigenvector. As an outcome, it is not possible to numerically evaluate the correlation between the two

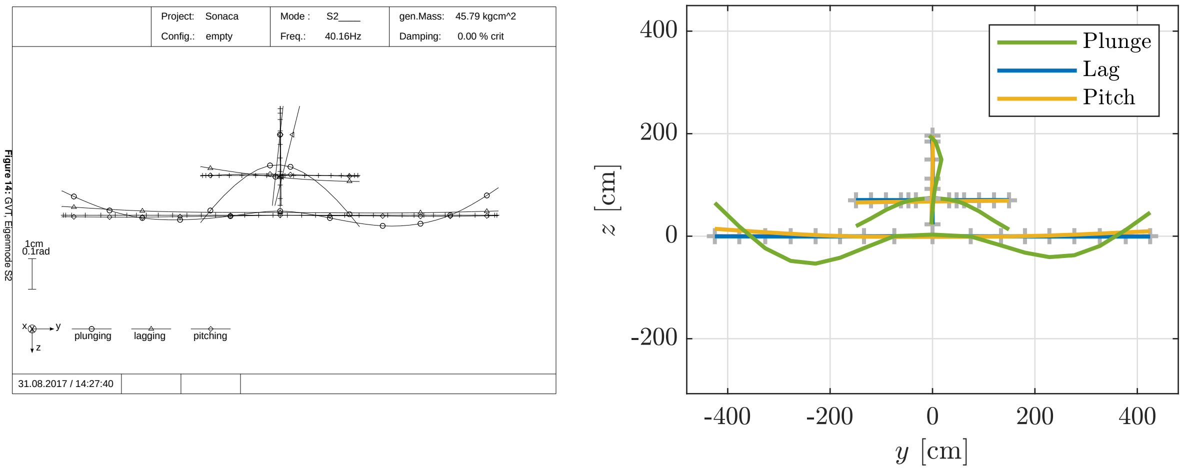

(a) Experimental mode [17] (40.160 Hz). (b) FE mode (40.672 Hz).

Figure 3.10: Graphical representation of mode S2.

cases, which could be expected to be rather close to 1. For the same reason, it hinders from exploiting the experimental results of this mode with the developped aeroelastic solver later introduced in this report .

3.3.7 Wing torsion (ST)

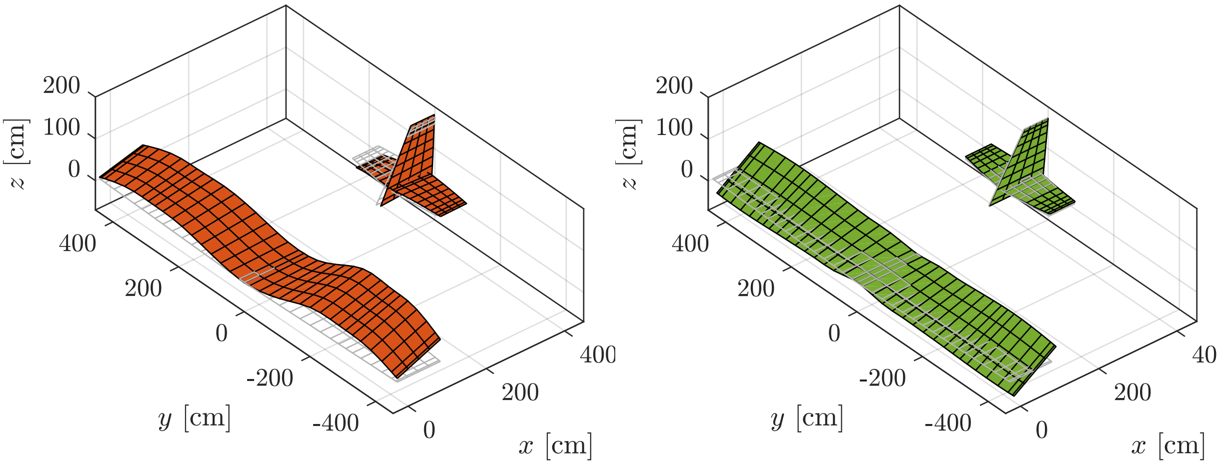

(a) Experimental mode (49.471 Hz). (b) FE mode (45.450 Hz).

Figure 3.11: Graphical representation of mode S2.

Symmetrical wing torsion appears at 45.450 Hz using the finite element model. It is fairly close, with a 8.3 % error, to the so-called torsion mode extracted from GVT data. While ST is explicitly described by *Leichtwerk* as torsion of the main wing, it is obviously coupled with a form of 2-node bending which is not present with numerical modal analysis.

Surprisingly, generalized masses remain close enough but this can not be interpreted with a strong similarity between the two modes.

3.4 Conclusions

Modes	Experimental data		FEM		MAC
	f [Hz]	μ [kg×cm^2]	f [Hz]	μ [kg×cm^2]	
S1 (*Err* [%])	10.431 -	22.690 -	7.963 (23.7)	20.341 (10.6)	0.988
AR2_2 (*Err* [%])	21.123 -	10.435 -	12.222 (42.1)	34.780 (233.3)	<0.5
SX1 (*Err* [%])	31.704 -	26.020 -	31.465 (0.8)	12.437 (52.2)	0.943
SH (*Err* [%])	35.373 -	4.895 -	36.201 (2.3)	5.621 (14.8)	0.850
VTB (*Err* [%])	37.148 -	4.600 -	39.926 (7.5)	2.062 (55.2)	0.679
S2 (*Err* [%])	40.160 -	45.79 -	40.672 (1.3)	20.302 (55.7)	-
ST (*Err* [%])	49.471 -	16.940 -	45.450 (8.3)	15.705 (7.3)	<0.5

Table 5: Synthesis of the modal parameters for the different compared modes.

Results presented above are synthesized in Table 5. At the exception of AR2_2, all the simulated modes present a certain level of similarity with their experimental counterpart, in regard of the eigenfrequencies and/or generalized masses as well as visually and in terms of correlation factor for some of them. Four additional vibration modes presented in Annex B were also given by numerical modal analysis but could not be paired with the ones described by *Leichtwerk*. It does not necessarily mean that they are unphysical: part of the lack of correlation between the results comes from undetermination in the boundary conditions with the ground. In other words they might correpsond to vibration modes that can be encountered in real life but not in the conditions of the ground vibration testing. Nonetheless, the final objective remains computation of aeroelastic solutions. This step only can validate wether or not the finite element model outputs can compare with an experimental approach in the present context. Aside from this, it can be noted that some improvement to the model could be beneficial in further studies. It could actually be relevant to consider the engine mount as a flexible structure whereas it is treated here as a rigid body. Mobility of the control surfaces can also be tackled. It can be stated that the followed methodology may provide a good basis to articulate the mobile parts with respect to the main frame as their mechanical properties are separately evaluated. In absolute terms it would mean changing the rigid links between HTP and ELV, VTP and RD into hinge elements.

4 Aeroelastic modelling

4.1 Principles of flutter analysis using the frequency-domain Vortex Lattice Method with multiple lifting surfaces

The goal of the Vortex Lattice Method (VLM) is to simulate unsteady phenomena taking place between the aircraft structure and the wake it generates. As described by Katz and Plotkin [2], this approach lies in the framework of incompressible potential flow theory. It is thus adapted for the study of subsonic flight in attached flow conditions. Two notorious benefits of this method are the ability to describe 3D effects like the roll-up of the wake and to consider large motions of the lifting surfaces. But it is also convenient to contemplate vibrational phenomena, which makes of it a good tool for flutter analysis, as described in this section. The studied implementation relies on the formulation of Dimitriadis [3] which elaborates the modal frequency-domain use of the VLM in order to simplify the aeroelastic stability analysis. It is question here of its generalization to N lifting surfaces in order to obtain solutions from practical aeroelastic systems.

4.1.1 Definition of the general aeroelastic model

The theoretical system under consideration consists in a simplified aircraft structure composed of N flexible lifting surfaces arranged in space in presence of an air flow of free stream velocity Q_∞. In the most general case, such lifting surfaces could be used to describe fuselage panels but the analysis carried out hereafter assumes a classical definition of the lifting surfaces: wing, canard, tail, fins. As mentioned above, the assumption of potential flow is made, which implies that thickness of the aerodynamic profiles is neglected. In each lifting surface, the motion of a given point is described by a single out-of-plane translation v. Its direction is chosen to be consistent with the general orientation of the surface, e.g. $\mathbf{e}_Z$ for a wing, $\mathbf{e}_Y$ for a vertical fin. It is then possible to consider a modal expansion on n_m structural modes of the form:

$$v(x,y,z,t) = \sum_{i=1}^{n_\mathrm{m}} w_i(x,y,z) r_i(t), \tag{4.1}$$

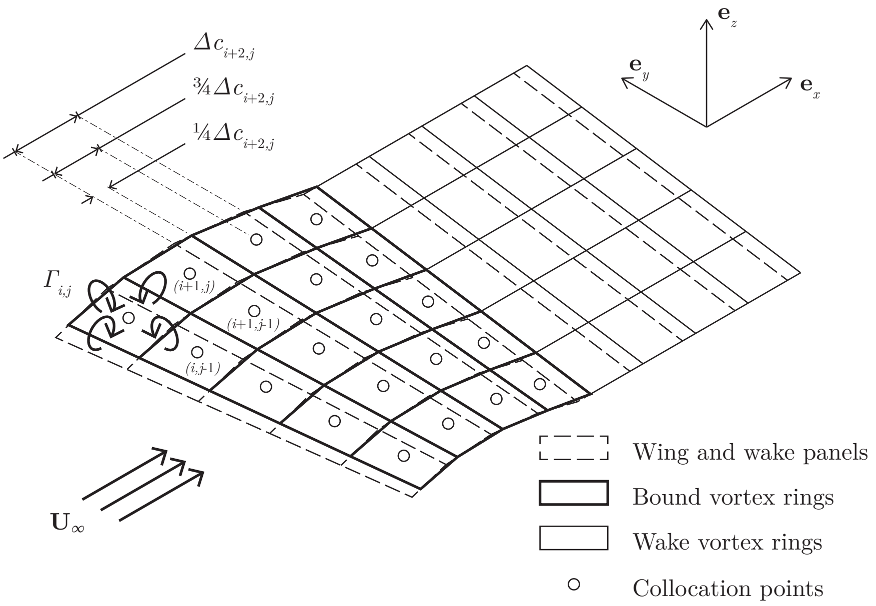

Figure 4.1: Aeroelastic model of a wing as used in the Vortex Lattice Method.

where $w_i(x, y, z)$ is the i^{th} modeshape function and $r_i(t)$ is the i^{th} generalized coordinate. Besides, dynamics of the system can be described as an equilibrium between internal forces in the structure and generalized aerodynamic forces using Lagrange's formalism:

$$\forall i \in \{1, ..., n_m\} \quad \frac{\mathrm{d}}{\mathrm{d}t}\left(\frac{\partial(\mathcal{T} - \mathcal{V})}{\partial \dot{r}_i}\right) - \frac{\partial(\mathcal{T} - \mathcal{V})}{\partial r_i} = Q_i, \tag{4.2}$$

where $\mathcal{T} - \mathcal{V} = E$ is the total energy of the system, $\mathcal{T}$ is the kinetic energy, $\mathcal{V}$ is the potential energy and $Q_i(t)$ is the generalized force acting on mode i. It can be expressed in terms of pressure difference on the whole set of lifting surfaces:

$$Q_i(t) = \int_{S_1 \cup \ldots \cup S_N} \Delta p(x, y, z, t) \frac{\partial v}{\partial r_i} \mathrm{d}S. \tag{4.3}$$

In order to compute the unsteady pressure field on member k, $k \in \{1, ..., N\}$, which is considered to be a wing for convenience reasons, impermeability and Kutta conditions need to be applied. To do so, the wing planform is discretized in m_k chordwise and n_k spanwise panels which are defined on the mean camber surface as seen in Figure 4.1. This base mesh allows to build vortex rings, the leading edges of which coincide with the quarter-chord lines of the underlying panels. Panels and vortex rings are also added in the wake, with the leading edge of the first ring corresponding to the trailing edge of the last wing vortex ring.

4.1.2 Impermeability condition for the full airplane

Vortices are commonly used singularities in potential flow theory. They are solutions of Laplace's equation:

$$\Delta\phi = \mathbf{0}, \tag{4.4}$$

where ϕ is the scalar potential from which the velocity field is derivated and Δ is the laplacian operator. In order to verify the impermeability condition on a given lifting surface, the potential must verify the following boundary condition at any point:

$$\nabla\phi \cdot \mathbf{n} = \nabla(\phi_{\mathrm{s}} + \phi_{\infty}) \cdot \mathbf{n} = \mathbf{0}, \tag{4.5}$$

where ϕ_{s} is the auto induced part of the potential and ϕ_{∞} is the contribution of the free stream. This latter is known at each time but ϕ_{s} has to be evaluated using vortex ring elements. Influence of a vortex line segment of constant strength Γ between point 1 and point 2 on an arbitrary point P is given by Biot-Savart's law [2]:

$$\mathbf{q}_{1.2} = -\frac{\Gamma}{4\pi}\frac{\mathbf{r}_1 \times \mathbf{r}_2}{|\mathbf{r}_1 \times \mathbf{r}_2|^2}\mathbf{r}_0 \cdot \left(\frac{\mathbf{r}_1}{r_1} - \frac{\mathbf{r}_2}{r_2}\right), \tag{4.6}$$

where $\mathbf{q}_{1,2}$ is the induced velocity and where the geometrical vectors are defined in Figure 4.2. According to the superposition principle, the velocity induced by a vortex ring is the sum of the velocities induced by the four segments forming its contour. They are computed here at collocation points situated on the center line of the wing panels at three-quarters of the chord. For a given collocation point in position (i, j), the influence of vortex (i', j') writes

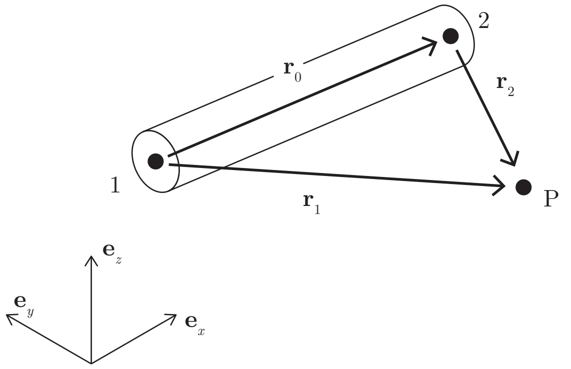

Figure 4.2: Nomenclature used for vortex line segment theory.

$$(u, v, w)_{ij,i'j'} \cdot \mathbf{n}_{ij} = a_{ij,i'j'}\Gamma_{i'j'}, \tag{4.7}$$

where $a_{ij,i'j'}$ is the velocity induced by a unit strength singularity in (i',j'), $\Gamma_{i'j'}$ is the strength of the vortex situated in (i',j'), and $\mathbf{n}_{ij}$ is the normal vector to wing panel (i,j). From a structural point of view, geometry of wing k and its wake are frozen throughout the time history and the relative air flow due to structural displacements and the free stream velocity $\mathbf{U}_\infty = (U \ V \ W)^\mathrm{T}$ is represented with downwash terms. The impermeability condition is imposed at each collocation point where the induced velocities are computed. It leads to a matrix equation involving the downwash terms associated to wing k, as well as the vortex strength distributions of all the other lifting surfaces:

$$Q_\infty \mathrm{diag}\left(\hat{\mathbf{U}}_k \mathbf{n}_k^\mathrm{T}\right) - \left(U\frac{\partial \mathbf{v}_k}{\partial x} - \frac{\partial \mathbf{v}_k}{\partial t}\right) + \sum_{l=1}^{N} \tilde{\mathbf{A}}_{l,k}^\mathrm{b} \mathbf{\Gamma}_l^\mathrm{b} + \sum_{l=1}^{N} \tilde{\mathbf{A}}_{l,k}^\mathrm{w} \mathbf{\Gamma}_l^\mathrm{w} = \mathbf{0}, \tag{4.8}$$

where, $\hat{\mathbf{U}}_k$ is the $m_k n_k \times 3$ matrix whose rows are all equal to $\mathbf{U}_\infty / Q_\infty$, $\mathbf{n}_k$ is the $m_k n_k \times 3$ matrix of unit vectors normal to the wing panels, $\mathbf{v}_k$ is the $m_k n_k \times 1$ vector of normal displacements, $\tilde{\mathbf{A}}_{l,k}^\mathrm{b}$ is the $m_l n_l \times m_k n_k$ influence coefficients matrix of the bound vortices of surface l on the collocation points of surface k, $\tilde{\mathbf{A}}_{l,k}^\mathrm{w}$ is the $m_l^\mathrm{w} n_l \times m_k^\mathrm{w} n_k$ influence coefficients matrix of the wake vortices of surface l on the collocation points of surface k. Finally, $\mathbf{\Gamma}_l^\mathrm{b}$ is the $m_l n_l \times 1$ vector of the strengths of the bound vortex rings of surface l and $\mathbf{\Gamma}_l^\mathrm{w}$ is the corresponding $m_l n_l \times 1$ vector of the strengths of the wake vortex rings. Using the matrix notation $\mathbf{v}_k = \mathbf{W}_k \mathbf{r}(t)$, where $\mathbf{W}_k$ is the $m_k n_k \times n_\mathrm{m}$ matrix of the eigenvectors introduced in Equation 4.1, Equation 4.8 can also be written:

$$Q_\infty \mathrm{diag}\left(\hat{\mathbf{U}}_k \mathbf{n}_k^\mathrm{T}\right) - U\partial_x \mathbf{W}_k \mathbf{r}(t) - \mathbf{W}_k \dot{\mathbf{r}}(t) + \sum_{l=1}^{N} \tilde{\mathbf{A}}_{l,k}^\mathrm{b} \mathbf{\Gamma}_l^\mathrm{b} + \sum_{l=1}^{N} \tilde{\mathbf{A}}_{l,k}^\mathrm{w} \mathbf{\Gamma}_l^\mathrm{w} = \mathbf{0}. \tag{4.9}$$

4.1.3 Unsteady Kutta condition

The trailing row of bound vortices is propagated in the wake which ensures that the 2D Kutta condition is respected on each panel of the wing over time. After leaving the lifting surface, the vorticity is shed on the subsequent vortex rings at a constant strength after a time step Δt. It means that the i^th chordwise row of wake vortices at time t has the same strength as the trailing row of bound vortices at time $t - i\Delta t$. This explicit time-marching implementation of the Kutta condition implies that $\left(\mathbf{\Gamma}_l^\mathrm{b}\right)_{l=1,..,N}$ is the only set of unknowns in Equation 4.9. It remains that $\sum_{l=1, l\neq k}^{N} m_l n_l$ other equations are necessary to solve the problem for surface k. They can be found by writing the impermeability conditions for all the other surfaces. It leads to a system of $N_\mathrm{e} = \sum_{l=1}^{N} m_l n_l$ independent equations with N_e unknowns that can be expressed in the following matrix form:

$$Q_\infty \mathrm{diag}\left(\hat{\mathbf{U}} \mathbf{n}^\mathrm{T}\right) - U\partial_x \mathbf{W} \mathbf{r}(t) - \mathbf{W} \dot{\mathbf{r}}(t) + \mathbf{A}^\mathrm{b} \mathbf{\Gamma}^\mathrm{b} + \mathbf{A}^\mathrm{w} \mathbf{\Gamma}^\mathrm{w} = 0, \tag{4.10}$$

where $\hat{\mathbf{U}}$ is the $N_{\mathrm{e}} \times 3$ matrix of free stream velocities, $\mathbf{n}$ is the $N_{\mathrm{e}} \times 3$ matrix of normal vectors, and $\mathbf{W}$ is the $N_{\mathrm{e}} \times n_{\mathrm{m}}$ matrix of eigenvectors. These matrices are obtained by vertically concatenating the matrices introduced in the individual impermeability conditions, like in Equation 4.9. Similarly, $\boldsymbol{\Gamma}^{\mathrm{b}}$ and $\boldsymbol{\Gamma}^{\mathrm{w}}$ are the $N_{\mathrm{e}} \times 1$ and $\sum_{l=1}^{N} m_l^{\mathrm{w}} n_l \times 1$ vectors of vortex strength defined as:

$$\boldsymbol{\Gamma}^{\mathrm{b}} = \begin{bmatrix} \boldsymbol{\Gamma}_1^{\mathrm{b}} \\ \vdots \\ \boldsymbol{\Gamma}_N^{\mathrm{b}} \end{bmatrix}, \text{ and } \boldsymbol{\Gamma}^{\mathrm{w}} = \begin{bmatrix} \boldsymbol{\Gamma}_1^{\mathrm{w}} \\ \vdots \\ \boldsymbol{\Gamma}_N^{\mathrm{w}} \end{bmatrix}. \tag{4.11}$$

As to the influence coefficients, $\mathbf{A}^{\mathrm{b}}$ is the $N_{\mathrm{e}} \times N_{\mathrm{e}}$ influence coefficients matrix of the bound vorticity, defined by block as:

$$\mathbf{A}^{\mathrm{b}} = \begin{bmatrix} \tilde{\mathbf{A}}_{1,1}^{\mathrm{b}} & \dots & \tilde{\mathbf{A}}_{N,1}^{\mathrm{b}} \\ \vdots & \ddots & \vdots \\ \tilde{\mathbf{A}}_{1,N}^{\mathrm{b}} & \dots & \tilde{\mathbf{A}}_{N,N}^{\mathrm{b}} \end{bmatrix}, \tag{4.12}$$

and $\mathbf{A}^{\mathrm{w}}$ is the $N_{\mathrm{e}} \times \sum_{l=1}^{N} m_l^{\mathrm{w}} n_l$ influence matrix of wake vorticity, defined by blocks as:

$$\mathbf{A}^{\mathrm{w}} = \begin{bmatrix} \tilde{\mathbf{A}}_{1,1}^{\mathrm{w}} & \dots & \tilde{\mathbf{A}}_{N,1}^{\mathrm{w}} \\ \vdots & \ddots & \vdots \\ \tilde{\mathbf{A}}_{1,N}^{\mathrm{w}} & \dots & \tilde{\mathbf{A}}_{N,N}^{\mathrm{w}} \end{bmatrix}. \tag{4.13}$$

As mentionned earlier, the wake vorticity shed by surface k is directly related to its bound vorticity with the relation

$$\boldsymbol{\Gamma}_k^{\mathrm{w}}(t) = \left[\begin{array}{c} \Gamma_{m_k,1}^{\mathrm{b}}(t-\Delta t) \\ \vdots \\ \Gamma_{m_k,n_k}^{\mathrm{b}}(t-\Delta t) \\ \hline \vdots \\ \hline \Gamma_{m_k,1}^{\mathrm{b}}(t-m_k^{\mathrm{w}}\Delta t) \\ \vdots \\ \Gamma_{m_k,n_k}^{\mathrm{b}}(t-m_k^{\mathrm{w}}\Delta t) \end{array}\right] = \begin{bmatrix} \mathbf{P}_k^{\mathrm{c}}\boldsymbol{\Gamma}_k^{\mathrm{b}}(t-\Delta t) \\ \vdots \\ \mathbf{P}_k^{\mathrm{c}}\boldsymbol{\Gamma}_k^{\mathrm{b}}(t-m_k^{\mathrm{w}}\Delta t) \end{bmatrix}, \tag{4.14}$$

where $\mathbf{P}_k^{\mathrm{c}}$ is the $n_k \times m_k n_k$ matrix $\mathbf{P}_k^{\mathrm{c}} = \left[\mathbf{O}_{n_k\times(m_k-1)n_k}\ \mathbf{I}_{n_k}\right]$. In order to have a more convenient expression of the wake vorticity that does not contain values of the bound vorticity, it is possible to consider the Fourrier transform of Equation 4.9:

$$Q_\infty \mathrm{diag}\left(\hat{\mathbf{U}}\mathbf{n}^{\mathrm{T}}\right)\delta(\omega) - U\partial_x\mathbf{W}\mathbf{r}(\omega) - i\omega\mathbf{W}\mathbf{r}(\omega) + \mathbf{A}^{\mathrm{b}}\boldsymbol{\Gamma}^{\mathrm{b}}(\omega) + \mathbf{A}^{\mathrm{w}}\boldsymbol{\Gamma}^{\mathrm{w}}(\omega) = \mathbf{0}. \tag{4.15}$$

As the Fourrier transform of $f(t-\Delta t)$ is $e^{-i\omega\Delta t}F(\omega)$, the frequency domain expression of $\mathbf{\Gamma}_k^{\mathrm{w}}$ becomes

$$\mathbf{\Gamma}_k^{\mathrm{w}}(\omega) = \begin{bmatrix} \mathbf{P}_k^{\mathrm{c}}\mathbf{\Gamma}_k^{\mathrm{b}}(\omega)e^{-i\omega\Delta t} \\ \vdots \\ \mathbf{P}_k^{\mathrm{c}}\mathbf{\Gamma}_k^{\mathrm{b}}(\omega)e^{-m_k^{\mathrm{w}}i\omega\Delta t} \end{bmatrix} = \mathbf{P}_k^{\mathrm{c}} \begin{bmatrix} \mathbf{\Gamma}_k^{\mathrm{b}}(\omega)e^{-i\omega\Delta t} \\ \vdots \\ \mathbf{\Gamma}_k^{\mathrm{b}}(\omega)e^{-m_k^{\mathrm{w}}i\omega\Delta t} \end{bmatrix} = \mathbf{P}_k^{\mathrm{e}}(\omega)\mathbf{P}_k^{\mathrm{c}}\mathbf{\Gamma}_k^{\mathrm{b}}(\omega), \tag{4.16}$$

with $\mathbf{P}_k^{\mathrm{e}}$ the $n_k m_k^{\mathrm{w}} \times n_k$ matrix given by

$$\mathbf{P}_k^{\mathrm{e}} = \begin{bmatrix} \mathbf{I}_{n_k}e^{-i\omega\Delta t} \\ \vdots \\ \mathbf{I}_{n_k}e^{-m_k^{\mathrm{w}}i\omega\Delta t} \end{bmatrix}. \tag{4.17}$$

The decomposition displayed in Equation 4.16 applies to the whole set of lifting surfaces, which can be summarized in the compact form

$$\mathbf{\Gamma}^{\mathrm{w}}(\omega) = \mathbf{P}^{\mathrm{e}}(\omega)\mathbf{P}^{\mathrm{c}}\mathbf{\Gamma}^{\mathrm{b}}(\omega), \tag{4.18}$$

where $\mathbf{P}^{\mathrm{e}}(\omega)$ and $\mathbf{P}^{\mathrm{c}}$ are respectively the $\sum_{l=1}^{N} n_l m_l^{\mathrm{w}} \times \sum_{l=1}^{N} n_l$ and $\sum_{l=1}^{N} n_l \times N_{\mathrm{e}}$ block diagonal matrices respectively given by

$$\mathbf{P}^{\mathrm{e}}(\omega) = \begin{bmatrix} \mathbf{P}_1^{\mathrm{e}}(\omega) & & (0) \\ & \ddots & \\ (0) & & \mathbf{P}_N^{\mathrm{e}}(\omega) \end{bmatrix}, \text{ and } \mathbf{P}^{\mathrm{c}} = \begin{bmatrix} \mathbf{P}_1^{\mathrm{c}} & & (0) \\ & \ddots & \\ (0) & & \mathbf{P}_N^{\mathrm{c}} \end{bmatrix}. \tag{4.19}$$

Substituting in Equation 4.15 and solving for $\mathbf{\Gamma}^{\mathrm{b}}(\omega)$ then provides

$$\mathbf{\Gamma}^{\mathrm{b}}(\omega) = -\left(\mathbf{A}^{\mathrm{b}} + \mathbf{A}^{\mathrm{w}}\mathbf{P}^{\mathrm{e}}(\omega)\mathbf{P}^{\mathrm{c}}\right)^{-1}\left(\mathrm{diag}\left(Q_\infty\hat{\mathbf{U}}\mathbf{n}^{\mathrm{T}}\right)\delta(\omega) - \left(U\partial_x\mathbf{W} + i\omega\mathbf{W}\right)\mathbf{r}(\omega)\right). \tag{4.20}$$

It can be noticed that Equation 4.20 has the exact same form as the expression obtained by Dimitriadis [3] for a single lifting surface.

4.1.4 Computation of the lift

Knowing the vorticity over the full aeroelastic model allows to compute the generalized lifting force as a function of the modal coordinates. This can be performed with the expression introduced by Katz and Plotkin [2] for computing the aerodynamic normal force contribution of the $(i,j)^{\mathrm{th}}$ panel of a given surface. The subsequent transformations in the frequency domain are out of the scope of this report but may be found in the references for further information. The final form of the lift is a $N_{\mathrm{e}} \times 1$ vector given as a function of the reduced frequency $\kappa = \omega b/Q_\infty$ with b the half chord of the reference lifting surface:

$$\mathbf{L}(\kappa) = -\rho Q_\infty^2 \left(\mathbf{L}_0\delta(\kappa) - \mathbf{L}_1(\kappa)\mathbf{r}(\kappa)\right), \tag{4.21}$$

where $\delta(\kappa)$ is the Dirac delta function. The two terms $\mathbf{L}_0$ and $\mathbf{L}_1(\kappa)$ respectively refer to the static and dynamic parts of the lift force. They are obtained using the previously defined influence and propagation matrices, as well as the geometric properties of the wing panels:

$$\mathbf{L}_0 = \mathbf{G}_{\text{cs}} \left(\mathbf{A}^{\text{b}} + \mathbf{A}^{\text{w}}\mathbf{P}^{\text{e}}(0)\mathbf{P}^{\text{c}}\right)^{-1} \operatorname{diag}\left(\hat{\mathbf{U}}\mathbf{n}^{\text{T}}\right), \tag{4.22}$$

and

$$\mathbf{L}_1(\kappa) = \left(\mathbf{G}_{\text{cs}} + i\frac{\kappa}{b}\mathbf{G}_{\text{A}}\right)\left(\mathbf{A}^{\text{b}} + \mathbf{A}^{\text{w}}\mathbf{P}^{\text{e}}(\kappa)\mathbf{P}^{\text{c}}\right)^{-1}\left(\partial_x\mathbf{W} + i\frac{\kappa}{b}\mathbf{W}\right), \tag{4.23}$$

where $\mathbf{G}_{\text{A}}$ is the $N_{\text{e}} \times N_{\text{e}}$ diagonal matrix, the diagonal elements of which are the wing panel areas, and $\mathbf{G}_{\text{cs}}$ is a $N_{\text{e}} \times N_{\text{e}}$ matrix involving the in-plane orientation vectors of the wing panels [1]. The current expression for the lift can then be used as the right member in the equation of motion. Nonetheless, it must be noted that Equation 4.21 is the outcome of a linearization that relies on several assumptions:

- all the surfaces have a small camber and a small dihedral angle so that the induced downwash terms are negligible, which is respected in the case of the Sonaca 200;
- induced velocities in the tangent directions remain small;
- the yaw angle of the airplane also remains small throughout time.

4.1.5 Equation of motion

The equation of motion for the considered system has the general time-domain expression

$$\mathcal{M}\ddot{\mathbf{v}}(t) + \mathcal{K}\mathbf{v}(t) = \mathbf{L}(t). \tag{4.24}$$

Applying the modal decomposition $\mathbf{v}(t) = \mathbf{W}\mathbf{r}(t)$ and multiplying by $\mathbf{W}^{\text{T}}$ to the left allows to write the modal form of Equation 4.24,

$$\mathcal{A}\ddot{\mathbf{r}}(t) + \mathcal{E}\mathbf{r}(t) = \mathbf{Q}(t), \tag{4.25}$$

where $\mathcal{A} = \mathbf{W}^{\text{T}}\mathcal{M}\mathbf{W}$ is the modal mass matrix of the system, $\mathcal{E} = \mathbf{W}^{\text{T}}\mathcal{K}\mathbf{W}$ is the modal stiffness matrix, and $\mathbf{Q}(t) = \mathbf{W}^{\text{T}}\mathbf{L}(t)$ is the generalized force vector corresponding to the definition given in Equation 4.3. Applying the Fourier transform to Equation 4.25

---

[1] $\mathbf{G}_{\text{A}}$ and $\mathbf{G}_{\text{cs}}$ are obtained from the definitions given by Dimitriadis [3] by proxy of the same block matrix formalism as for $\mathbf{P}^{\text{e}}$ and $\mathbf{P}^{\text{c}}$ in Equation 4.19

and substituting with the expression for $\mathbf{L}(\kappa)$ given by Equation 4.21 provides a new expression for the modal equation of motion,

$$\left(-\left(\frac{\kappa Q_\infty}{b}\right)^2 \mathcal{A} + \mathcal{E} - \rho Q_\infty^2 \mathbf{Q}_1(\kappa)\right) \mathbf{r}(\kappa) = -\rho Q_\infty^2 \mathbf{Q}_0 \delta(\kappa), \tag{4.26}$$

where $\mathbf{Q}_1(\kappa) = \mathbf{W}^{\mathrm{T}}\mathbf{L}_1(\kappa)$ and $\mathbf{Q}_0 = \mathbf{W}^{\mathrm{T}}\mathbf{L}_0$. On the one hand, solving for $\mathbf{r}(0)$ at $\kappa = 0$ can give the static deflection of the structure at a fixed airspeed. On the other hand, obtaining non-trivial solutions in terms of κ and Q_∞ for $\kappa > 0$ takes to cancel the flutter determinant:

$$\det\left(-\left(\frac{\kappa Q_\infty}{b}\right)^2 \mathcal{A} + \mathcal{E} - \rho Q_\infty^2 \mathbf{Q}_1(\kappa)\right) = 0. \tag{4.27}$$

In conjunction with a search procedure like Newton-Raphson algorithm, Equation 4.27 can be exploited to find an eventual flutter speed and the corresponding frequency in the flight envelope of the aircraft. Besides, the flutter determinant solution can be correlated with the outputs of the $p - \kappa$ method, also based on Equation 4.27. This particular approach is further introduced to discuss the practical solutions of the aeroelastic problem. But for this purpose, the structural model of the Sonaca 200, presented in Section 2, first needs to be integrated in the VLM code developed in *Matlab*.

4.2 Practical aeroelastic model of the S200: integration of the structural model in the VLM code

4.2.1 Preliminary considerations

The practical aeroelastic model defined in this section [2] only considers the interactions of the main lifting surfaces with the air flow and neglects the aerodynamic behavior of the fuselage. As an outcome, the finite element model of the fuselage developed in Section 2 only acts as flexible connection between the wing and the empennage and its nodal outputs are not needed in the subsequent steps. It only ensures that members of the aircraft can move as rigid bodies in relation to each other in a way that is consistent with the mechanical behavior of the real structure. Only the outputs of the finite element model given at the locations of the wing, tail and vertical fin are integrated in the Vortex Lattice Method developed in *Matlab* to simulate fluid structure interactions. The nodal displacements provided by modal analysis are actually interpolated to describe deformations of the chord surfaces. As described in the following, the extracted mode shapes are then converted into deformations of the properly discretized lifting surfaces to build the $\mathbf{W}$ and $\partial_x\mathbf{W}$ matrices. As a side note, the modal mass and stiffness matrices of Equation

---

[2] All the steps mentionned in Section 4.2.2 to Section 4.2.4 are explicitly related to the corresponding *Matlab* codes, which can be found in the resource files.

4.27 are obtained from the frequencies and modal masses given by *Samcef* with:

$$\begin{cases} \mathcal{A} & = \operatorname{diag}(\boldsymbol{\mu}) \\ \mathcal{E} & = \mathcal{A}\operatorname{diag}(\boldsymbol{\omega})^2 \end{cases}, \tag{4.28}$$

where $\boldsymbol{\mu}$ is the vector of the modal - or effective - masses, and $\boldsymbol{\omega}$ is the vector of the computed natural frequencies.

4.2.2 Discretization of the three lifting surfaces in vortex panels

This step consists in obtaining a three dimensional mesh similar to that of Figure 4.1 by using the actual geometrical specifications of the Sonaca 200. To do so, the wing planform is first discretized in m_{wing} chordwise and n_{wing} spanwise panels, respecting a linear increment for the $m_{\text{wing}} + 1$ chordwise points and a sinusoidal distribution for the $n_{\text{wing}} + 1$ spanwise points. It thus creates a higher panel density at the wing tips where wake roll-up phenomena take place, hence the need for a finer relative velocity field description at these locations even if the wake is frozen in the present case. It can be noted that the chord length distribution along the span is linearly interpolated between the values measured on the CAD model at the root and at a certain distance y close to the tip of the wing. Therefore, dimensions of the base configuration along the x axis do not correspond to a projection of the three dimensional wing on the ground, which should be elliptical due to the twist angle, but to an untwisted representation of its chord surface. The initial grid is then deformed in the vertical direction to follow the camber line $\bar{Y}(x)$ of a NACA 4415 using the analytical formula

$$\bar{Y}(x) = \begin{cases} \frac{\epsilon x}{q^2}(2q - \frac{x}{c}) & \text{for} \quad 0 \leq \frac{x}{c} \leq q, \\ \frac{\epsilon(c-x)}{(1-q)^2}(1 + \frac{x}{c} - 2q) & \text{for} \quad q \leq \frac{x}{c} \leq 1, \end{cases} \tag{4.29}$$

with $\epsilon = 0.04$ and $q = 0.4$, where c is the local chord length, ϵc is the maximum camber and qc is the distance between the leading edge point and the point of maximum camber along the x axis. To account for the influence of the dihedral angle, the camber is then multiplied by a factor $\cos(d)$ and the proper elevation is added with a linear function of y:

$$\Delta z_d(y) = y\sin(d). \tag{4.30}$$

The local angle of attack is finally generated by rotating each section in the (x, z) plane of an amount $\alpha(y)$ around its leading edge point, with

$$\alpha(y) = \alpha_0 + \frac{y}{s}\varepsilon_{\text{g}}. \tag{4.31}$$

The horizontal and vertical planes of the empennage have no camber nor dihedral, so sheer

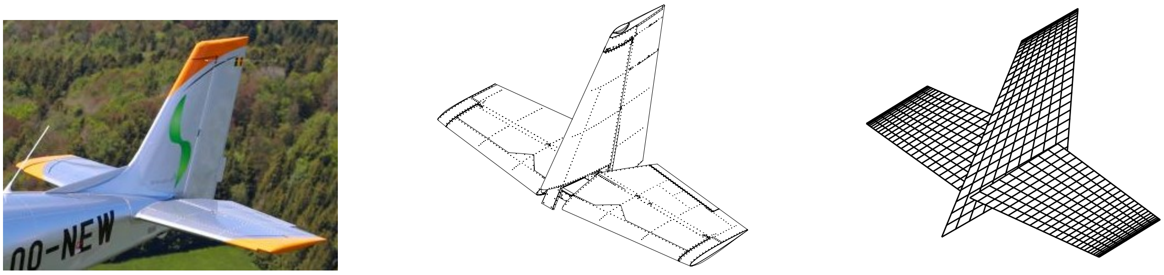

(a) Empennage of the Sonaca 200 assembled on the fuselage

(b) CAD model of the empennage used for measurements

(c) Aeroelastic model of the empennage as used for flutter analysis

Figure 4.3: Simplified aeroelastic model of the empennage for implementation in the VLM code

interpolations of values measured on the CAD file allow to recover the base shape of these components. Geometrical simplifications are made at the roots where the surfaces are simply extended toward their inner extremity, and toward the lower point of the rudder in the case of the vertical fin. As displayed in Figure 4.3, it is intended to account for the parts of the empennage masked by the rear fuselage. It can be higlighted that values for m_{HTP} and n_{HTP} corresponding to the tail, as well as m_{VTP} and n_{VTP} corresponding to the vertical fin, are scaled from m_{wing} and n_{wing} by using the local values for the span and chord length. It thus ensures conservation the panel density over the different lifting surfaces. The process for obtaining the bound vortex rings and wake vortex rings distributions follows the principles described in Section 4.1 and is performed with the `VLMmesh.m` *Matlab* function. As to the shed vortices, the chordwise extent of the wake generated by the main wing is defined from its trailing edge as a multiple $c^{\text{w}}_{\text{wing}}$ of c_{wing}. In order to facilitate control over the full mesh, lengths of the two other computed wakes are adapted so that the wing, tail and vertical fin have their wake stopping at the same location. For any lifting surface with a chord length c and m chordwise panels, the chord increment of the wake vortex rings has a constant value of c/m. It comes that the number of chordwise wake vortex is given by

$$m^{\text{w}} = \left\lceil \frac{c^{\text{w}} m}{c} \right\rceil, \tag{4.32}$$

where c^{w} is the wake length of the corresponding surface, determined by $c^{\text{w}}_{\text{wing}}$ and the airplane geometry. As illustrated in Figure 4.4, the procedure described here above allows to obtain a vortex lattice with a rather uniform mesh density over its different components, in addition to being easily modifiable.

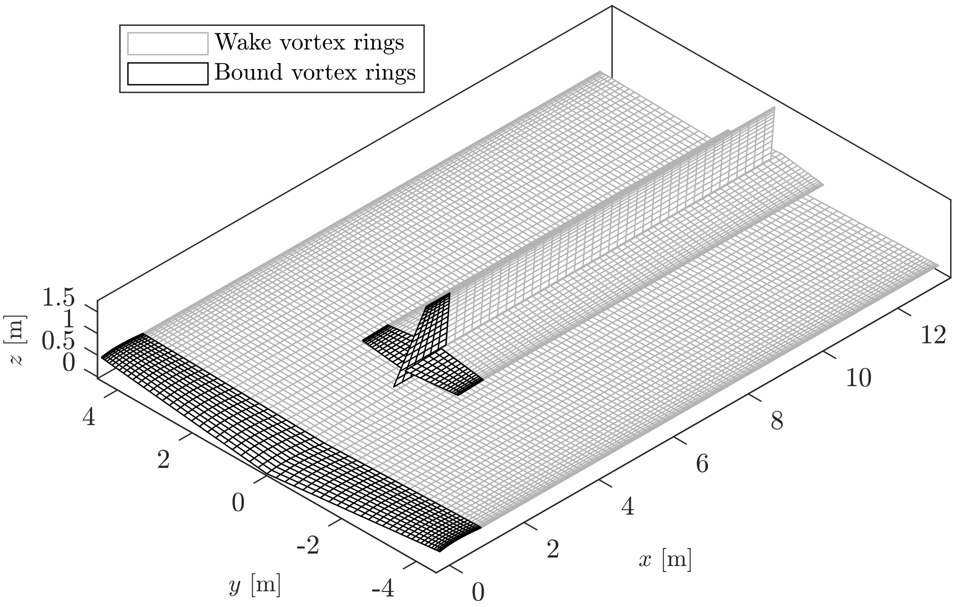

Figure 4.4: Aeroelastic model of the Sonaca 200 as used for flutter analysis, here represented with $m = 12$, $n = 30$ and $c_{\mathrm{wing}}^{\mathrm{w}} = 8c_{\mathrm{wing}}$ for the sake of clarity.

4.2.3 Computation of the influence coefficient matrices.

Once the aeroelastic mesh is created, influence coefficients matrices are computed with a double loop on each surface of the system. At each (i, j) iteration, *Matlab* function `influence.m` evaluates both the influence coefficient sub-matrix of bound vortex rings attached to surface i on collocation points of surface j and and the influence coefficient sub-matrix of wake vortex rings generated by surface i on collocation points of surface j. The underlying procedures are managed with C scripts using the *Matlab* API based on the guidelines given by Katz and Plotkin [2]. The global influence coefficients matrices are then assembled as displayed in Equations 4.12 and 4.13. It is always verified that all coefficient are non-zero.

4.2.4 Combination of the aeroelastic model with the structural eigenmodes

Interpolation of the mode shapes Thus far, normal displacement obtained from numerical modal analysis helped describe rigid motion of the chord at a few different locations along the span. It allowed to validate the finite element model of the airplane but further interpolations need to be performed in order the structural mesh to be finer than the aeroelastic mesh. Indeed, values of the displacement are linearly interpolated at the collocation point of the aeroelastic model. As an outcome, having a too coarse structural mesh would result in a linear pattern of the displacement field between neighbour collocation points, which should be avoided. For this purpose, the raw finite element mode shapes which contain 16 sections for the wing, 12 sections for the tail and 7 sections for the vertical fin are fitted with spline curves in *Matlab*. The resulting functions are then re-evaluated on a mesh of resolution $n = 100 \times m = 50$ to form operable extended mode shapes. The number of chordwise divisions is in fact here not important since no deformations are taken into account along the stream direction. This set of values is validated by a convergence study on the number of aeroelastic panels to use, as developed further in this section. The aeroelastic mode shapes produced with theses parameters, as used to form the $\mathbf{W}$ and $\partial_x \mathbf{W}$ matrices, are obtained with the `VLMmodes` function in *Matlab* and displayed in Figure 4.5.

Mesh convergence in terms of flutter speed The flutter determinant method introduced in Section 4.1 can be applied to the aeroelastic mode shapes in order to fix an aeroelastic model resolution by studying convergence of the flutter speed. It however appears that the studied configuration of the aircraft does not exhibit any flutter phenomenon in the subsonic range where the VLM applies. This study is thus carried out for the wing by itself which displays a flutter speed around 1050 km/h EAS at 0 km altitude in absence of the empennage. The chosen control variable is a rough measure of the panel density defined by

$$D = \frac{mn}{cs}. \tag{4.33}$$

This variable is progressively increased while keeping a constant n/m ratio until the flutter speed and frequency stabilize. This process is successively repeated for $n/m = 0.5$, $n/m = 1.4$, $n/m = 2.8$, and $n/m = 5.4$. As shown in Figure 4.6, it appears that decreasing the value for n/m leads to a quicker convergence of the flutter speed. However, a too low n/m ratio generates vortex rings with a very high aspect ratio in the spanwise direction, especially in the linear part of the sine distribution. It can be detrimental in terms of mode shapes description since it gives the deformation a more jagged aspect for a given number of panels, which is illustrated in Figure 4.7. This issue could be fixed by increasing the number of panels but it would be all the more demanding in computation time, as the small chord length of the stretched panels implies a finer time increment for vortex shedding. It can actually be noticed in Table 6 that the lowest value for n/m at 150 panels/m^2 displays a slight increase in computation time in comparison to the second and third tested values.

	$D = 150$ m^{-2}			
n/m [-]	0.5	1.4	2.8	5.4
CPU time [s]	21.84	20.69	20.55	23.93

Table 6: Comparison of the computation times for a fixed panel density and different values of the n/m ratio.

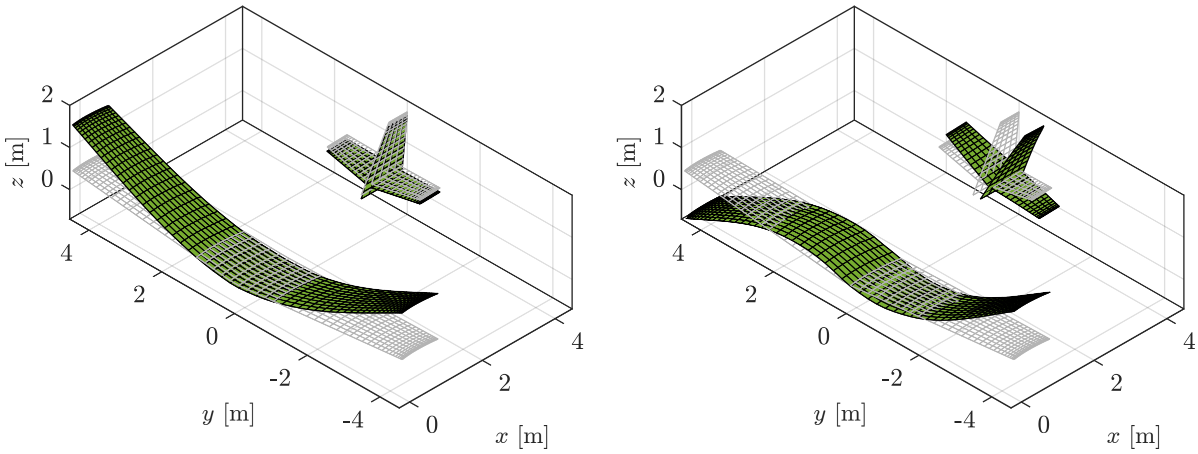

(a) Mode S1 (10.431 Hz). (b) Mode AR2_2 (21.123 Hz).

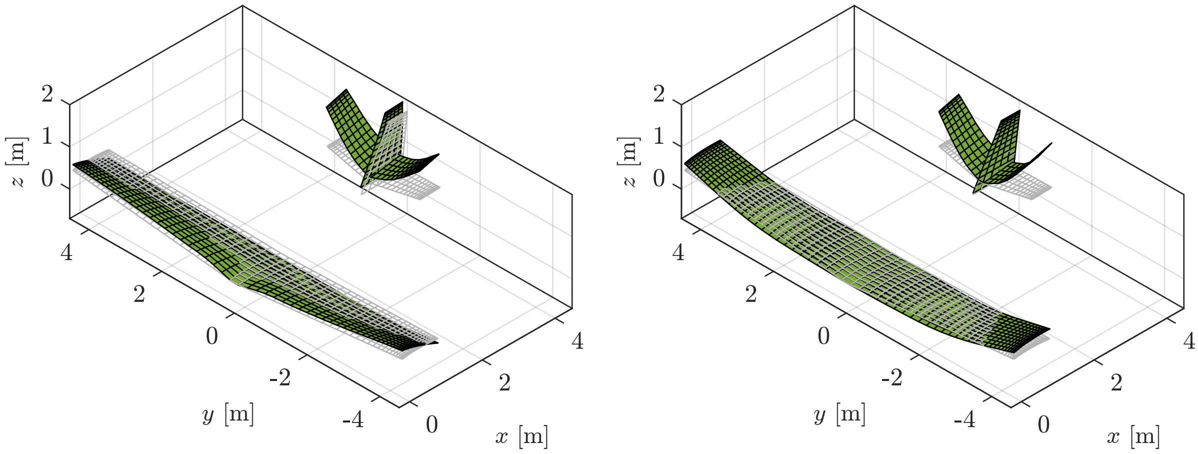

(c) Mode SX1 (31.704 Hz). (d) Mode SH (35.373 Hz).

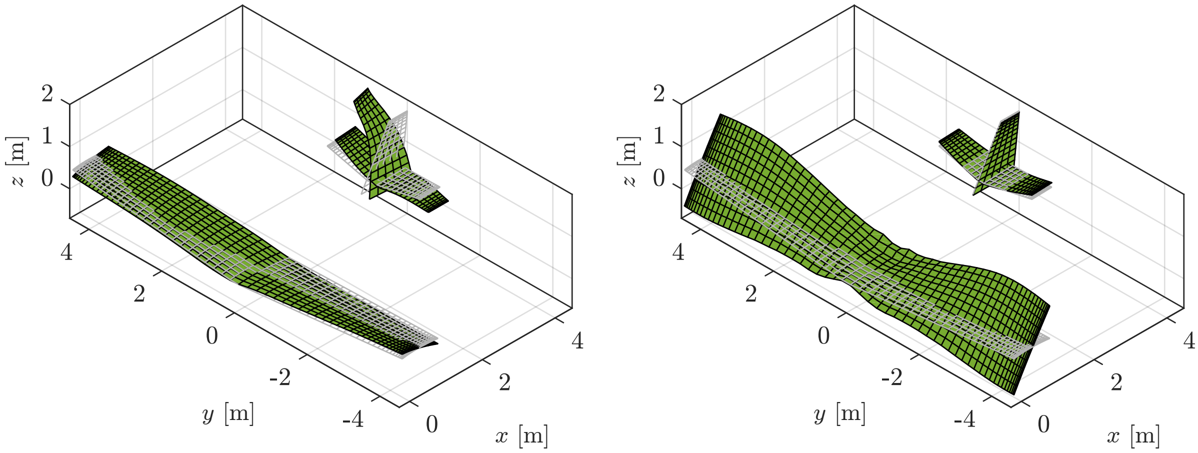

(e) Mode VTB (37.148 Hz). (f) Mode ST (49.471 Hz).

Figure 4.5: Numerical aeroelastic mode shapes of the Sonaca 200, obtained by combining the aeroelastic model with the extended finite element modes; the initial configuration is represented in grey and the deformation in black.

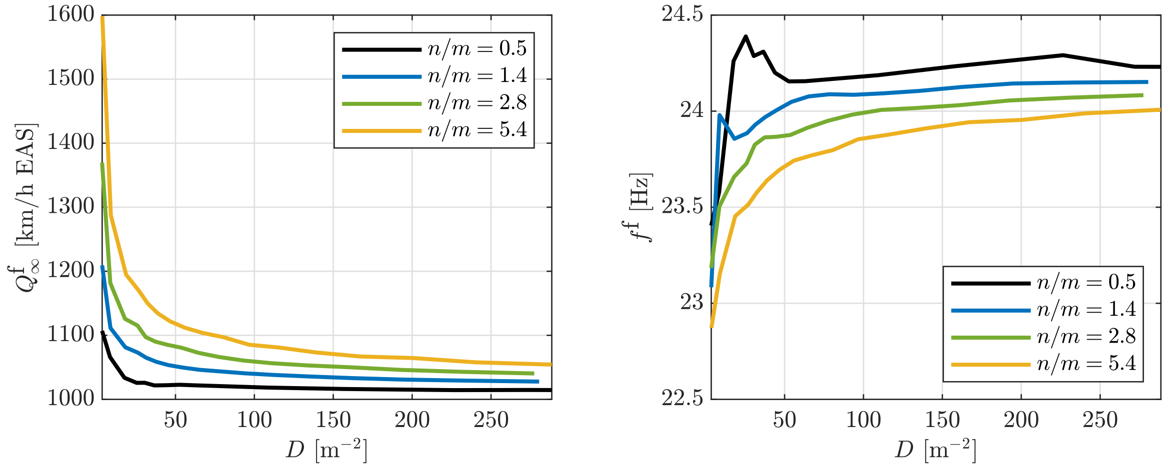

(a) Flutter speed *vs* panel density

(b) Flutter frequency *vs* panel density

Figure 4.6: Convergence curves of the flutter velocity and flutter frequency with respect to the panel density computed with Equation 4.33 for different m/n ratios; equivalent airspeeds are given at 0 km altitude.

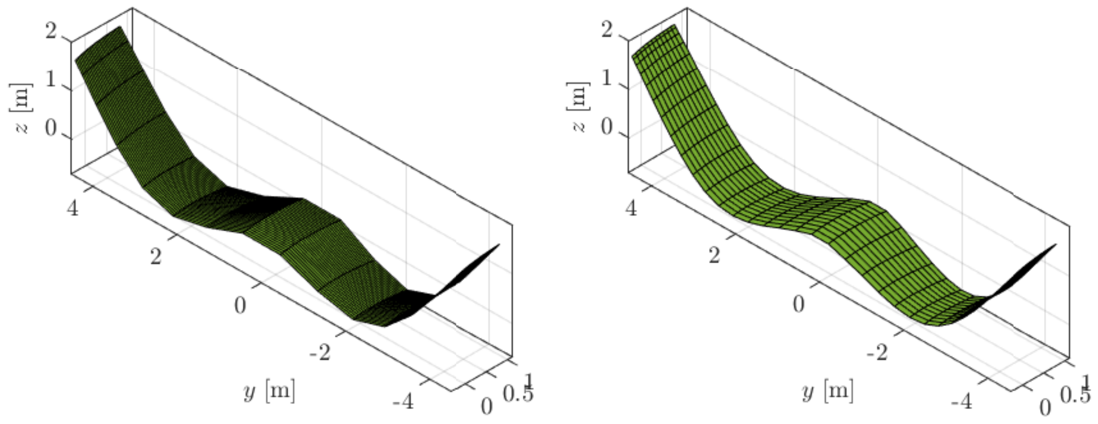

(a) $n/m = 0.5$ and $D = 65$ m^{-2}.

(b) $n/m = 2.8$ and $D = 65$ m^{-2}.

Figure 4.7: Comparison between the aeroelastic mode shapes obtained for a fixed panel density but two different n/m ratios in the case of mode ST.

To sum up, having a n/m ratio between 1 and 3 seems to be a reasonable compromise between convergence of the aeroelastic solution, fidelity of the mode shapes and required computation resources. Therefore, $n/m = 2$ is chosen for all the subsequent aeroelastic simulation, with $D = 150$ to ensure a fairly stabilized solution. It can be translated in terms of chordwise and spanwise panels, which gives $n = 64$ and $m = 32$. This result confirms the choice of structural mesh density used to build the extended mode shapes.

4.3 Flutter analysis results

4.3.1 $p - \kappa$ method

This approach uses the dynamic part of the equation of motion. It allows to get the damping ratios and eigenfrequencies of all the considered modes at any airspeed by applying an iterative procedure to Equation 4.27. This latter is transformed into an eigenvalue problem by introducing a new complex variable p verifying

$$\det\left(-p^2\mathcal{A} + \mathcal{E} - \rho Q_\infty^2 \mathbf{Q}_1(\kappa)\right) = 0. \tag{4.34}$$

An initial guess is made on the value of κ and, as discussed by Hassig [19], subsequent solutions of the determinant are assumed to appear in complex conjugate pairs:

$$p = \frac{\delta}{2\pi}\omega \pm i\omega, \tag{4.35}$$

where δ is a negative logarithmic decay rate and ω a damped frequency. For a given mode, iterating with a new value for κ given by $\kappa = \omega b/Q_\infty$, with $\omega = \mathfrak{Im}(p)$, then allows converge toward a (p, κ) couple that satisfies Equation 4.34. Once the damped frequency is converged, the natural frequency is obtained with $\omega_\text{n} = |p|$ and the damping ratio is deduced with $\zeta = -\mathfrak{Re}(p)/\omega_\text{n}$. This procedure, as illustrated in Figure 4.8, must be repeated for each mode and multiple airspeed in the range of interest in order to have an overview of the aeroelastic behavior of the system.

4.3.2 Validation of the method with experimental modes

Outputs provided by the $p - \kappa$ method can be compared with reference flutter analysis curves of the Sonaca 200. In order to first validate the VLM code without influence of the finite element model, a resolution is carried out on the set of available experimental modes. The experimental aeroelastic modes are obtained with the same techniques as for the finite element aeroelastic modes and are displayed in Figures **??** and 4.9.

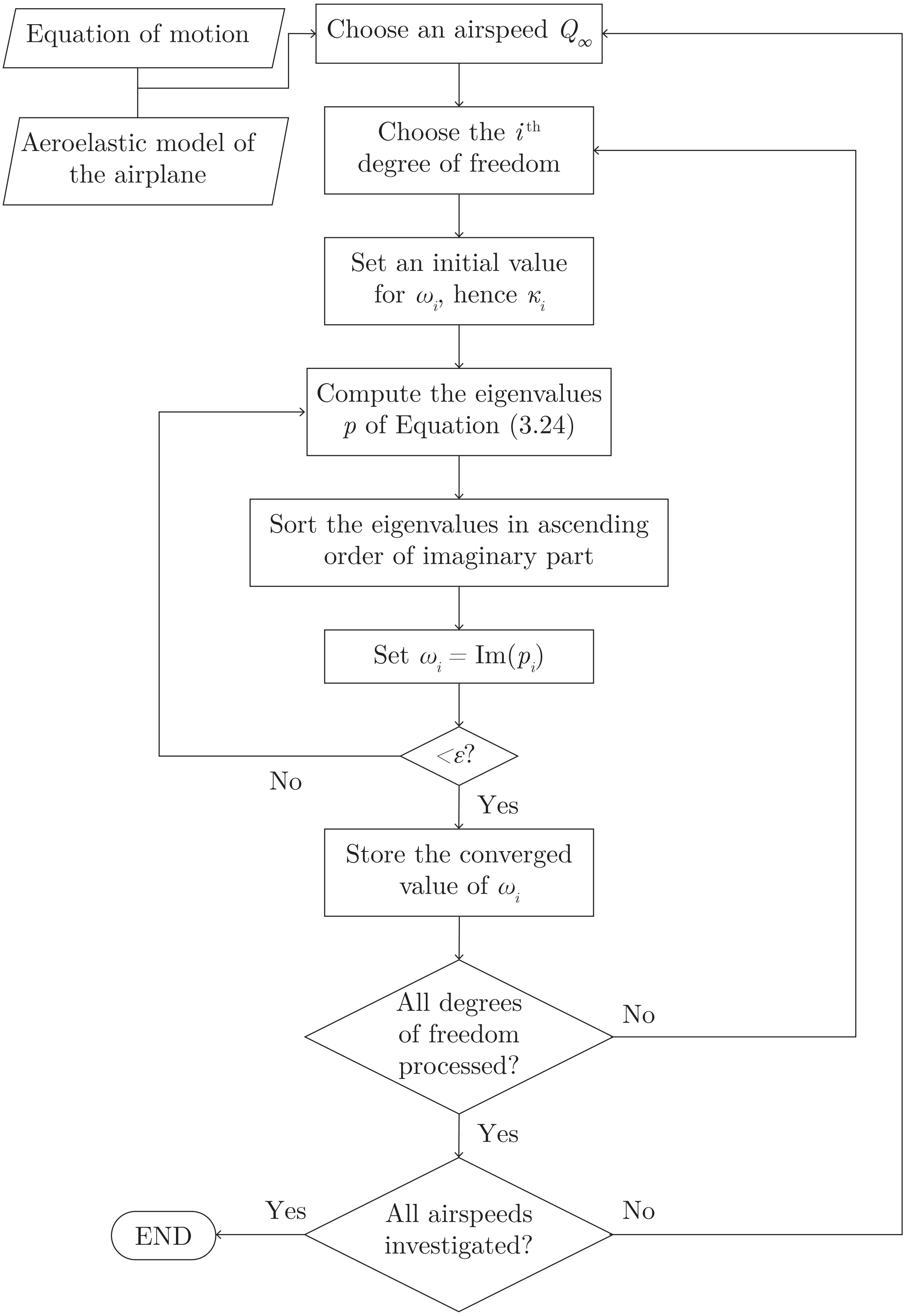

Figure 4.8: Implementation of the frequency matching process to obtain damping and frequency curves with the $p - \kappa$ method

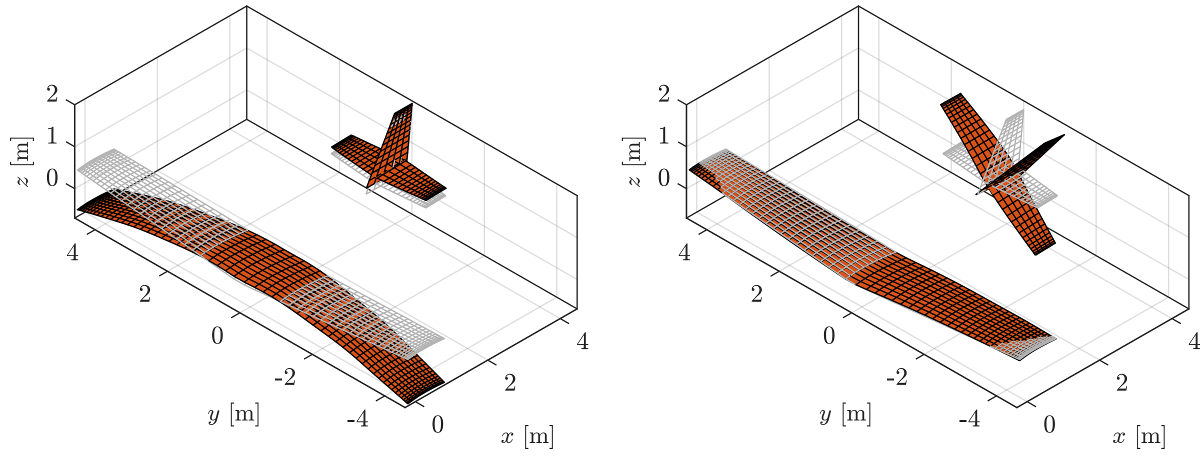

(a) Mode S1 (10.431 Hz).

(b) Mode AR2_2 (21.123 Hz).

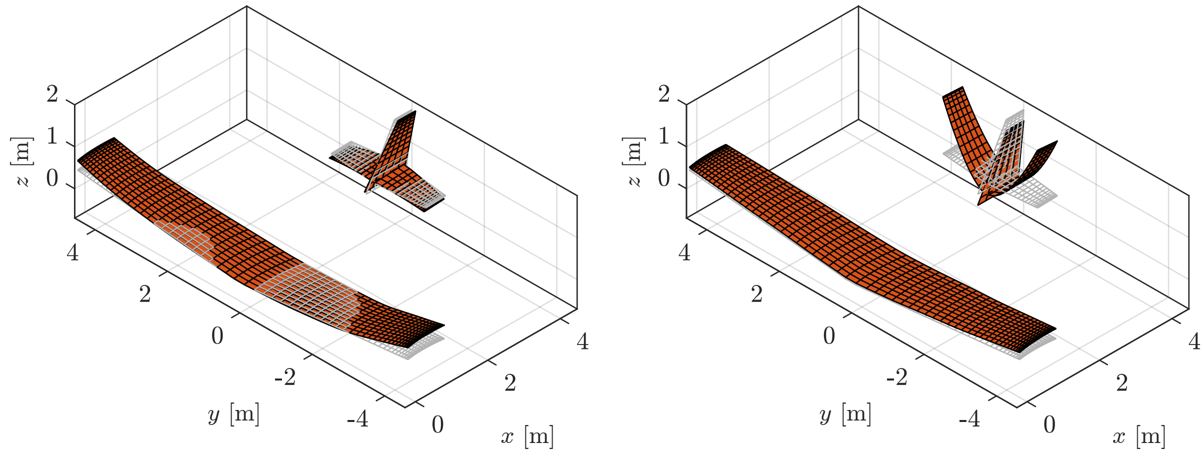

(c) Mode SX1 (31.704 Hz).

(d) Mode SH (35.373 Hz).

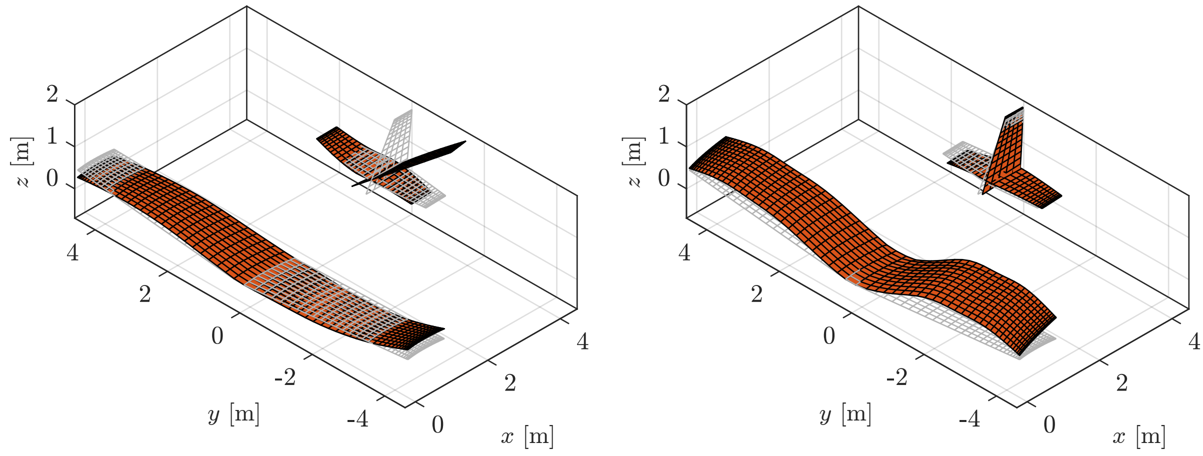

(e) Mode VTB (37.148 Hz).

(f) Mode ST (49.471 Hz).

Figure 4.9: Experimental aeroelastic mode shapes of the Sonaca 200, obtained by combining the aeroelastic model with the extended mode shapes generated on the experimental data provided by *Leichtwerk AG* (Part.2); the initial configuration is represented in grey and the deformation in black.

The resulting curves are presented in Figure 4.10 in comparison with the reference material. It can be observed that the computed aeroelastic solution shows rather similar trends in terms of frequencies and damping ratio.

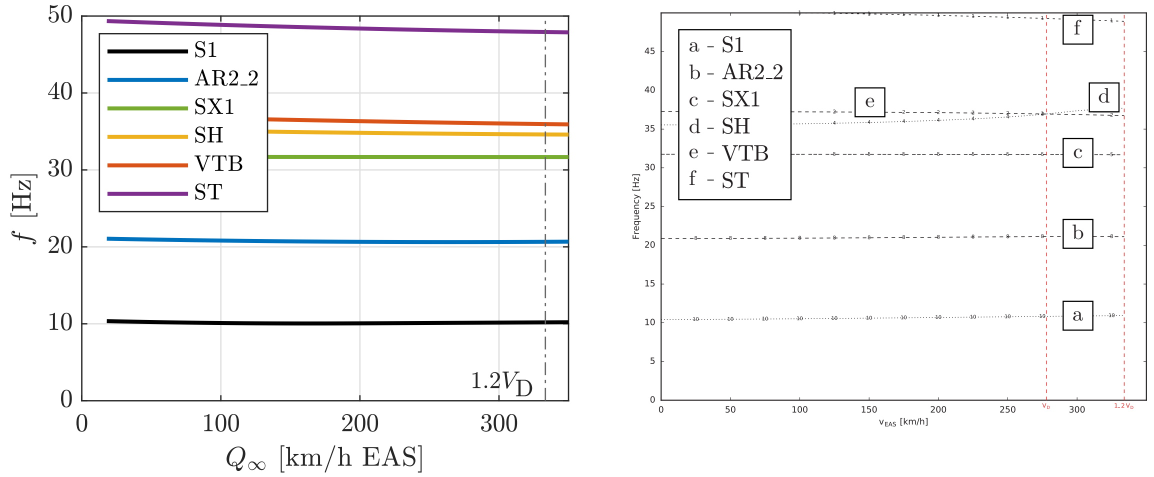

(a) Eigenfrequencies computed with the VLM code *vs* free stream velocity.

(b) Eigenfrequencies provided by *Leichtwerk AG vs* free stream velocity [20].

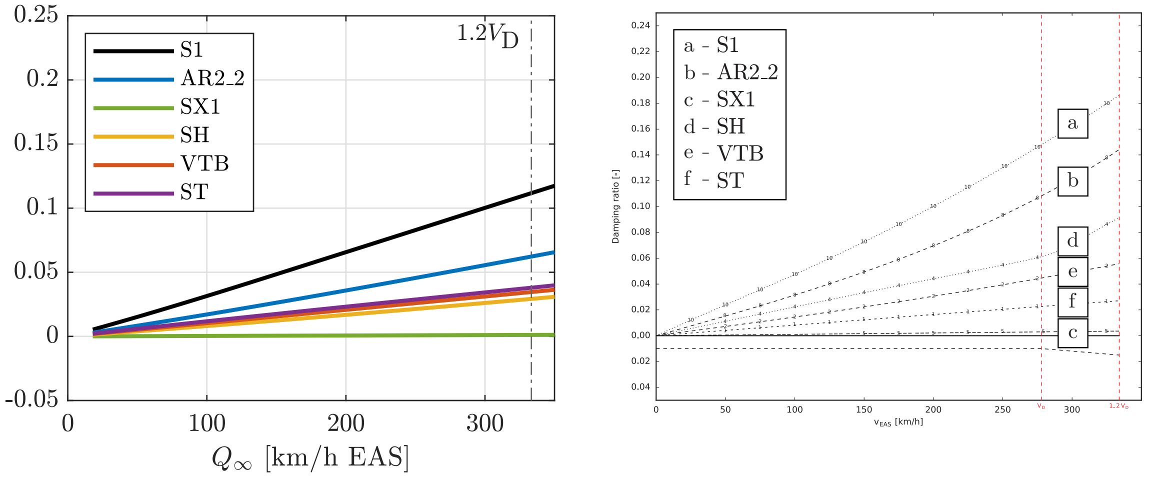

(c) Damping ratios computed with the VLM code *vs* free stream velocity.

(d) Damping ratios provided by *Leichtwerk AG vs* free stream velocity [20].

Figure 4.10: Comparison between the VLM solutions and the flutter analysis data provided by *Leichtwerk AG* exploiting in both cases the same experimental modal a anlysis outputs; reference curves on the right are reproduced from [20] and slightly edited for better visualization; computed solutions are based on the experimental aeroelastic modes presented in this report (Figures **??** and 4.9).

In both cases, S1 appears to be the most damped structural mode, whereas SX1 is very lightly damped in comparion to the other modes considered. The relative importance of the other modes on the damping plot is also almost identical between the reference and simulated results. The only difference concerns modes SH and VTB, which in both cases have close damping values but are inverted with respect to the reference data in the VLM solution. In this regard, it can be noted that symmetrical and antisymmetrical modes were separately handled in the initial flutter analysis. As presented in [20], degrees of freedom of the system seem to have first been expanded on all the symmetrical modes to obtain the corresponding damping curves and on all the antisymmetrical modes afterwards. It suggests that SH, which is symmetrical, and VTB, which is antisymmetrical, might have been expressed in two different bases, hence the slight noticeable variations. It could also explain why these modes have intersecting frequency curves while this behaviour is not to be seen in the current solution. Unfortunately, too few details are unveiled in the technical report of *Leichtwerk AG*, which does not grant to confirm nor refute these hypotheses. A last remark concerns the obvious difference in magnitude regarding the damping ratios. The results obtained by *Leichtwerk AG* are actually almost two times higher than those of the VLM code, which was already observed by Lempereur [11] in the first iteration of the aeroelastic model of the S200. A possible explanation may be a different definition of the damping ratio in use for the reference data. Besides, it can be reminded that the company fell back on a 2D strip theory approach to estimate the aeroelastic solution, whereas the implemented procedure relies on 3D aerodynamics.

4.3.3 Comparison with the FEM modes

In total, eleven vibration modes were extracted from finite element analysis. Similarly to the experimental data, they can be converted into aeroelastic modes and processed with the VLM code to obtain frequency and damping curves. As shown in Figure 4.11, the resulting graphs display similar tendencies as previously. Natural frequencies remain almost stationary while damping ratios monotonously grow with the free stream velocity. It is comforting to observe than no flutter phenomenon happens in the airspeed range of interest, which is consistent with the behavior of the real aircraft.

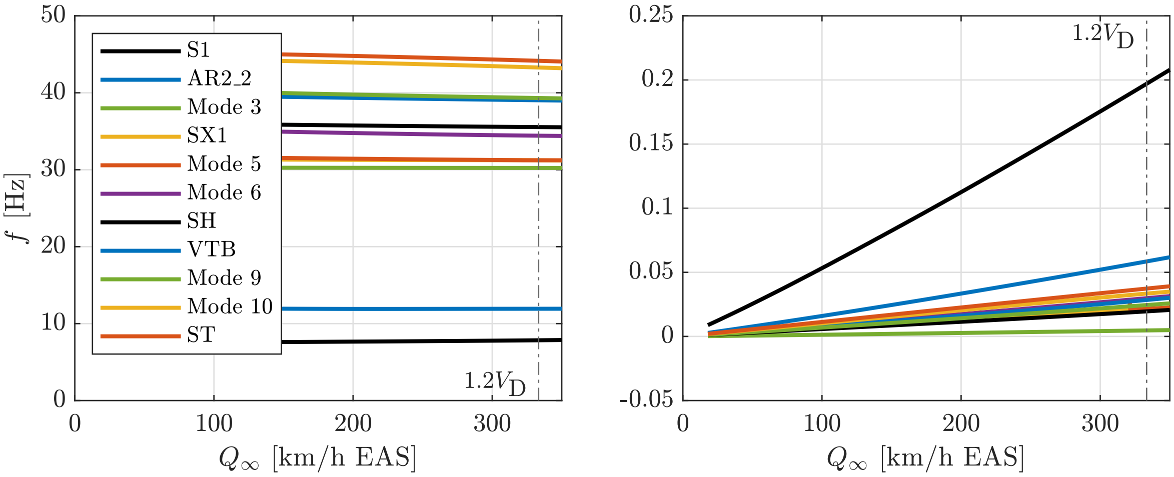

(a) Eigenfrequencies computed with the VLM code *vs* free stream velocity.

(b) Damping ratios computed with the VLM code *vs* free stream velocity.

Figure 4.11: Results of the $p - \kappa$ method applied to the numerical aeroelastic modes.

Like in the experimental case, it can be observed that the first mode is the most damped but it is hard to distinguish the other damping curves due to them being cluttered around the same values. In order to have a better overview of the finite element results and to compare them with data generated with the experimental aeroelastic modes, the six modes of Section 4.3.2 are isolated. The aeroelestic solution is thus computed only with these latter, neglecting contribution of the other eigenmodes. It can first be observed in Figure 4.12 that reducing the number of modes in such a way has very few effects.

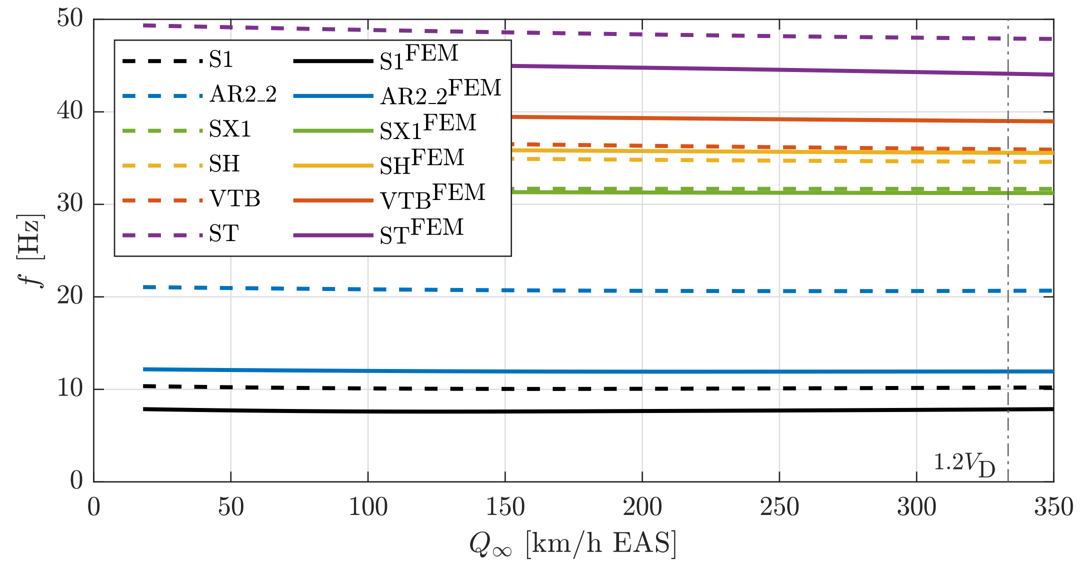

(a) Eigenfrequencies computed with the VLM code *vs* free stream velocity.

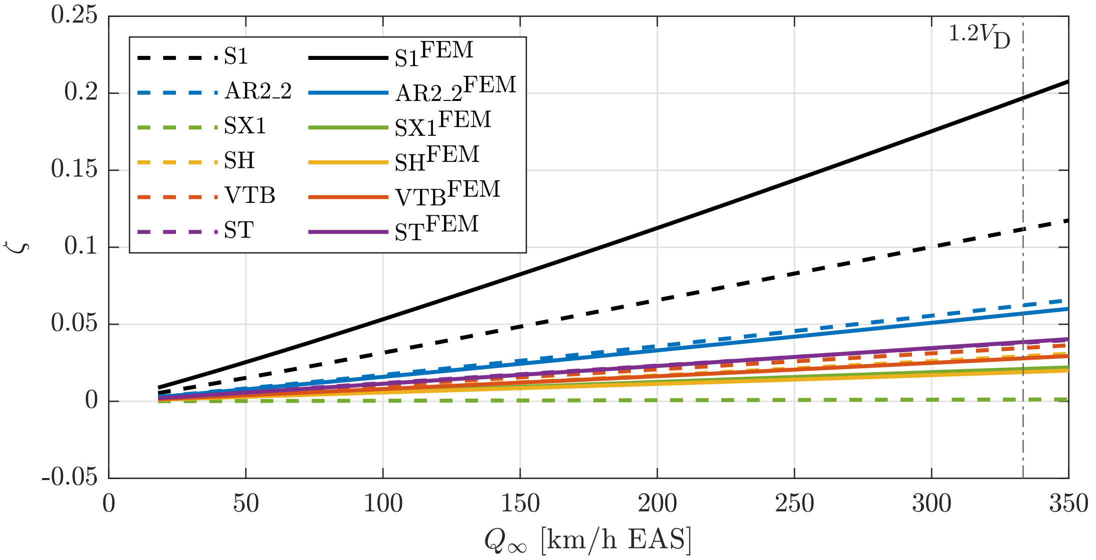

(b) Damping ratios computed with the VLM code *vs* free stream velocity.

Figure 4.12: Comparison between the frequency and damping curves computed with the VLM code for experimental aeroelastic mode shapes and the finite element aeroelastic mode shapes.

It can be noticed by looking for instance at the unchanged values for the damping ratio of S1 and AR2_2 at $1.2V_\mathrm{D}$. Resemblance of the finite element based solutions to the experimental based ones varies depending on the eigenmode. The damping curves provided for mode ST almost perfectly overlap in spite of the low modal correlation factor stated in Section 3.3. More surprisingly, the two curves obtained for AR2_2 are also quite close even though matching between the two modes was very loosely established. Similarity between the experimental and finite element damping curves for SH that can be seen on the graph was more likely since it is one of the best fitted modes. Another remark is that SX1 is no longer the less damped mode in the case of the finite element results. It may be justified by the fact that, as mentioned in Section 3.3, vertical tail plane bending has a non negligible contribution in the computed eigenvector.

4.4 Conclusions

The implemented VLM does not contradict the analysis carried out by *Leichtwerk* outside the influence of the finite element model. It may be vain to expect a perfect match between the different curves since the implemented methods a priori significantly differ. Relevance of the computed results can still be put forward, as developed in Section 4.3.2 and offers good prospect to eventually apply the algorithm to other configurations. Using the finite element data in the code highlighted sensitivity of the solutions to modal parameters, which invites to respect a critical distance from the evaluated numerical values. This given, it might be interesting to observe the computed flutter speed in cases where it can be computed. It would however requires extensive improvements of the finite element model to take into account control surfaces.

5 General conclusions

This work illustrates how it is possible to break down analysis of a complex system into different simplification steps. For aeroelastic modelling of th Sonaca 200, they can be listed as: mechanical description of the aircraft by proxy of thin structures theory, creation of a finite element model with beam elements, aeroelastic modelling of the plane using a well chosen set of surfaces and aeroelastic solving with a vortex lattice method. The aeroelastic solution computed with the VLM code based on experimental vibration modes does not contradict the 2D approach regarding behavior of the damping and frequency terms. Besides, results remain fairly consistent in the case of finite element modes. It thus illustrates that the methods applied in the different resolution stages were viable to a certain extend. It is not completely surprising as numerous verification phases were respected throughout this study to ensure a progression relying on physically acceptable data. In addition to this, present study especially highlights capability of the frequency-domain Vortex Lattice Method in an industrial case. As an outcome, it can be established that the practical implementation of the method for a full airplane has good prospects in further development of the presented work. Nonetheless, a few limitations remain. It would indeed have been beneficial to posses more experimental modal data to compare the VLM outputs with the 2D approach. There might also be place for improvement in terms of description of the lifting surfaces, without saying that aerodynamic influence of the fuselage was neglected from the beginning. Moreover, it could be interesting to investigate possibilities of creating a more accurate finite element model in terms of mass distribution, internal and external boundary conditions. It however remains delicate due to sensitivity of the modal analysis results to geometrical or physical adjustments in the model. In practice, a more comprehensive description of the boundaries between the structural members using an appropriate analytical approach instead of rough approximations, or specific finite element simulations, could help improve quality of the model. This can also be coupled with a definition of stiffness terms describing the flexible engine mount. A more obvious modification to the model would be to take into account rigid body degrees of freedom of the control surfaces to perform modal analysis on the control free configuration which were identified as critical by *Leichtwerk AG*. The main objective would be to ensure that flutter can be predicted in the corresponding flight conditions. Since operable experimental data are not available to do so, the alternative to develop is thus using data provided by the finite element model incorporating mobile control surfaces. This can be performed by defining cinematic connections instead of rigid links between the wing and ailerons, horizontal tail plane and elevator, vertical tail plane and rudder, with a software such as *Mecano*. The developed algorithm and structural analysis methodology could then be validated as a satisfying way to predict flutter phenomena.

6 Sources

[1] Thomas Henry Gordon Megson. *Aircraft structures for engineering students*. Butterworth-Heinemann, 2016.

[2] Joseph Katz and Allen Plotkin. *Low-speed aerodynamics*. Vol. 13. Cambridge university press, 2001.

[3] Grigorios Dimitriadis, NF Giannelis, and GA Vio. “A modal frequency-domain generalised force matrix for the unsteady Vortex Lattice method”. In: *Journal of Fluids and Structures* 76 (2018), pp. 216–228.

[4] *Sonaca 200, Product Overview*. `https://www.sonaca-aircraft.com/products/sonaca-200`. Accessed: 2020-07-06.

[5] *Certification Specifications for Very Light Aeroplanes (CS-VLA)*. 2003.

[6] George Platanitis and Thomas W Strganac. “Suppression of control reversal using leading-and trailing-edge control surfaces”. In: *Journal of guidance, control, and dynamics* 28.3 (2005), pp. 452–460.

[7] *Boeing 737 rudder issues*. `https://en.wikipedia.org/wiki/Boeing_737_rudder_issues`. Accessed: 2020-06-30.

[8] Michael W Kehoe. “A historical overview of flight flutter testing”. In: (1995).

[9] William P Rodden and E Dean Bellinger. “Aerodynamic lag functions, divergence, and the British flutter method”. In: *Journal of Aircraft* 19.7 (1982), pp. 596–598.

[10] *A-AS-ASS-001-C Complete Aircraft Assembly*. Tech. rep. Sonaca Aircraft, 2019.

[11] B Lempereur. *Structural modelling for the flutter analysis of the S200 aircraft*. Tech. rep. University of Liege, 2018.

[12] F Sohani and H Eipakchi. “Analytical solution for modal analysis of Euler-Bernoulli and Timoshenko beam with an arbitrary varying cross-section”. In: *Mathematical Models in Engineering* 4 (Sept. 2018), pp. 164–174. DOI: `10.21595/mme.2018.20116`.

[13] A oares da Costa Azevêdo and S dos Santos Hoef. “Modal analysis for free vibrations of four beam theories”. In: (Dec. 2015).

[14] *Aide de NX 12, Boîte de dialogue Section de poutre*. `https://docs.plm.automation.siemens.com/tdoc/nx/12/nx_help/#goto:advanced:beam_section`. Accessed: 2020-05-29.

[15] I.E. Elishakoff. *Handbook On Timoshenko-ehrenfest Beam And Uflyand- Mindlin Plate Theories*. World Scientific Publishing Company, 2019. ISBN: 9789813236530. URL: `https://books.google.be/books?id=CjHnDwAAQBAJ`.

[16] Michel Géradin and Daniel J Rixen. *Mechanical vibrations: theory and application to structural dynamics*. John Wiley & Sons, 2014.

[17] D Tempel and O Meister. *Ground Vibration Test of the Aircraft Sonaca S200*. Tech. rep. Leichtwerk AG, 2016.

[18] David J Ewins. *Modal testing: theory and practice*. Vol. 15. Research studies press Letchworth, 1984.

[19] Hermann J Hassig. "An approximate true damping solution of the flutter equation by determinant iteration." In: *Journal of Aircraft* 8.11 (1971), pp. 885–889.

[20] D Tempel and O Meister. *Flutter Analysis of the Aircraft Sonaca S200*. Tech. rep. Leichtwerk AG, 2016.

Annex

A Shear stress in stiffener sections

Let i index a stiffener of cross section area A_i fixed to and arbitrary thin structure under shear load T_z. Its total cross section contour is noted l_i and its wall thickness t_i. As shown in Figure A.1, its contour is parametrized with abscissa s' going from 0 to s'_1, respectively corresponding to $\tilde{z}_i$ and z_i. It can be recalled that

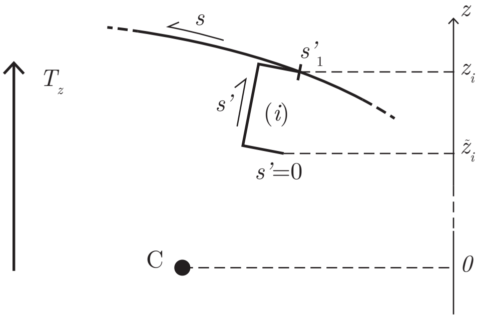

Figure A.1: Parametrization of the skin-stringer connection.

$$\frac{T_z}{A'} = \int_A \sigma_{xs}^2 dA, \tag{A.1}$$

where A is here the total area of the thin structure cross section, which is separated between the skin area and the stringers area. As an outcome:

$$\frac{T_z}{A'} = \int_{A_{\text{sk}}} \sigma_{xs}^2 dA + \int_{A_{\text{st}}} \sigma_{xs}^2 dA, \tag{A.2}$$

where A_{sk} is the total area of the skin and A_{st} is the total area of the stringers. Under the sufficient condition that $|z_i| >> l_i$ it can be shown that

$$\int_{A_i} \sigma_{xs}^2 dA \leq \frac{T_z^2 z_i^2 A_i^3}{I_y^2 t_i^2}. \tag{A.3}$$

Proof. From the definition of the shear flow, the integral over the stringer area writes

$$\int_{A_i} \sigma_{xs}^2 dA = \int_{s'=0}^{s'_1} \frac{1}{t_i} q^2(s') ds'. \tag{A.4}$$

And

$$q(s') = -\frac{T_z}{I_y} \int_0^{s'} t_i z(s'') ds'', \text{ with} \left\{ \begin{array}{rc} z(s'') = & \tilde{z}_i + f(s'') \\ |f(s'')| \leq & s'' \end{array} \right. . \tag{A.5}$$

So

$$\frac{I_y}{T_z}q(s') = \tilde{z}_i t_i s' + \int_0^{s'} f(s'')ds''. \tag{A.6}$$

It yields

$$\tilde{z}_i t s' - t_i \int_0^{s'} s''ds'' \leq \frac{I_y}{T_z}q(s') \leq \tilde{z}_i t s' + t_i \int_0^{s'} s''ds'', \tag{A.7}$$

which means

$$\tilde{z}_i t s' - \frac{t_i}{2}s'^2 \leq \frac{I_y}{T_z}q(s') \leq \tilde{z}_i t s' + \frac{t_i}{2}s'^2. \tag{A.8}$$

In the case where $\tilde{z}_i \geq 0$,

$$\tilde{z}_i t s' + \frac{t_i}{2}s'^2 \leq \tilde{z}_i A_i + \frac{A_i^2}{2t_i}. \tag{A.9}$$

And

$$\tilde{z}_i A_i + \frac{A_i^2}{2t_i} \leq 2A_i z_i \iff 2z_i - \tilde{z}_i \geq \frac{A_i}{2t_i} = \frac{1}{2}l_i, \tag{A.10}$$

which is verified since $2z_i - \tilde{z}_i \simeq z_i$. Furthermore $\tilde{z}_i t s' - \frac{t_i}{2}s'^2$ is positive for $s' \leq 2\tilde{z}_i$ which is the case according to the initial assumption. In other words

$$0 \leq \frac{I_y}{T_z}q(s') \leq 2A_i z_i \tag{A.11}$$

The case where $\tilde{z}_i < 0$ is symmetrical and similarly leads to

$$-2A_i zi_{\leq}\frac{I_y}{T_z}q(s') \leq 0. \tag{A.12}$$

It can thus be written that

$$|q(s')| \leq 2\frac{A_i z_i T_z}{I_y}. \tag{A.13}$$

As an outcome:

$$\int_{s'=0}^{s'_1} \frac{1}{t_i}q^2(s')ds' \leq 2\frac{T_z^2}{I_y^2 t_i}\int_0^{s'1} z_i^2 A_i^2 ds' = 2\frac{T_z^2 z_i^2 A_i^2}{I_y^2}l_i = 2\frac{T_z^2 z_i^2 A_i^3}{I_y^2 t_i^2}. \tag{A.14}$$

□

Returning now to the equation for the reduced cross-section area, it comes that

$$\frac{A}{A'} = \frac{A}{T_z}\int_{A_{\text{sk}}} \sigma_{xs}^2 dA + \frac{A}{T_z}\int_{A_{\text{st}}} \sigma_{xs}^2 dA, \tag{A.15}$$

which can write

$$\frac{1}{k_z^*} = \frac{A}{A_{\text{sk}}}\frac{1}{k_z} + B, \tag{A.16}$$

Section	$\frac{A}{A_{\text{sk}}}\frac{1}{k_z}$	B
FUS3	3.9957	0.2398
FUS6	6.1786	0.0262
FUS10	2.6150	0.0316

Table 7: Comparison of the skin and stringers related terms in the equation for the shear factor.

where B verifies

$$B \leq A \sum_i 2 \frac{z_i^2 A_i^3}{I_y^2 t_i^2}. \tag{A.17}$$

By comparing numerical values of the two terms in Equation A.16, it appears that B remains negligible, as it is shown in Table 7. The final expression for the shear factor can thus be reduced to

$$k_z^* = \frac{A_{\text{sk}}}{A_{\text{sk}} + A_{\text{st}}} k_z. \tag{A.18}$$

B Additional finite element vibration modes

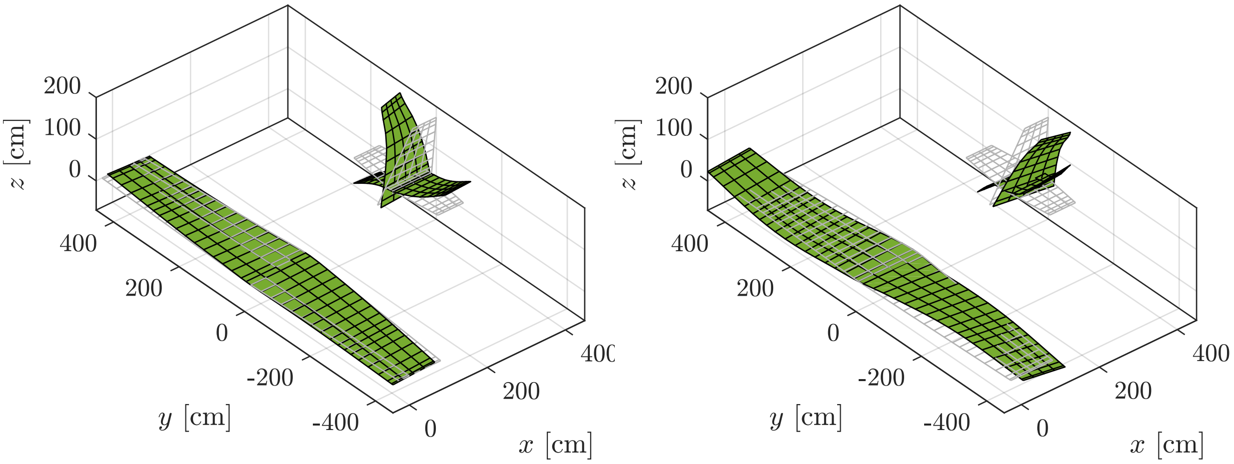

(a) Mode 3 (30.305 Hz).

(b) Mode 5 (31.884 Hz).

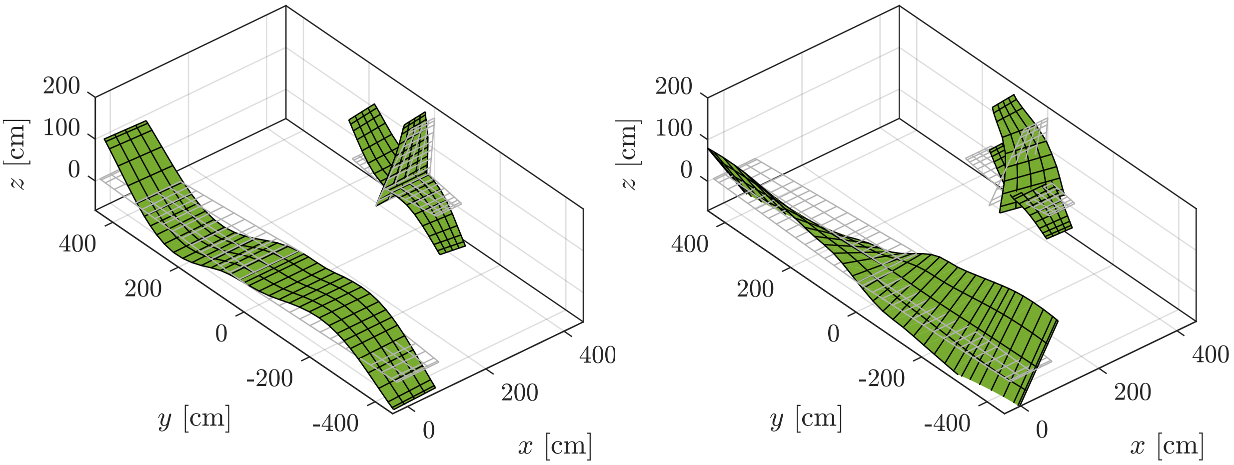

(c) Mode 6 (35.598 Hz).

(d) Mode 10 (44.450 Hz).

Figure B.1: Additional numerical modes that were not validated with experimental data; the initial configuration is represented in grey and the deformation in green.